

# **Thi-Qar University Journal for Engineering Sciences**

ISSN 2075-9746

## **The English Section Contents**

<b>Author</b>	<b>Title</b>	<b>Pages</b>
Oday J. Al-Furaiji Aksana G. Shauchuk, Viktar Yu. Tsviatkou,	Localization and Normalization of Isolated Direct Contour Lines Based On Masks and Form-Factor	1-18
Hussein A. Shaia	Numerical Simulation to Study the Effect of Combination Vertical Load and Lateral Load on Pile Performance in Cohesionless Soil	19-30
Ahmad Jasim Mohammad	Artificial Aging Time Effect on Fatigue stress for Friction Stir Welded AA6061T6	31-42
Dr. Ahmed K. Al – Shara Dr. Hussien S. Sultan Haitham M. Bachi	Effectiveness of film cooling process on flat plate using multi-rows of cooling	43-53
Wasan Q. Fayyadh	Effect of using waste-iron on the mechanical properties of concrete	54-65
Dr. Khansaa Dwood Salman Dr. Muhannad Zedain Khalifa	Wear Behavior of An Aluminum Alloys Using Nd:YAG Laser Treatment	66-76
MARWA S.HASHIM DR. KHEARIA A.MOHAMMED DR. NAWAL JASIM HAMADI	Identification of Impressed Current Cathodic Protection System (ICCP) By Artificial Neural Network	77-89
Tahseen Ali Gabbar	Study The Effect Of Water – Gas Shift Equilibrium on Adiabatic Flame Temperature for Alkanes Family Fuels at rich conditions	90-100
Alaa Liaq Hashem	Evaluation of Off-Grid PV-Battery Inverter System for Supporting Energy Sector in Iraq	101-113

## Localization and Normalization of Isolated Direct Contour Lines Based On Masks and Form-Factor

<sup>1</sup>Oday J. Al-Furaiji      <sup>2</sup>Aksana G. Shauchuk,      <sup>3</sup>Viktar Yu. Tsviatkou,

1 Head of Computer Technologies Engineering, Kinouze University College

2. Department of networks and devices BSUIR, Minsk, Belarus

3. Department of networks and devices BSUIR, Minsk, Belarus

### Abstract

The method for localization of isolated direct contour lines based on form- factor is proposed in this paper. The essence of this method consists in comparison to unit of value of form-factor – the relations of the size of the contour line (distance between end points) to its length (number of the forming contour pixels). It is found that the proposed method provides a gain in speed of allocating direct contour lines in 4 times in comparison with the method of LSD (Line Segment Detector) and in 14.8 times in comparison with the method based on the Hough transform.

The effective method of normalization of the contour line on thickness on the basis of the analysis of orientation of the connected pixels is proposed in this paper. This method is specially developed for deleting excess pixels of a dedicated line.

Also developed algorithm of normalization of contour lines on thickness promotes the best calculation of a form-factor.

**Key words:** allocation of direct lines, contour image processing, key elements, identification, parameterization.

**الخلاصة:** تحديد وتطبيع الخطوط الكنتورية المستقيمة المنعزلة على اساس الاقنعة وعامل الشكل في هذا البحث تم اقتراح طريقة لتحديد الخطوط الكنتورية المستقيمة المنعزلة على اساس عامل الشكل. اساس هذه الطريقة يكمن بالمقارنة بوحدة قيمة عامل الشكل علاقة حجم الخط الكنتوري (البعد بين نقاط النهاية) والنسبة الى طولها (عدد البكسلات الكنتورية المكوّنة). وقد وجد بان الطريقة المقترحة توفر ربح في سرعة تحديد الخطوط الكنتورية المستقيمة بـ (٤ مرات) مقارنة بطريقة مكتشف المقطع الخطي LSD (Line Segment Detector) و بـ (١٤,٨ مرة) مقارنة بطريقة تحويل هوف Hough transform.

### Introduction

Methods of processing of the overlapped images (imposing, comparison, creation of panoramas, etc.) are based on localization the key elements. The most effective methods of localization of key elements, such as SIFT [1] and SURF [2], use keypoints. It allows to reduce computing complexity of comparison of images in comparison with correlation methods [3], however results in low resistance of results of localization of reference points to change of brightness, contrast and noise of the image. Direct lines possess considerably bigger stability in comparison with points. For their allocation on images the methods based on transformation of the Half [4], mask search [5], calculation of a gradient [6] and quantization on orientation [7] are widely used. However these methods have high computing complexity. Elimination of this shortcoming possibly at the expense of the accounting of a ratio of lengths of contour lines and distances between their end points, that is at the accounting of a form factor of the contour line.

In case of parametrization and identification of lines with use of a form factor thin boundaries yield considerably the best result. Therefore after application of operators of separation of boundaries (Canny, Roberts and others)

it is necessary to subject dedicated lines to additional processing – a thinning of line. Algorithm of thinning is resulted by deleting all excess contour pixels and contour lines one pixel thick is created.

Widely used algorithm of thinning, such as algorithm Zong-Suen [8], the algorithm of thinning by sample, a wave method, Shchepin algorithm, provide the maximum thinning of contour lines [9]. However these approaches aren't effective for a algorithm of thinning of the contour lines having thickness some pixels as are oriented on processing of areal objects of any size and therefore use iterative algorithms of deleting excess contour pixels before achievement of the required line thickness that leads to growth of time of contour processing.

For abbreviation of time of processing of the contour lines having thickness some pixels it is possible to use algorithm of normalization of the line on thickness which is based on processing of the form of lines and not iterative algorithms.

Method of localization of lines on the basis of a form factor and of a fast algorithm of normalization of contour lines on thickness is proposed in this paper.

### 1. Method of localization of lines based on form-factor

The method for localization of isolated contour lines based on the analysis of value of a form factor – the ratio of the size of the contour line calculated on known coordinates of her ending points to length of the contour line determined by the amount of the contour points which form it - is offered. For direct contour lines this relation shall be close to 1. By this criterion the method allows to select only isolated direct lines which don't have intersections with other lines. The method provides reduction of computing complexity of localization of contour lines due to of rather small number of processed contour pixels.

The flowchart of a method for localization of isolated lines based on form-factor is provided in figure 1.

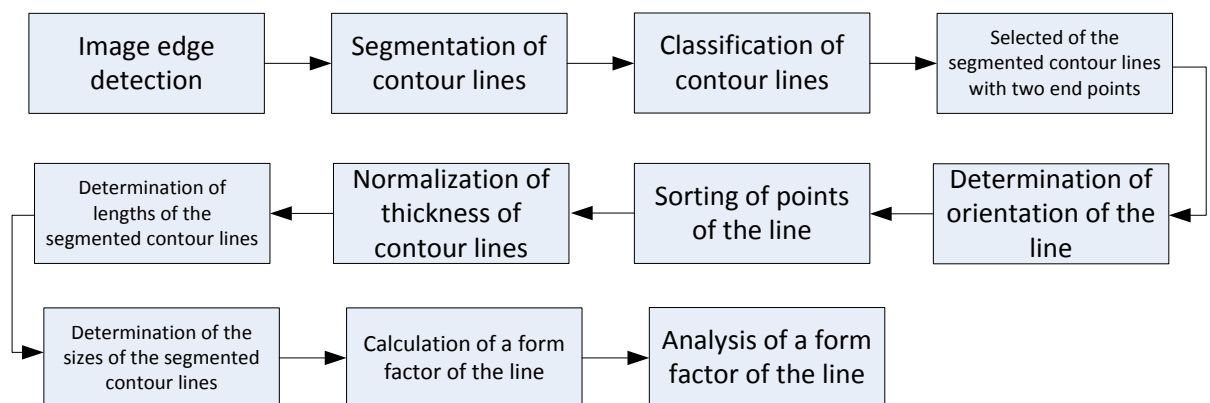


**Figure 1** – flowchart of a method for localization of isolated lines based on form-factor.

The algorithm of localization of isolated direct contour lines based on form-factor consists of the following steps.

- 1) Image edge detection. As a result of contour edge detection of the source image  $I = \|i(y, x)\|_{(y=0, \overline{Y-1}, x=0, \overline{X-1})}$  the binary contour image  $I_B = \|i_B(y, x)\|_{(y=0, \overline{Y-1}, x=0, \overline{X-1})}$  which single pixels define contour points where  $Y, X$  – image sizes on a vertical and a horizontal is created.
- 2) Segmentation of contour lines. To each contour pixel  $i_B(y, x)$  is assigned the number of the line which it belongs. The segmentation matrix  $I_S = \|i_S(y, x)\|_{(y=0, \overline{Y-1}, x=0, \overline{X-1})}$  is created. Values of array elements are concluded in an interval  $[1, N_s]$ , where  $N_s$  – number of contour lines.
- 3) Classification of contour lines. Classification of contour lines is carried out on number of end points. For each segmented the contour line  $l(n)$  formed by pixels  $i_B(y, x) = 1$ , for which the appropriate pixels  $i_S(y, x) = n$  where  $n \in (1, N_s)$ , the number of end points is defined. An end point is the single pixel  $i_B(y, x)$  of a binary contour image which has only one adjacent single pixel  $i_B(y + p, x + q)$  where  $p = \overline{-1, 1}$ ,  $q = \overline{-1, 1}$  and  $p + q \neq 0$ .
- 4) Selected of the segmented contour lines with two end points. From the set of the segmented contour lines  $L_s = \{l_s(n)\}_{(n=1, \overline{N_s})}$  including the shorted, crossed and open circuit isolated lines the subset of contour lines  $L_2 = \{l_2(n)\}_{(n=1, \overline{N_2})}$  which have two end points where  $N_2$  – number of the segmented contour lines with two end points is selected. As a rule, the crossed contour lines have more than two end points. Therefore on this step of algorithm contour lines are selected generally isolated (not having intersections). An exception is intersection of closed and open-ended contour lines. Such exception is processed on the following steps of algorithm.
- 5) Determination of orientation of the line. For the selected contour line on the basis of the found end points orientation is calculated:  $O = \begin{cases} \frac{x_1 - x_2}{y_1 - y_2}, & y_1 \neq y_2 \\ 60, & y_1 = y_2 \end{cases}$ , where  $x_1, y_1, x_2, y_2$  – coordinates of end points of the line.
- 6) Sorting of points of the line. The stack of pixels of the selected contour line is sorted by the bubble sort method on x if the line is drawn out on a x axis, or on y if it is drawn out on a y axis. The stack is sorted by increase, if orientation of the line the negative, and by decrease, if orientation – the positive.
- 7) Normalization of thickness of contour lines. For each contour line excess pixels which are deleted are defined. Excess pixels decide on the help of masks of

$2 \times 2$  pixel and orientation of the line. As a result of geometrical normalization all a contour lines have thickness in one pixel.

- 8) Determination of lengths of the segmented contour lines. For each contour line having two end points  $l_2(n)$  the number of the contour pixels  $s_2(n)$  forming this line  $i_B(y, x)$  by means of expression is defined

$$s_2(n) = \sum_{y=0}^{Y-1} \sum_{x=0}^{X-1} t(m) i_B(y, x) k(n, y, x), \quad (1)$$

where  $k(n, y, x) = \begin{cases} 0, & i_S(y, x) \neq n, \\ 1, & i_S(y, x) = n; \end{cases}$   $t(m)$  - the coefficient depending on a mask

to which belongs pixel (figure 2),  $t(m)=1$  in case of pixel belonging to a direct mask,  $t(m)=1,2$  - to a broken mask and  $t(m)=1,5$  - to an oblique mask.

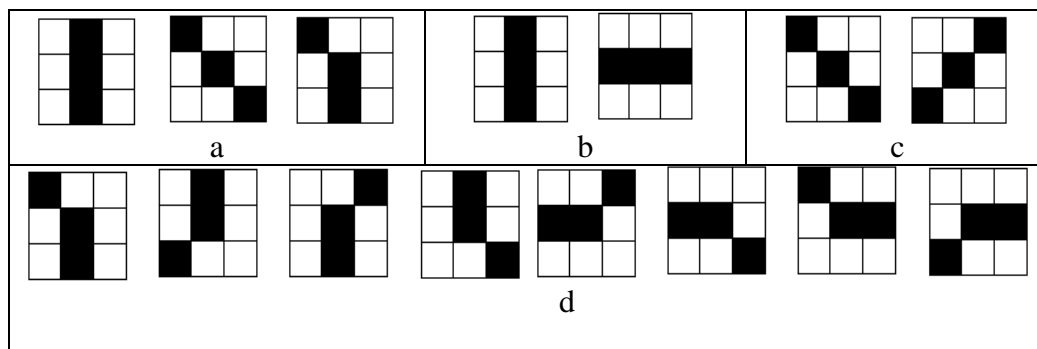


**Figure2** - Classification of generatrixes:

- a – types of generators (direct, oblique, broken);  
b – kind of a direct line; c – kind of oblique;  
d – kind of a broken line.

The number  $s(n)$  is interpreted as length of the contour line.

- 9) Determination of the sizes of the segmented contour lines. For each contour line  $l_2(n)$  having two end points the distance between end points  $r_2(n)$  (the size of the contour line) by means of expression is calculated

$$r_2(n) = \sqrt{(y_1(n) - y_2(n))^2 + (x_1(n) - x_2(n))^2} \quad (2)$$

where  $(y_1(n), x_1(n)), (y_2(n), x_2(n))$  – coordinates of end points of the contour line  $l_2(n)$ .

- 10) Calculation of a form factor of the line. For each contour line  $l_2(n)$  having two end points value of a form factor  $f_2(n)$  of the line by means of expression is calculated

$$f_2(n) = r_2(n)/s_2(n) \quad (3)$$

11) Analysis of a form factor of the line. For each contour line  $l_2(n)$  having two end points comparing of value of its form factor  $f_2(n)$  with 1 is carried out. If value of a form factor  $f_2(n)$  closely to 1, the contour line  $l_2(n)$  is a direct line. Otherwise  $f_2(n) < 1$  the line is a curve or a broken line. Closeness of value of a form factor  $f_2(n)$  of the line to 1 is estimated as a result of comparison of the given threshold  $T_c$  defining curvature of the line to the difference module calculated by means of expression  $|1 - f_2(n)|$ . The contour line  $l_2(n)$  is a direct line if  $|1 - f_2(n)| \leq T_c$ . As a result of execution of this step of algorithm from a subset  $L_2$  the subset  $L_D = \{l_D(n)\}_{(n=1, N_D)}$  of isolated direct contour lines is selected, where  $N_D$  – number of isolated direct contour lines.

Are fixed information on the found isolated direct contour lines (coordinates of end points  $(y_1(n), x_1(n)), (y_2(n), x_2(n))$ , length  $s_2(n)$ , value of a form factor  $f_2(n)$ ).

## 2. Segmentation of contour lines.

Segmentation usually is understood as process of search of uniform areas on the image. This stage very difficult and in a general view not algorithmization up to the end for arbitrary images. The segmentation methods based on determination of the uniform brightness (colors) or homogeneities like textures are most widespread.

In case of existence of stable distinctions in brightness of separate areas of a field of vision threshold methods are applied. Methods of building of areas are effective with steady connectivity in separate segments. It is good to apply a method of edge detection, if edge accurate and stable. The listed methods serve for separation of segments by criterion of uniform brightness. We will note that one of the most effective methods of building of areas assumes a choice of start points or by means of the operator (algorithm of centroid binding), or automatically. Here the method of watersheds based on search of local minima with the subsequent group of areas round them on connectivity is represented effective.

All methods are very acceptable from the point of view of computing expenses, however, for each of them ambiguity of a marking of points in real situations because of need of application эвристик is characteristic (a choice of thresholds of coincidence of brightness, a choice of digital masks, etc.). The algorithms of an acceleration of process of a marking allowing parallel processing on the basis of the logical analysis of adjacent elements have important practical value.

For the description and segmentation of properties of images, exactly, of homogeneity, roughness's, regulars, apply the textural methods sharing conditionally on two categories: statistical and structural. An example of

statistical approach is use of matrixes of the coincidence created of source images to the subsequent count of the statistical moments and entropies. In case of structural approach, for example, on the basis of a Voronoi mosaic, the set of polygons is built. Polygons with the general properties integrate in areas. For research of the general properties often use signs - the moments of polygons.

After segmentation there are noises in a look as separate changes of isolated image elements, and in the form of distortions of some downlink areas. Thus in case of segmentation by separation of boundaries use of the averaging filters masks is impossible as boundaries thus aren't emphasized, and are blurred. Special operators of integral type are applied to underlining of circuits.

The considered methods of segmentation can be reduced to the diagram in figure 3.

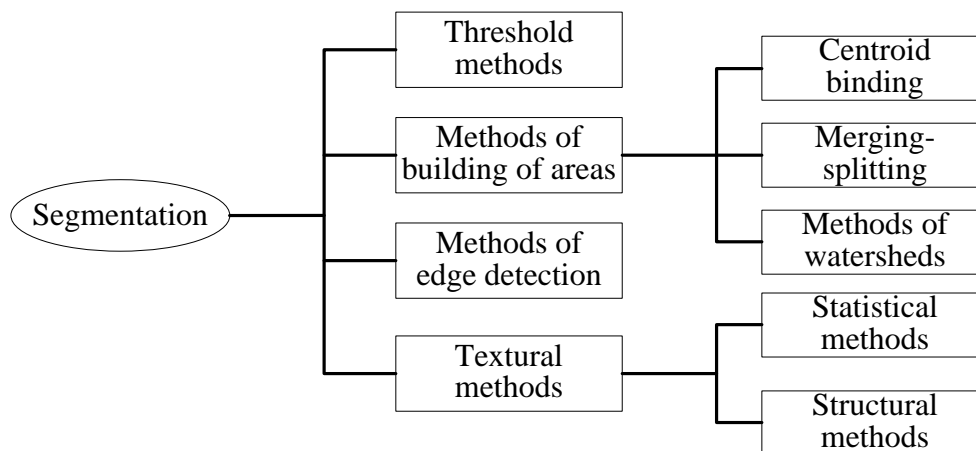


**Figure 3.** Classification of methods of segmentation.

Building of areas - one of the simplest approaches to segmentation for understanding on brightness: adjacent elements with an identical brightness are grouped together and form area.

Brice and Fennem [10] developed the method of building of areas based on a choice of simple rules of growth and a brightness mark. This provides rather exact segmentation of simple scenes with a small number of objects and without texture [10, 11].

In the developed method of localization of lines on the basis of a shape factor the modified Bruce-Fennem's method is used. This method is based not on a brightness sign, and on binary value of pixel, equal 1.

### **3. Normalization of contour lines on thickness**

Among the existing thinning methods the most productive is the algorithm Zong-Suen, however it has the linear dependence from number of the pixels making boundaries [8].



In this algorithm the matrix 3\*3 [12] is entered:

$$\begin{bmatrix} P9 & P2 & P3 \\ P8 & P1 & P4 \\ P7 & P6 & P5 \end{bmatrix}$$

This matrix is superimposed on the image, combining the interesting pixel with P1. Each iteration consists of two subiterations: one aimed at deleting the south-east boundary points and the north-west corner points while the other one is aimed at deleting the north-west boundary points and the south-east corner points. End points and pixel connectivity are preserved.

Iterations are executed until the quantity of the points deleted for iteration doesn't become equal to zero.

This algorithm when processing the contour lines having thickness of 2-3 pixels, a minimum two times processes all pixels from which only 10-20% will be deleted. I.e. the algorithm executes excess iterations that significantly influences processing rate.

The method of normalization of contour lines on thickness based on the shadow-mask analysis of orientation connected and deleting's excess contour pixels is offered. The method allows to increase the speed of contour processing at the expense of the one-fold analysis of each pixel in comparison with the known methods of a thinning using repeated processing of pixels. The entity of a method consists in classification of fragments of the contour line by means of masks, determination of excess contour pixels in these fragments and their deleting. The flowchart of algorithm is provided in figure 4.

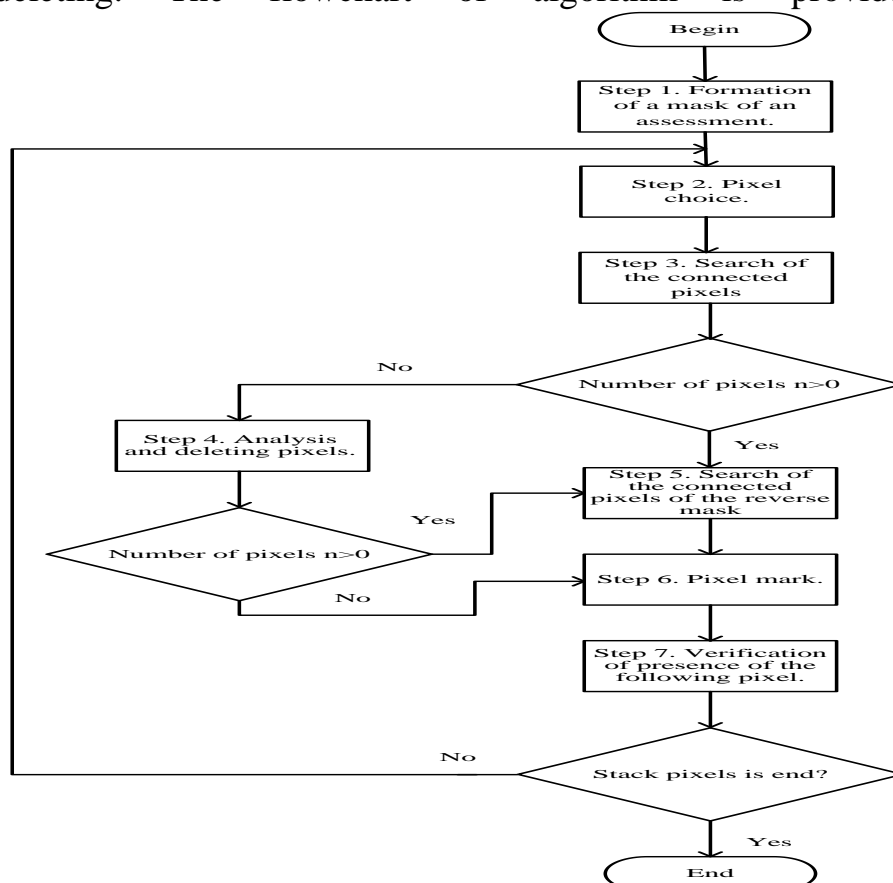


**Figure 4.** Flowchart of algorithm of normalization of the line on width.



**Description of algorithm:**

Step 1. Formation of a mask of an assessment. Masks for the analysis are created based on of the general orientation of the line of size 2x2 pixels (figure 5) relatively checked pixel. The checked pixel of the line is in the upper left corner, if orientation of the line  $O < 0$  (figure 5a), and in the upper right corner, if  $O \geq 0$  (figure 5b). The provided masks are reversed each other.

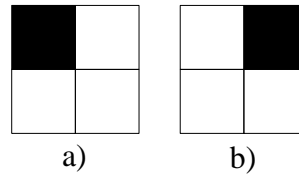


**Figure 5.** The Mask of detection of the connected pixels of the line:  
a) for the line with orientation  $O < 0$ ; b) for the line with orientation  $O \geq 0$ .

Step 2. Pixel choice. From a stack of coordinates of the line not processed and not remote pixel (further reference pixel) is undertakes.

Step 3. Search of the connected pixels. All connected pixels with reference within 1 mask selected on a step are looked for (figure 10). If their quantity from 1 to 3, is carried out transition to a step 4 if pixels aren't found – that go on a step 5.

Step 4. Analysis and deleting pixels. All found pixels are checked for compliance of orientation of the line. For this purpose the deviation

$$r = |d(n) - O| \text{ is calculated, where } d(n) = \begin{cases} 0, & y_1 = y_2, x_1 \neq x_2 \\ 1, & y_1 \neq y_2, x_1 \neq x_2 \text{ - orientation of} \\ 60 & y_1 \neq y_2, x_1 = x_2 \end{cases}$$

the found pixel in a mask rather checked,  $O$  – orientation of the line. All pixels not the appropriate orientations, i.e. with  $r > 0.1$  are deleted if they aren't marked as checked. If the found pixels was 2 and all of them are deleted, for elimination of discontinuity of the line in a consequence of normalization there is an artificial determination of the connected pixel depending on orientation of the line. If  $|O|$  is ranging from 0.5 to 2, the pixel with orientation is artificially decides on. If  $|O| < 0.5$  – the pixel with orientation  $d(n) = 0$  is selected. If  $|O| > 2$  – the pixel with orientation  $d(n) = 60$  is selected. Transition to a step 6 is carried out.

Step 5. Search of the connected pixels of the reverse mask. If within a mask of a pixel aren't found, all connected pixels within the reverse mask are looked for (figure 5). If pixels are found, transition to a step 4 if isn't present – on a step 6 is carried out.

Step 6. Pixel mark. The reference pixel is marked as processed.

Step 7. Verification of presence of the following pixel. If not processed and not remote pixel is present at a stack, transition to a step 3 if isn't present is carried out – that comes an output from algorithm.

Operation of algorithm is resulted by search and deleting excess pixels. Pixels visually and physically thickens contour are superfluous, pixels without which the contour will become thinner, but won't change the parameters of weight.

#### 4. The experimental part.

For an assessment of efficiency of the offered method for localization of isolated contour lines based on form-factor comparing with the LSD method (Line Segment Detector) [6] and method based on Hough transform is carried out it [4]. As criteria of efficiency time and stability of results of localization of direct contour lines on the image are used.

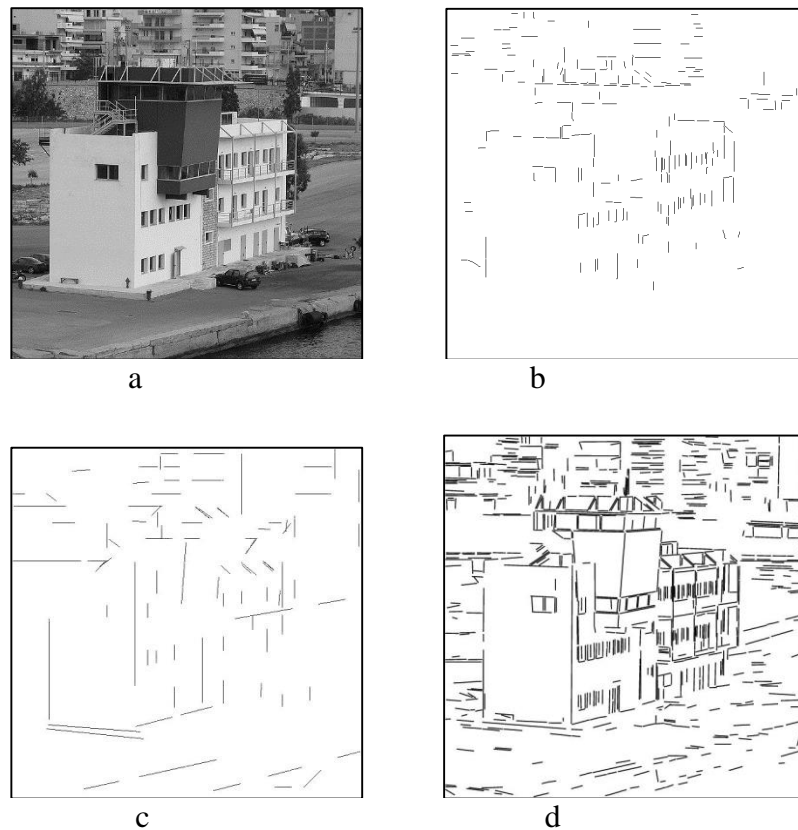
In table 1, the time of localization of direct contour lines is given in the image size  $600 \times 600$  pixels (figure 6a) for the offered method (FFLD – Form-Factor Line Detection), and also the LSD method and method based on Hough transform (HT). The computer on which experiments were made, has the following characteristics: number of cores – 2; processor frequency – 2.0 GHz; bus frequency – 250 MHz; cache memory size: 2.0 GB. For contour processing in the offered method and a method based on Hough transform Canny's filter is used. Follows from table 1 that the offered FFLD method provides a scoring in the speed of localization of direct contour lines by 4 times in comparison with the LSD method and by 14.8 times in comparison with method based on Hough transform.

Table 1 - Time of localization direct contour lines

	FFLD	LSD	HT
Time, c	0,1	0,4	1,48

In figure 6b – 7d, shows the results of localization of direct contour lines in the image by means of the FFLD, LSD methods and method based on Hough transform. In figure 7 and 8 characteristics of stability ( $s$ ) of results of localization of direct contour lines in case of change of brightness ( $\Delta Y$ ) and contrast ( $\Delta C$ ) of the image are provided. Comparison of number of pixels, which saved the location after change of brightness and contrast of the image, on the direct contour lines with total number of pixels, which was of localization on the source image, on the direct contour lines is made for the quantitative assessment of stability.

It is set that the offered FFLD method benefits in stability of position fix of the localization direct contour lines in comparison with method based on Hough transform to 30% and 20%, but loses to the LSD method to 10% and 30% in case of increase and reduction of image brightness respectively (figure 7). In case of increase in contrast the FFLD method benefits in stability against a method based on Hough transform to 10%, but loses to the LSD method to 20% (figure 13). In case of contrast reduction the FFLD method loses in stability to methods based on Hough transform and LSD to 30% and 15% respectively.



**Figure 6.** The localization of direct contour lines:

a) source image; b) results of localization for the FFLD method; c) results of localization for method based on Hough transform; d) results of localization for the LSD method

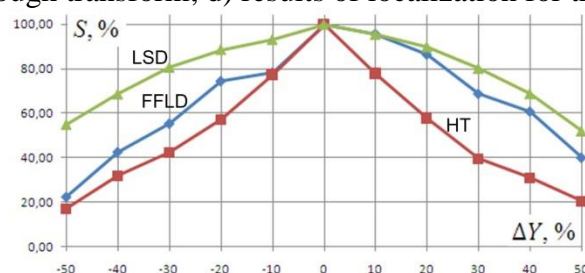


**Figure7.** Characteristics of stability of results of localization of direct contour lines in case of change of brightness for 50%

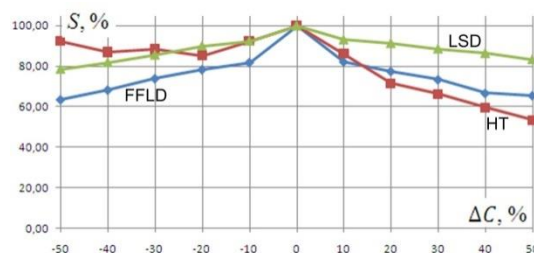


**Figure 8.** Characteristics of stability of results of localization of direct contour lines in case of change of contrast for 50%

The algorithm of normalization of contour lines on thickness is developed for more effective operation of a method of localization of contour lines based on form-factor. This algorithm is realized in language C++ with use of OpenCV 2.4.10 library. For comparison purposes operations of algorithm the most known algorithm of thinning - algorithm Zong-Suen was realized. Experiment is made on a computer with the following technical characteristics: the processor -

Intel(R) Core(TM) i7-4700HQ CPU @ 2.40 GHz; The RAM – 6 GB; type of system – a 64-bit operating system, the processor x64; an operating system – Windows 8.1.

For comparing of operation of algorithms artificially the created line and the line selected on the image was used.

Artificially the created line was used different size (5, 11, 15, 25, 41, 65 and 101 pixels) with curvature of a deviation from 0 to 3 pixels of rather ideal direct line. Each line was round on an angle from 0 to 180 degrees concerning a y axis. Examples of source and processed by the developed method and algorithm Zong-Suen lines are provided in figures 9-12.

Source image and filtered by the Canny method image are provided in figure 13. The line processed by the developed algorithm of normalization and algorithm of Zong-Suen are provided in figure 14.

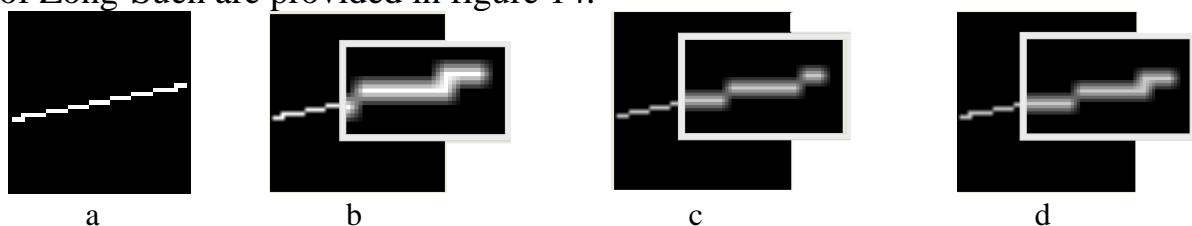


**Fig. 9.** Results of normalization of a direct line on thickness of long 41 pixels and round on 11 degrees:

- a– the source line;
- b – the source line with the selected problem section;
- c – method of normalization of the contour line on thickness with the selected problem section;
- d –Zong-Suen algorithm with the selected problem section.

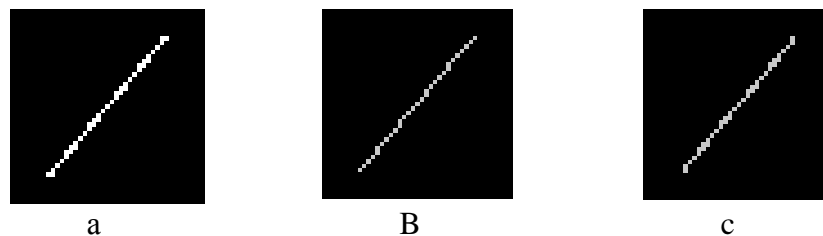


**Figure 10.** Results of normalization of a direct line on thickness of long 41 pixels and the curvature 1 pixel, round on 50 degrees:

- a– the source line;
- b –normalization of the contour line;
- c – Zong-Suen algorithm.

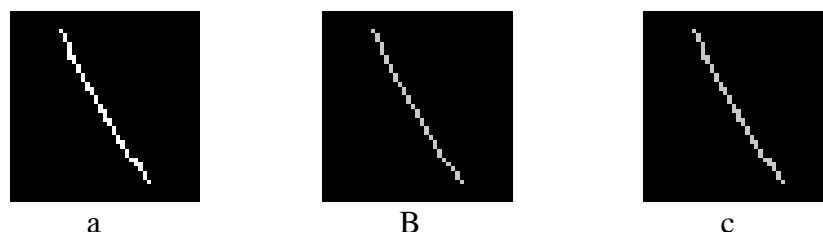


**Figure 11.** Results of normalization of a direct line on thickness of long 41 pixels and the curvature 2 pixel, round on 120 degrees:

- a– the source line;
- b – method of normalization of the contour line on;
- c –Zong-Suen algorithm.

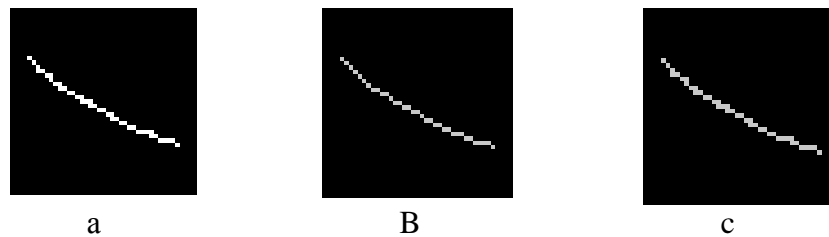


**Fig. 12.** Results of normalization of a direct line on thickness of long 41 pixels and the curvature 3 pixel, round on 150 degrees:

- a– the source line;
- b –normalization of the contour line;
- c –Zong-Suen algorithm.

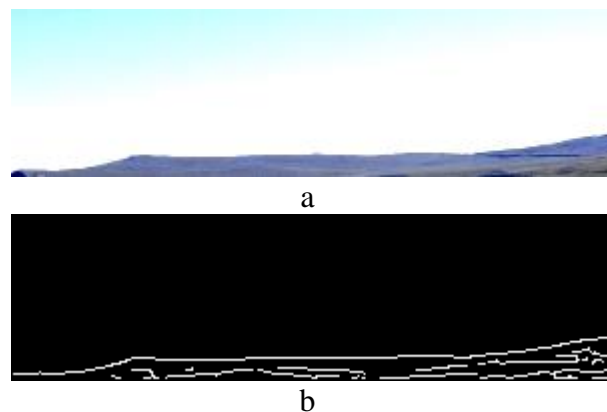


**Figure 13.** The tested image: a – the source image;  
b – the image filtered by Canny's method.



**Figure 14.** Results of normalization of the line of the image on thickness:  
a – method of normalization of the contour line;  
b –Zong-Suen algorithm.

Proceeding from figures 9-12 it is visible that the algorithm of Zong-Suen leaves more "excess" pixels that influences computation of a form-factor.

The assessment of runtime of the developed algorithm of normalization in comparison with algorithm of Zong-Suen is given in table 2.

Table 2 - Comparative assessment of runtime of algorithms

Length of the line, pixels	Algorithm of normalization of the line on thickness, Msec	Algorithm of Zong-Suen, msec
5	0.0570065	0.110769
11	0.101445	0.35529033
15	0.1306015	0.593886
25	0.19512325	1.560834
41	0.29332025	4.1196445
65	0.44578175	10.0513325
101	0.6689235	24.203958

The algorithm of normalization of the contour line on thickness in the developed method of localization of lines based on form-factor is used after segmentation, and algorithm of Zong-Suen – after. The comparative assessment of runtime of segmentation when using each of algorithms is given in table 3.

Table 3 - A comparative assessment of runtime of segmentation when using different algorithms of normalization.

Length of the line, pixels	Algorithm of normalization of the line on thickness, Msec	Algorithm of Zong-Suen, msec
5	0.0387545	0.0395215
11	0.062543667	0.063474
15	0.078612	0.0808365
25	0.11609525	0.118144
41	0.179705	0.1839628
65	0.290381	0.2928783
101	0.4771175	0.4819805

From tables 2 and 3 it is visible that in case of identical costs of segmentation, the provided algorithm works in 1.9..36 times, depending on line length, quicker than algorithm Zong-Suen. It occurs due to smaller number of iterations of the developed method, the one-fold analysis of each pixel of the contour line.

Impact assessments of algorithms of normalization and thinning of the line on determination of a form-factor it is based on calculation of dispersion of the received values of a form-factor for artificial lines and the real image.

Dispersion of a form-factor is calculated on a formula:

$$D = \frac{\sum_{i=1}^n x_i^2 - \frac{\left(\sum_{i=1}^n x_i\right)^2}{n}}{n}, \quad (4)$$

where  $n$  – number of the considered lines of one length for which the form-factor was calculated;  $x_i$  – value of a form-factor of the line.

The diagram of dependence of dispersion of a form-factor on curvature of the line of different length it is given in figures 15-21.

The artificial line long 5 (figure 15), 11 (figure 16), 15 (figure 17), 25 (figure 18), 41 (figure 19), 65 (figure 20), 101 (figure 21) pixels was round from 0 to 180 degrees with a step 1. Curvature of the line 5 pixels long makes 0 and 1 pixels, curvature of the line 11 pixels long – 0-2 pixels, curvature of lines 15, 25, 41, 65, 101 pixel long – 0-3 pixels.

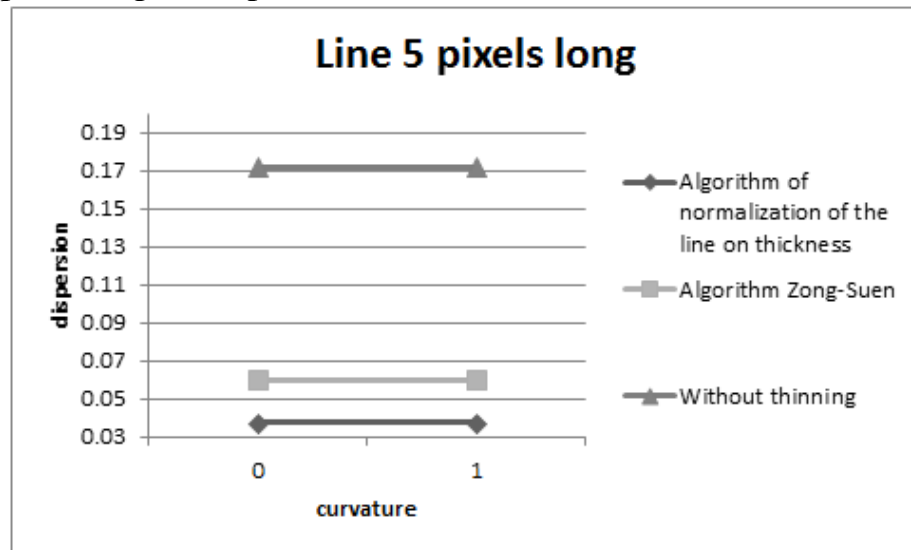


**Figure 15** - Dependence of dispersion of a form-factor on curvature of the line 5 pixels long

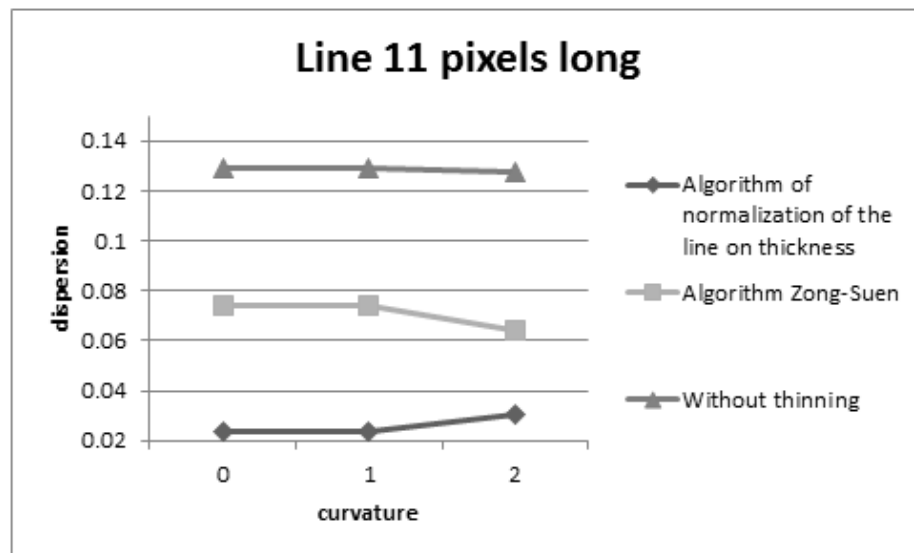


**Figure 16** - Dependence of dispersion of a form-factor on curvature of the line 11 pixels long



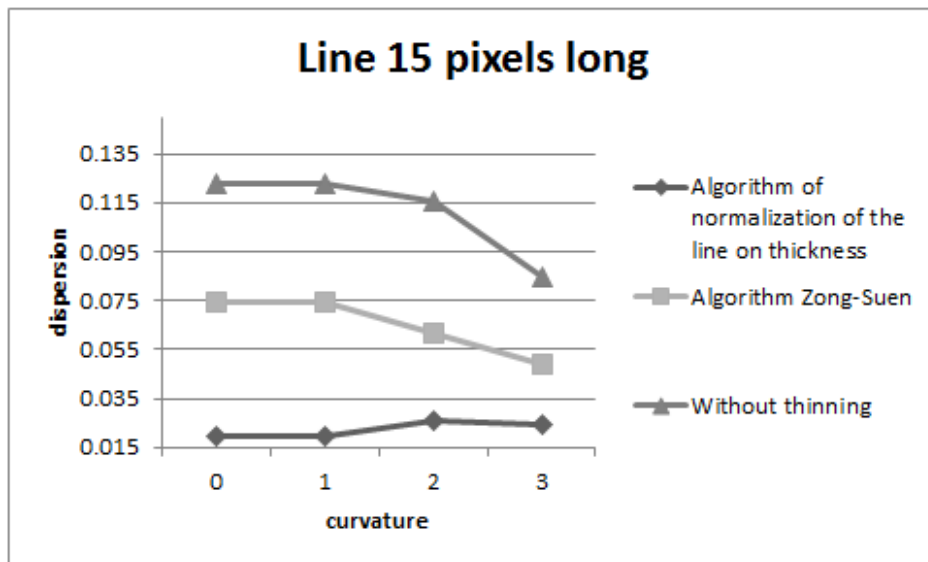


**Figure 17** - Dependence of dispersion of a form-factor on curvature of the line 15 pixels long

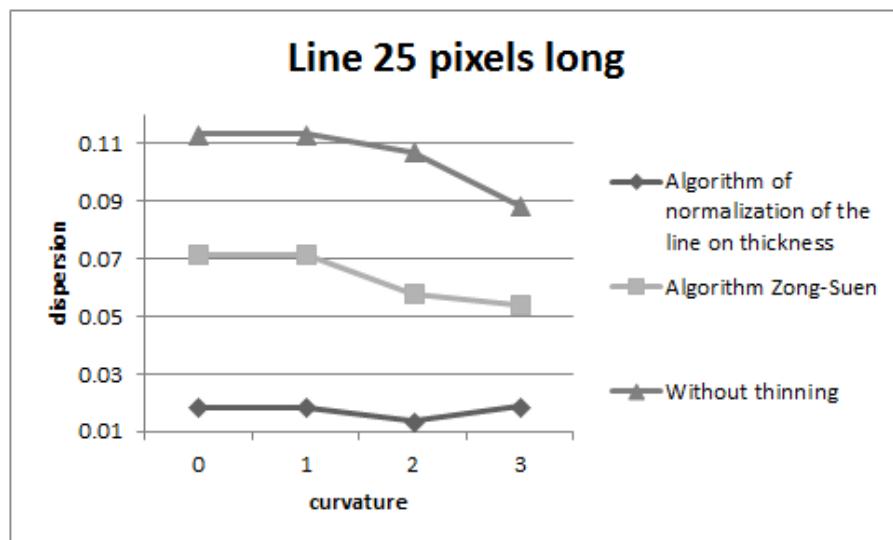


**Figure 18** - Dependence of dispersion of a form-factor on curvature of the line 25 pixels long

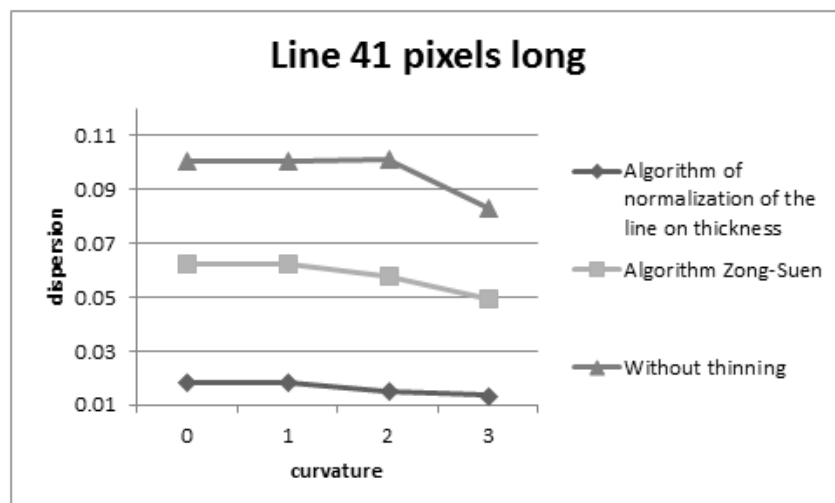


**Figure 19** - Dependence of dispersion of a form-factor on curvature of the line 41 pixels long

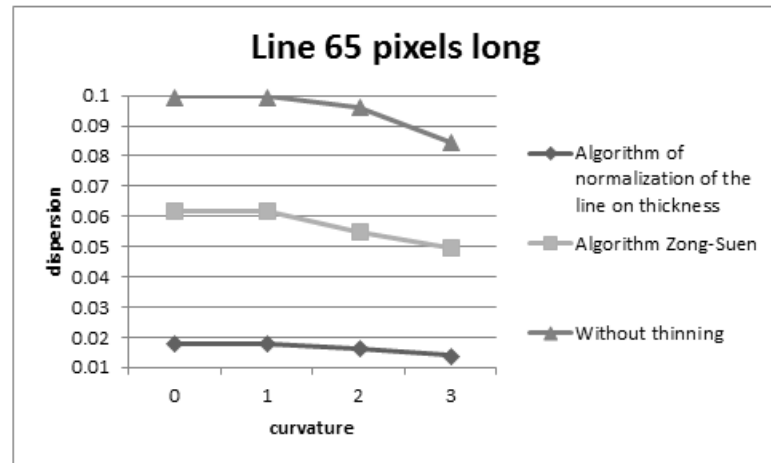


**Figure 20** - Dependence of dispersion of a form-factor on curvature of the line 65 pixels long

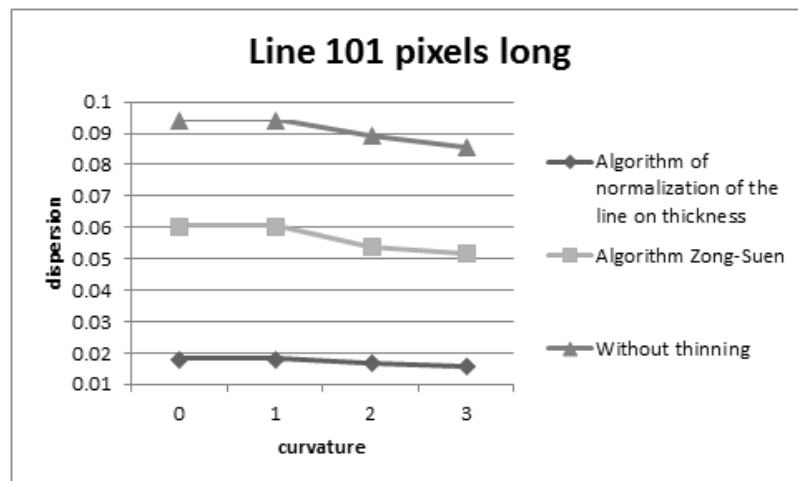


**Figure 21** - Dependence of dispersion of a form-factor on curvature of the line 101 pixels long

From figures 15-21 it is visible that use of a method of normalization or thinning in case of calculation of a form-factor improves dispersion last in case of round of the line. It is also shown that when using of the offered normalization method dispersion on average on 0,05 points is lower, than when using algorithm of Zong-Suen. With insignificant increase in curvature of the line dispersion changes slightly.

In table 4 are provided dispersion of a form-factor depending on the selected method of normalization of the line or without its use in case of round of the image (figure 13a) from 0 to 90 degrees with a step to 15 degrees.

Table 4 – An assessment of dispersion of a form-factor for the line of the image.

	Algorithm of normalization of the line on thickness, msec	Algorithm Zong-Suen, msec	Without thinning, msec
dispersion	0.019484	0.103612	0.166342

Comparing of algorithms of normalization and segmentation on time for the line of the real image is given in table 5.

Table 5 - A comparative assessment of runtime of normalization of the line on thickness and segmentation.

	Algorithm of normalization of the line on thickness, msec	Algorithm Zong-Suen, msec
normalization time	3.203058	92.42205
segmentation time	1.756553	1.980582

From tables 4-5 it is visible that in case of identical time of segmentation the developed algorithm is nearly 30 times faster than algorithm of Zong-Suen. Also developed algorithm of normalization of contour lines on thickness promotes the best calculation of a form-factor by 10 times that is shown in table 4.

### Conclusion

The method of localization of isolated direct contour lines based on form-factor is offered. The entity of a method consists in comparison to unit of value of form-factor – the relations of the size of the contour line (distance between end points) to its length (number of the forming contour pixels). It is set that the offered method provides a scoring in the speed of localization of direct contour lines by 4 times in comparison with the LSD method and by 14,8 times in comparison with method based on Hough transform. It is shown that the offered method benefits in stability of position fix of the localization direct contour lines in comparison with method based on Hough transform to 30%, but loses to the LSD method to 30% in case of image brightness change. In case of increase in contrast the offered method benefits in stability against a method based on Hough transform to 10%, but loses to the LSD method to 20%. In case of contrast reduction the offered method loses in stability to methods based on Hough transform and LSD to 30% and 15% respectively.

The effective method of normalization of the contour line on thickness on the basis of the analysis of orientation of the connected pixels is developed. It is shown that the method works in 1.9..36 times quicker than algorithm Zong-Suen. To shortcomings of a method the impossibility of its application belongs to lines more than 3 pixels thick, on what the main methods of a thinning are directed. However this method is specially developed for deleting excess pixels of a dedicated line.

## References

1. Lowe, D. Distinctive image features from scale invariant keypoints/ D. Lowe// International J. of Computer Vision. – 2004. – Vol. 60, № 2. – P. 91–110.
2. Bay, H. SURF: Speeded up robust features/ H. Bay// Proc. of the 9th European Conference on Computer Vision. – Graz, Austria, 2006. – Vol. 3951. – P. 404–410.
3. Hirschmuller, H. Realtime correlation-based stereo vision with reduced border errors/ H. Hirschmuller, J.M. Garibaldi// International J. of Computer Vision. – 2002. – Vol. 47, № 1–3. – P. 229–246.
4. Duda, R.O. Use of the Hough Transformation to Detect Lines and Curves in Pictures/ R.O. Duda// Communication of the ACM. – 1972. – Vol. 15, № 1. – P. 229–246.
5. Anver, M.M. Fuzzy edge detection using competition between multiple masks/ M.M. Anver, R.J. Stonier// Proc. of the 2nd International Conference on Computational Intelligence, Robotics and Autonomous Systems, CIRAS 2003. – Singapore, 2003. – P. 344–348.
6. LSD: A Fast Line Segment Detector with a False Detection Control/ R. Grompone von Gioi [et al.]// IEEE Transactions on Pattern. Analysis and Machine Intelligence. – 2010. – Vol. 32, № 4. – P. 722–732.
7. Chan, T.S. Line detection algorithm/ T.S. Chan, K.K. Raymond// Proc. of 13<sup>th</sup> Int. Conference on Pattern Recognition, ICPR 1996. – Vienna, 1996. – P. 126–130.
8. T. Y. Zhang, C. Y. Suen. A fast parallel algorithm for thinning digital patterns// Commun. ACM, vol. 27, no. 3, pp. 236--239, 1984.
9. Молчанова, Грунский. Решение задачи топологического утончения объектов бинарного растра с использованием специализированных агентов.// Информационные управляющие системы и компьютерный мониторинг (ИУС КМ 2013)
10. Brice C. R., Fenema C. L., Scene Analysis Using Regions, Artificial Intelligence, 1, 205-226 (1970).
11. Barrow H. G., Popplestone R. J., Relational Descriptions in Picture Processing, in: Machine Intelligence, Vol. 6, Meltzer B., Michie D., Eds., University Press, Edinburgh, 1971, pp. 377-396.
12. Р. Гонсалес, Р. Вудс Цифровая обработка изображений — М: Техносфера, 2005 – 1007с

## **Numerical Simulation to Study the Effect of Combination Vertical Load and Lateral Load on Pile Performance in Cohesionless Soil**

**Hussein A. Shaia**

**College of Engineering, University of Thi-Qar/ Iraq**

### **Abstract**

Pile foundation is widely subjected to both vertical and lateral loads. The available design procedure assumes that the effect of these two loads is independent of each other and hence the pile design is carried out separately for vertical and lateral loads. The traditional methods for analysis of piles according to sub-grade reaction methods also do not consider the effect of interaction between the different load directions. The effect of combination vertical loads and lateral on pile performance that installed in cohesionless soils is considered in this paper through three-dimensional finite element analyses. In the numerical model, the pile was treated as a linear elastic material and the soil was idealized using the Mohr-Coloumb constitutive model. The results from the analysis of single piles under combined vertical and lateral loads are studied in this paper. The influences of related parameters such as shear strength (angle of internal friction and dilatation angle) of soil in term of loose and dense sands and pile/soil interface friction coefficient have also been studied in this work. The results have shown that the combination vertical load and lateral has a significant effect on the pile performance that installed in cohesionless soil.

**Key Words:** FEM model, Pile, cohesionless soil, lateral load, deflection, interface friction.

## المحاكاة العددية لدراسة التأثير المتداخل للحمل الرأسي و الحمل الجانبي على استجابة الركيزة المثبتة في التربة غير المتماسكة

د. حسين عبد شايح  
كلية الهندسة-جامعة ذي قار

### الملخص

أسس الركائز غالباً ما تتعرض إلى أنواع الأحمال الرأسية والجانبية. أن طريقة التصميم المتوفرة والمستخدم حالياً تفترض أن تصميم الركائز تحت تأثير هذه الأحمال يجب ان يتم بشكل منفصل لكلا الأحمال الرأسية أو الجانبية. الطرق التقليدية الخاصة بتحليل الركائز وفقاً لطرق رد فعل التربة الطبيعية أيضاً لا تأخذ بنظر الاعتبار تأثير دمج كل من الأحمال ذات الاتجاهات المختلفة. لذلك فإن تأثير دمج كل من الأحمال العمودية والاحمال الجانبية للذات تتعرض له الركيزة المثبتة والمغروسة في التربة الغير متماسكة تم أخذها بنظر الاعتبار ودراستها وتحليلها باستخدام طرق المحاكاة العددية لنموذج ممثل بركيزة ثلاثية الأبعاد. تم في هذا النموذج تمثيل الركيزة على انها تتصرف بطريقة خطية ومرنة اما التربة المحيطة بالركيزة فقد تم تمثيل تصرفها باستخدام دالة أذعان موهر- كولومب. تم في هذه الدراسة تحليل النتائج المستحصلة من تعرض أساسات الركائز لتأثير دمج كل من الأحمال العمودية والجانبية. بالإضافة الى دراسة تأثير قوة القص للتربة والمتمثلة بزواوية الاحتكاك الداخلي وزاوية تمدد حبيبات من حيث حالات التربة المفككة والمرصوصة وكذلك معامل الاحتكاك البيئي بين الركيزة والتربة تم دراسة تأثيره أيضاً. وقد أظهرت النتائج أن دمج كل من الحمل العمودي والحمل الجانبي للذات تتعرض له الركيزة المثبتة في التربة غير المتماسكة له تأثير كبير على ادائها.

## Introduction

Piles have been used extensively for supporting vertical and lateral loads for various structures including heavy buildings, transmission lines, power stations, and highway structures. These piles are not only used to support vertical loads, but also lateral loads and combination of vertical and lateral loads. (Rajagopal and Karthigeyan 2011). According to the current design practice, piles are independently analyzed first for the vertical load to determine their bearing capacity and settlement and for the lateral load to determine the flexural behaviour. This approach is valid only for small lateral loads, however, in case of coastal/offshore applications, the lateral loads are significantly high of the order of 10–20% of the vertical loads and in such cases, studying the interaction effects due to combined vertical and lateral loads is essential, which calls for a systematic analysis (Moayed et al. 2012).

Several investigators have attempted to study the behaviour of piles and pile groups under pure lateral loads [(Mahmoud and Burley 1994), (Abbas et al. 2008), (Basu et al. 2008)]. Besides, with the advent of latest generation computers, it is now possible to investigate the effects due to non-linearity and elasto-plasticity of soil medium, asymmetric loading on piles etc. using 2-dimensional finite element analysis [(Brown and Shie 1991), (Yang and Jeremić 2002), (Chik et al. 2009) and (Mardfekri et al. 2013)]. However, there is hardly any concerted effort to study the influence of vertical load on the lateral response of piles and the literature on combination of vertical and lateral loads is scanty. The limited information on this aspect based on the analytical investigations (Davisson and Robinson 1965) and (Banerjee and Davies 1978) reveals that for a given lateral load, the presence of vertical load increases the lateral deflection. However, laboratory (Jain et al. 1987) and field investigations [(Soroohan and Bykov 1976) (Zhukov and Balov 1978) (Pando et al. 2003)] suggest a decrease in lateral deflection under the presence of vertical loads. Anagnostopoulos and Georgiadis, (1993) have reported that the modified status of soil stresses and local plastic volume changes in the soil continuum under combined vertical and lateral loads cannot be accounted for in general by the conventional subgrade reaction and elastic half space methods of analysis. Trochanis et al.,(1991) attempted to study the behaviour of a pile under combined vertical and lateral loads based on 3-dimensional finite element method. The emphasis was mainly focused on the influence of lateral load on the vertical response of a pile rather than the influence of vertical load on the lateral response of piles. However, since piles are not often structurally designed to resist lateral loads, the lateral response of piles is more critical and interesting for design engineers. In view of the above stated issues, the present paper focuses on the effect of vertical load on the lateral response of piles. The effects of factors such shear strength (angle



of internal friction and dilatation angle) of soil in term of loose and dense sands and pile/soil interface friction coefficient are highlighted.

### Numerical Model

Recently, there is a growing number of mature FEM commercial software in international market (e.g Adina, Crisp, Ansys, Abaqus and Plaxis). Among them Abaqus and Ansys are the widely used FEM software in the geotechnical engineering and Abaqus is one of these software's dealing with elastic-plastic, nonlinear and contact problems. Therefore, Abaqus software is adopted to analyse the effect of combined vertical load and lateral load behaviour of single pile embedded in cohesionless soil. The schematic diagram of the single pile subjected to vertical load and lateral load is shown in Figure 1.

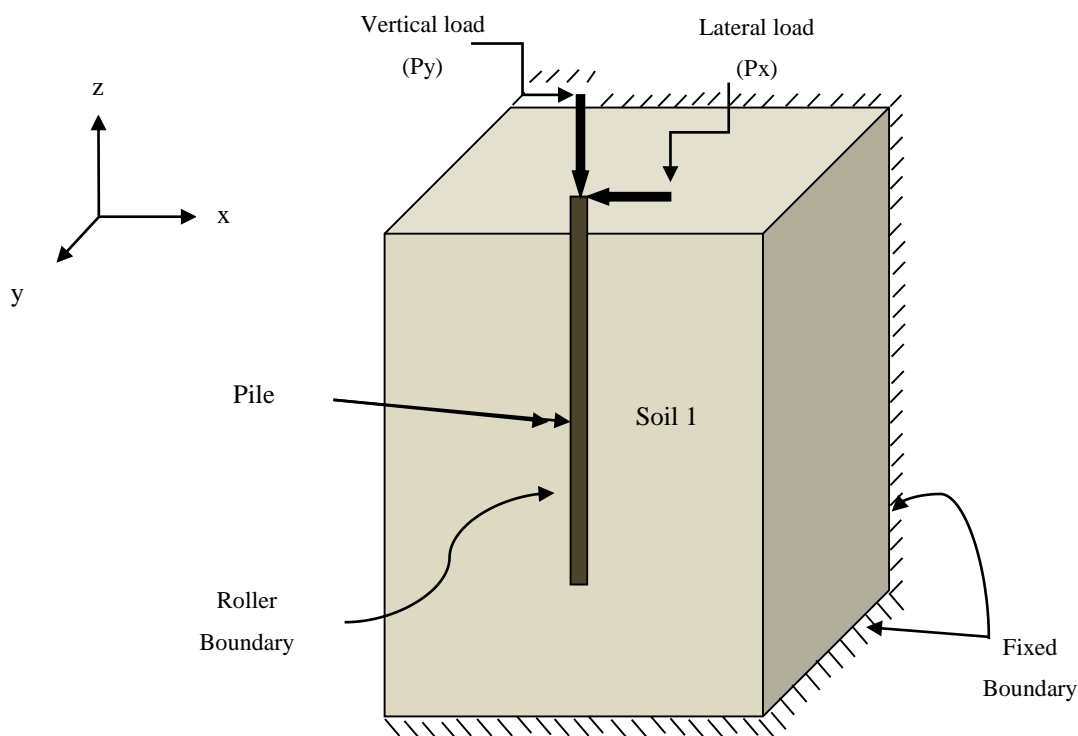


Figure 1: Schematic Diagram of the Axisymmetric Pile/soil model Subjected to Vertical and Lateral Loads

The solid elements were used to model the pile and the soil elements using 8-node linear brick, reduced integration, and hourglass control. The material behaviour of the concrete pile was assumed to be linear elastic. The surrounding sand is described by elasto-plastic material obeying Mohr-Coulomb failure criterion. A pile diameter of  $D=1.5$  m and 35 m length was considered. The material behaviour of the pile was assumed to be linear elastic with the parameters  $E=25000$  MPa (Young's modulus) and  $\nu=0.2$  (Poisson's ratio) for concrete. The set of soil properties for both loose and dense cases considered are shown in Table 1. The soil

properties for loose and dense states were arrived at using correlations between SPT N-values and Young's modulus for soil (Bowles 1988).

Table 1: Material parameters used for soil

Property	Loose sand	Dense sand
Young Modulus, E (MPa)	16.0	50.0
Poisson's ratio, $\nu$	0.30	0.30
Internal friction, $\phi^\circ$	27	35
Dilatation angle, $\psi^\circ$	5	11
Unit weight $\gamma$ (kN/m <sup>3</sup> )	17	21

The contact behaviour at the pile-soil surface was modeled by “hard” contact in normal direction and Coulomb friction in tangent direction. The Mohr-Coulomb model is based on plotting Mohr's circle for states of stress at yield in the plane of the major and minor axis, ( $\sigma_1$  and  $\sigma_3$ ) respectively (Verruijt and Van Baars 2007). The yield line is the best straight line that touches these Mohr's circles (Figure 1).

There is no tension sustained between pile and sand and no slip occurred when tangential shear stress is lower than the shear resistance determined by normal pressure and friction coefficient of interface. The friction interface angle of pile-soil is set as 0.75 times of internal friction angle of sand.

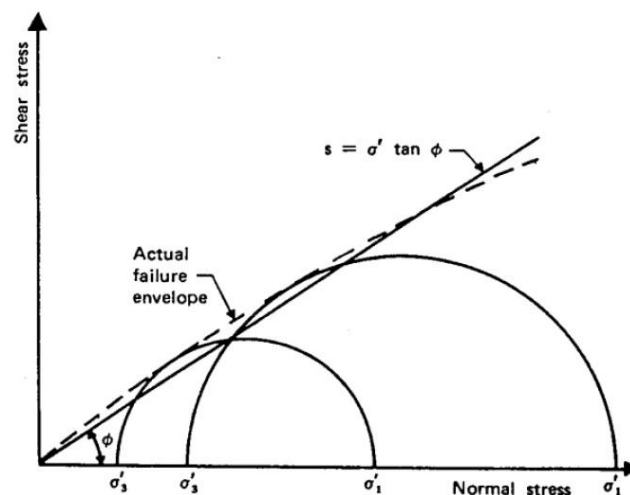


Figure 1: Mohr-Coulomb Failure Criterion

### Model features

For the investigation of the influence of vertical loads on the lateral response of piles installed in sandy soil, a three-dimensional (3-D) numerical model was established. The computations were done using the finite element program system ABAQUS. Due to the symmetric loading condition only a half-cylinder representing the sub-soil and the pile was considered. For that, an idealized homogeneous soil consisting of loose and dense sands were considered. Due to the symmetric loading condition only a half-cylinder representing the sub-soil and the pile was considered. The boundary condition of the both sides of model was 10 times that of the pile diameter (Vipulanandan et al. 1989). The distance between the bottom of pile and soil bottom boundary is 12 m. With these model lengths the calculated behaviour of the pile is not influenced by the boundaries (Sakr and Hesham El Naggar 2003). A view of the discretized model area is given in Figure 2. The interaction behaviour between the pile and the sand soil is simulated using contact elements. The maximum shear stress in the contact area is determined by a friction coefficient. Boundary (or support) conditions for models must be specified before executing the finite element analysis. Without specifying adequate constraints the structure will be free to move as a rigid body. In the specified load transfer problem two separate boundary conditions were utilized. The nodes at the base and outer bounds of the mesh were fixed against displacement while the nodes in the symmetric plane (dividing the problem domain) were allowed to translate along the x and z axes. A total of 4484 elements, 5561 nodes were used for this analysis.

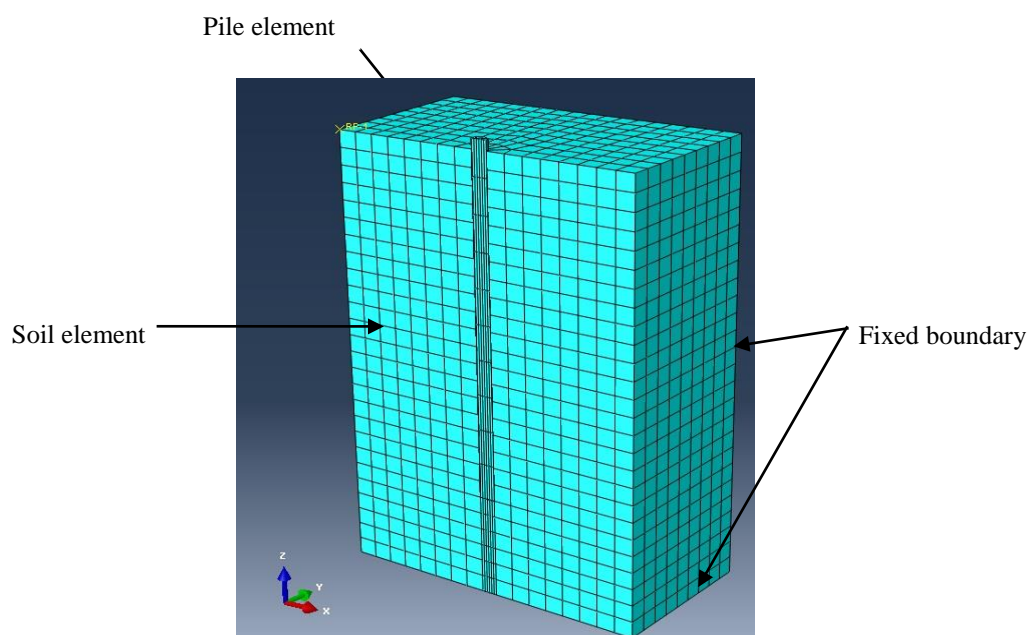


Figure 2: Axisymmetric Finite Element Model of the Pile/Soil Model

## Results and discussion

A series of numerical analyses have been conducted to study the behaviour of piles under pure lateral loads and the effect of vertical load on the lateral response of piles. Several parameters were considered in this parametric study namely, (i) shear strength parameters (angle of internal friction and dilatation angle) in term of loose and dense sands (ii) pile/soil interface friction angle.

### *Effect of soil parameters*

In the present analysis, the combine of vertical load ( $P_y$ ) and lateral load ( $P_x$ ) were applied at the head of the pile. The response of pile under combined loading was analyzed separately with different vertical load levels that equal to zero (pure lateral load),  $0.25P_x$ ,  $0.5P_x$ , and  $0.75P_x$  by separate numerical analyses. The combine vertical load and the horizontal load are applied simultaneously and increased gradually until the required maximum loads are reached. At the first stage, the ultimate lateral load ( $P_x$ ) capacity of pile model was evaluated a priori by separate numerical analyses. The ultimate lateral load of pile is obtained from load deflection curves which corresponding to a displacement of (10-20%) of the pile diameter (Chawhan et al. 2012). Figure 3 shows the pure lateral load vs. deflection relationship of pile embedded in loose and dense sand. It is noted from the figure that the horizontal deflection increases as the lateral load is increased up to about a 1200-kN pile load, at which a pile lateral displacement of about (10-20%) of the pile diameter. Shortly after that, the pile moves laterally at a greater rate, indicating that the lateral load capacity of the pile has been reached. The Figure also shows that the deflection of the pile increase at the maximum load in loose sand case compared to that obtained from the dense sand. This is expected response due to the soil in the dense case having higher stiffness than the loose sand.

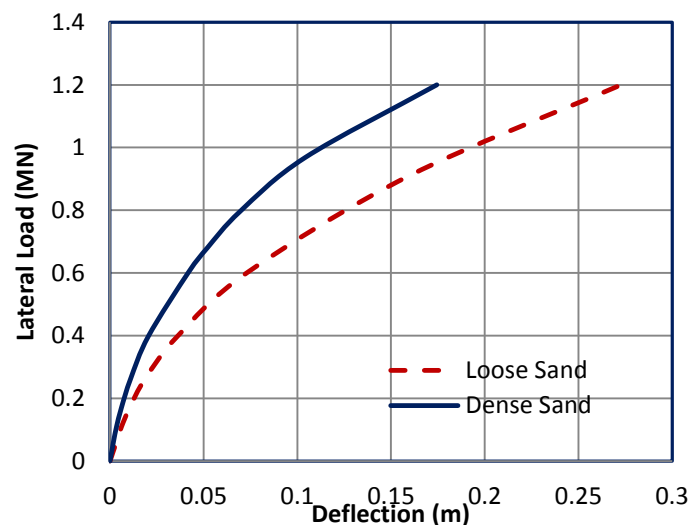


Figure 3: Load Deflection Response for Piles in Loose and Dense sand

The level of vertical load was applied first and then in the second stage, the ultimate lateral load was applied on the node corresponding to the pile head. The reaction forces developed at

the nodes were used to calculate the lateral displacements corresponding to the applied lateral load ( $P_x$ ). The analysis was performed using load control (rather than displacement control) so as to know the displacement developed at various vertical load levels.

The response of piles in dense and loose sands is shown in Figures 4 and 5. It is seen from these figures that the vertical load has only a marginal influence on the lateral response of piles in the case of loose sands compared to that in dense sand. It can be noted that, in the case of dense sands, there is an increase in lateral bearing capacity with increasing vertical loads. This could be attributed to the following: (i) under the influence of vertical loads, higher vertical soil stresses develop in the soil along the pile surface leading to higher lateral stresses in the soil, (ii) higher lateral stresses in turn mobilize larger friction forces along the length of the pile. However, it is clear that the lateral soil stresses are not much affected by vertical loads in the case of loose sand as shown in Figure 5. On the other hand, the lateral stresses for dense sands increase because of the presence of vertical load as illustrated in Figure 4. The increase of lateral soil stresses leads to the development of higher lateral loads in the case of dense sands.

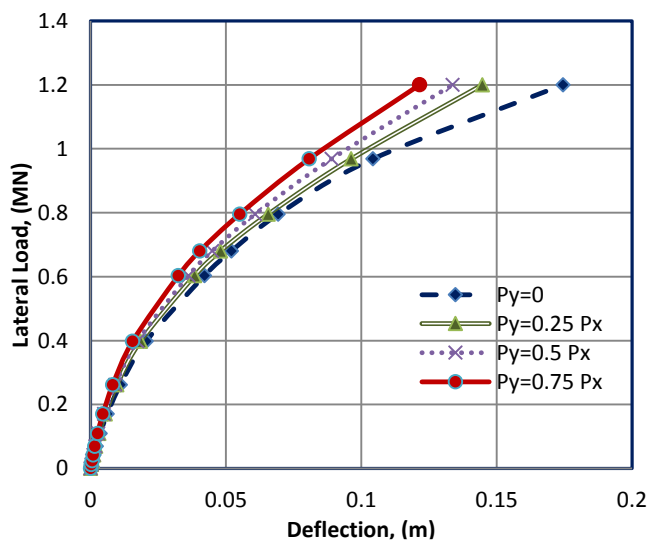


Figure 4: Lateral Load-Deflection Behaviour of a Pile in Dense Sand

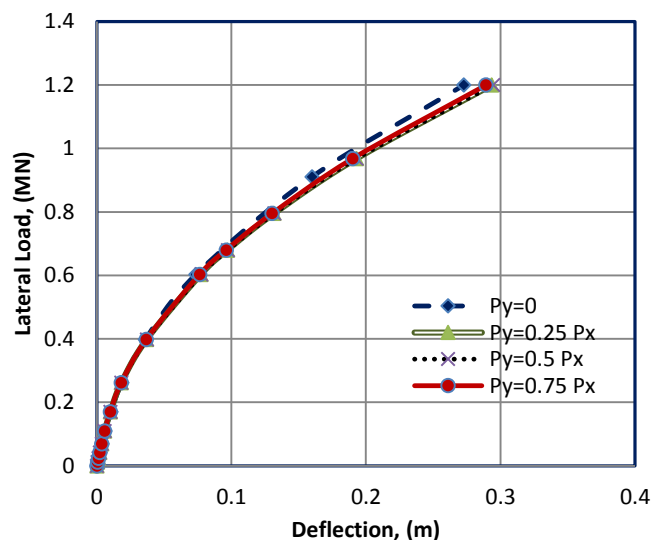


Figure 5: Lateral Load-Deflection Behaviour of a Pile in Loose Sand

This is further illustrated through lateral soil stresses developed in front of the pile at different vertical load levels for a lateral deflection, as shown in Figures 6 and 7 for loose and dense sands respectively. It is clear that the lateral soil stresses are not much affected by vertical loads in the case of loose sand as shown in Figure 6. On the other hand, the lateral stresses for dense sands increase because of the presence of vertical load as illustrated in Figure 7. The increase of lateral soil stresses leads to the development of higher lateral loads in the case of dense sands.

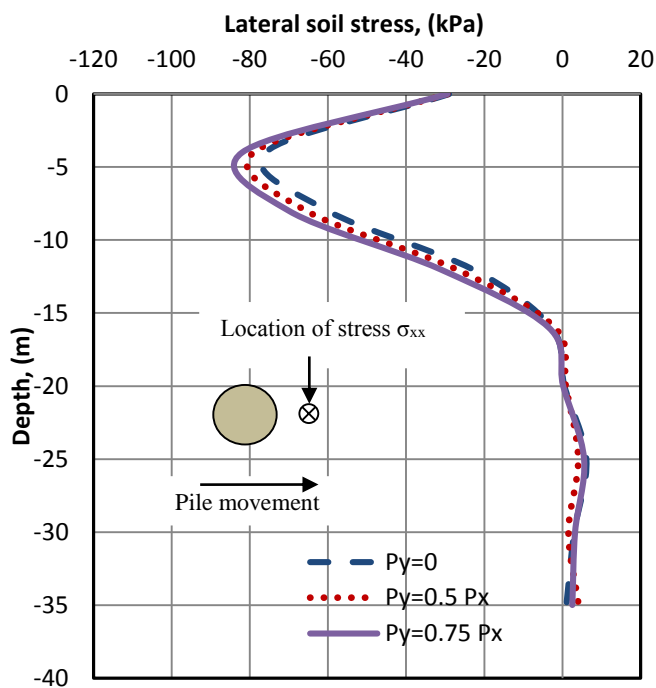


Figure 6: Variation of Lateral Soil Stress ( $\sigma_{xx}$ )  
infront of the Pile in Loose Sand

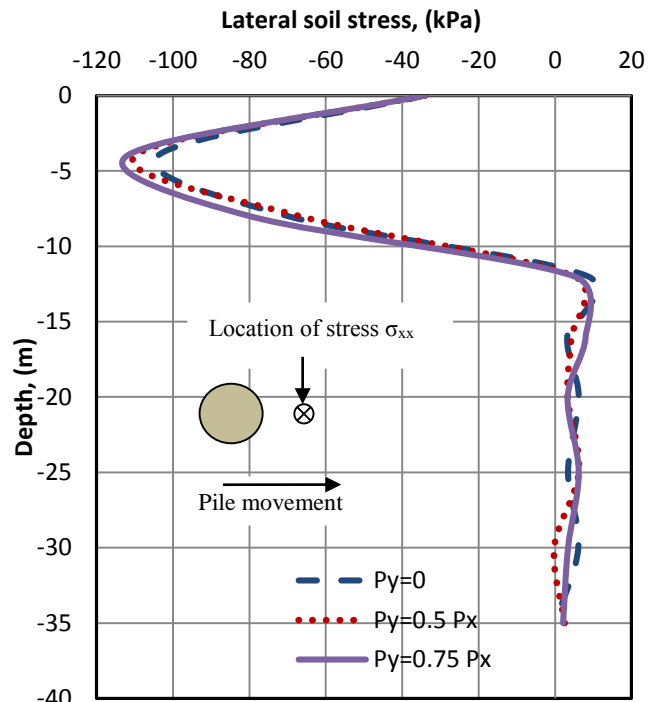


Figure 7: Variation of Lateral Soil Stress ( $\sigma_{xx}$ )  
Infront of the pile in Dense Sand

### *Effect of Interface Friction Coefficient*

In order to verify the numerical model results with those obtained from experimental model, the FRP pile/sand model was simulated using the contact property technique in term of interface friction. The interaction relationship between pile and soil around and bottom pile can simulate the penalty contact-type (Pan et al. 2011). This type of interface friction is capable of simulating the interface friction between the pile surface and the soil in contact (Sam 2007). The external surface of the pile and pile tip are contacted with the soil as shown in Figure 8. The ABAQUS interface modelling technique is used to simulate slip at the soil/pile interface (ABAQUS 2010). ABAQUS uses the Coulomb frictional law in which frictional behaviour is specified by an interface friction coefficient,  $\mu$ .

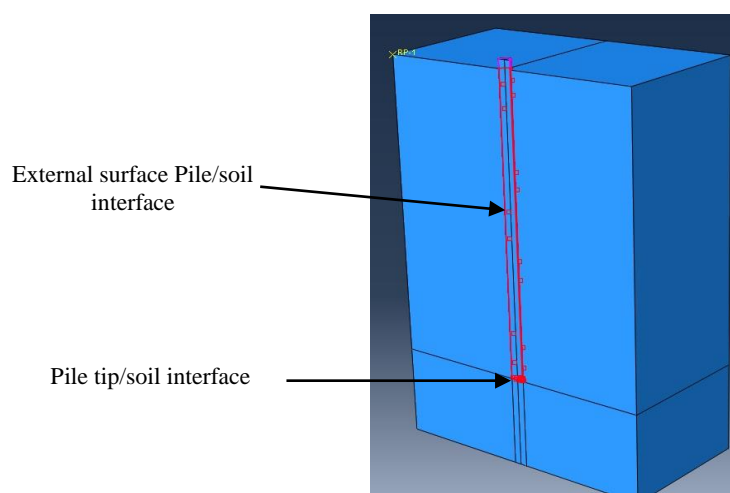


Figure 8: The Interface Friction Elements

As the previous results have clearly shown that the influence of vertical load is more prominent in the case of dense sands, the influence of interface friction coefficient was study only for the ( $P_y=0.5P_x$ ). To investigate the effect of interface friction coefficient, a three FE analyses were conducted for both soil state (loose and dense). These analyses were conducted using three different interface friction coefficients (0.22, 0.32, and 0.42) respectively. The comparison, in term of the pile load deflection was presented in Figure 9. As a result it can be seen that that both cases behaved in a similar manner between three analyses. It is clear that the coefficient of interface friction vertical loads have very little influence on the lateral deformations during the applied vertical load on both loose and dense sand.

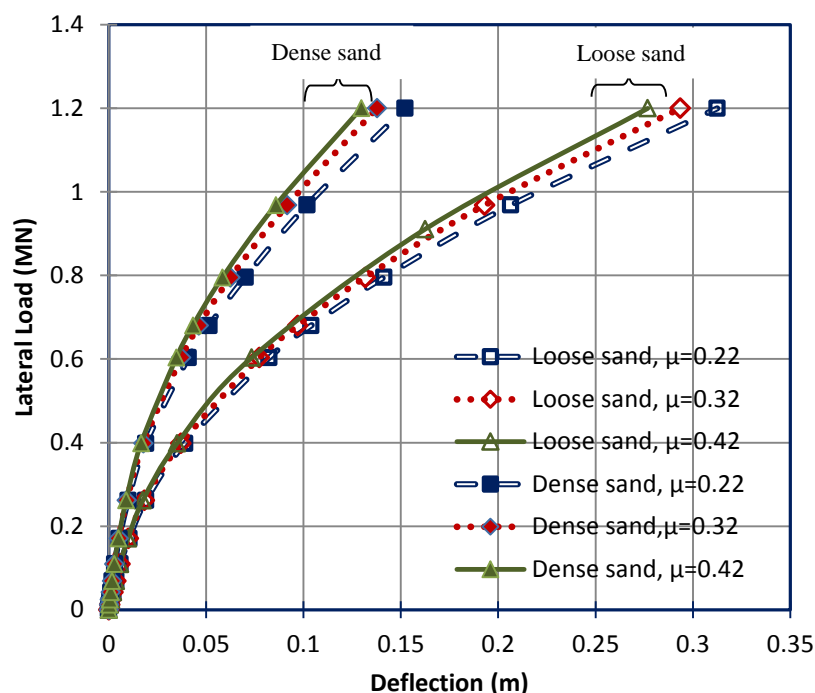


Figure 9: Effect of Interface Friction Coefficient on Lateral Load-Deflection Response Pile in Dense and Loose Sands

## Conclusions

The behaviour of single pile subjected to combined vertical and lateral loads has been investigated in this study through a series of three-dimensional analysis using Abaqus software. The single pile under combined loading was analyzed separately with different vertical load levels that equal to zero (pure lateral load),  $0.25P_x$ ,  $0.5P_x$ , and  $0.75P_x$  by separate numerical analyses. The influences of related parameters such as shear strength (angle of internal friction and dilatation angle) of soil in term of loose and dense sands cases and pile/soil interface friction coefficient. The results show that the behaviour of pile under combination of vertical and lateral loads has larger resistance to lateral load as compared to



pile under pure lateral load only for the case in dense sand. The reason could be directly attributed to the development of additional lateral soil stresses in front of the pile and additional frictional resistance developed along its length. The coefficient of interface friction between the pile and sand has a minor effect on the pile response when subjected to lateral load during the applied vertical load in both loose and dense sand cases.

## References:

- ABAQUS. (2010). *Abaqus Analysis User's Manual* Providence.
- Abbas, J. M., Chik, Z. H., and Taha, M. R. (2008). "Single pile simulation and analysis subjected to lateral load." *Electronic Journal of Geotechnical Engineering*, 13, 1-15.
- Anagnostopoulos, C., and Georgiadis, M. (1993). "Interaction of axial and lateral pile responses." *Journal of geotechnical engineering*, 119(4), 793-798.
- Banerjee, P., and Davies, T. (1978). "The behaviour of axially and laterally loaded single piles embedded in nonhomogeneous soils." *Geotechnique*, 28(3), 309-326.
- Basu, D., Salgado, R., and Prezzi, M. (2008). "Analysis of Laterally Loaded Piles in Multilayered Soil Deposits." *Joint Transportation Research Program*, 330.
- Bowles, J. E. (1988). *Foundation analysis and design*.
- Brown, D. A., and Shie, C.-F. (1991). "Some numerical experiments with a three dimensional finite element model of a laterally loaded pile." *Computers and Geotechnics*, 12(2), 149-162.
- Chawhan, B., Quadri, S., and Rakaraddi, P. "Behavior of Lateral Resistance of Flexible Piles in Layered Soils."
- Chik, Z., Abbas, J., Taha, M., and Shafiqu, Q. (2009). "Lateral Behavior of Single Pile in Cohesionless Soil Subjected to Both Vertical and Horizontal Loads." *European Journal of Scientific Research*, 29(2), 194-205.
- Davisson, M., and Robinson, K. "Bending and buckling of partially embedded piles." *Presented at Soil Mech & Fdn Eng Conf Proc/Canada/*.
- Jain, N., Ranjan, G., and Ramasamy, G. (1987). "Effect of vertical load on flexural behaviour of piles." *Geotechnical Engineering*, 18(2).
- Mahmoud, M., and Burley, E. (1994). "Lateral load capacity of single piles in sand." *Proceedings of the ICE-Geotechnical Engineering*, 107(3), 155-162.
- Mardfekri, M., Gardoni, P., and Roeset, J. M. (2013). "Modeling Laterally Loaded Single Piles Accounting for Nonlinear Soil-Pile Interactions." *Journal of Engineering*, 2013.

- Moayed, R., Mehdipour, I., and Judi, A. (2012). "Undrained lateral behavior of short pile under combination of axial, lateral and moment loading in clayey soil." *kuwait journal of science and engineering*, 39, 59-78.
- Pan, W. D., Gu, R. G., Zhu, K., and Lv, Y. G. (2011). "Finite Element Analysis about the Properties of CFG-Pile Composite Foundation Based on Parametric Language PYTHON." *Advanced Materials Research*, 320, 20-25.
- Pando, M., Filz, G., Ealy, C., and Hoppe, E. (2003). "Axial and lateral load performance of two composite piles and one prestressed concrete pile." *Transportation Research Record: Journal of the Transportation Research Board*, 1849(-1), 61-70.
- Rajagopal, K., and Karthigeyan, S. (2011). "Influence of Combind Vertical and Lateral Loading on the Lateral Response of Piles."
- Sakr, M., and Hesham El Naggar, M. (2003). "Centrifuge modeling of tapered piles in sand." *ASTM geotechnical testing journal*, 26(1), 22-35.
- Sam, H. (2007). "Applied Soil Mechanics with ABAQUS Applications [Book].-[sl]". City: John Wiley & Sons, Inc.
- Sorochan, E., and Bykov, V. (1976). "Performance of groups of cast-in place piles subject to horizontal loading." *Soil Mechanics and Foundation Engineering*, 13(3), 157-161.
- Trochanis, A. M., Bielak, J., and Christiano, P. (1991). "Three-dimensional nonlinear study of piles." *Journal of geotechnical engineering*, 117(3), 429-447.
- Verruijt, A., and Van Baars, S. (2007). *Soil mechanics: VSSD*.
- Vipulanandan, C., Wong, D., Ochoa, M., and O'Neill, M. "Modelling of displacement piles in sand using a pressure chamber." *Presented at Foundation Engineering@ sCurrent Principles and Practices*.
- Yang, Z., and Jeremić, B. (2002). "Numerical analysis of pile behaviour under lateral loads in layered elastic-plastic soils." *International Journal for Numerical and Analytical Methods in Geomechanics*, 26(14), 1385-1406.
- Zhukov, N., and Balov, I. (1978). "Investigation of the effect of a vertical surcharge on horizontal displacements and resistance of pile columns to horizontal loads." *Soil Mechanics and Foundation Engineering*, 15(1), 16-22.

## Artificial Aging Time Effect on Fatigue stress for Friction Stir Welded AA6061T6

تأثير زمن التعتيق الصناعي على مقاومة الكلال لسبيكة المنيوم AA6061T6 لحمت بلحام الخلط الاحتكاكي

Ahmad Jasim Mohammad  
technical institute /Al swarah  
ahmedalmusawym@hotmail.com

### Abstract

This work involves studying the effect of heat treatment on the fatigue stress of friction stir welded joint of 6061T6 aluminum alloy. The microstructure , micro hardness , tensile and fatigue test of the welds and base alloy were examined before and after heat treatment which includes solution heat treatment at 500°C and artificial aging at 190°C for 2, 4, and 8hrs. The friction stir welding was carried out by using CNC milling machine at constant tool rotational speed of (1000 rpm) and welding speed of (20mm/min), the fatigue test is investigated for all specimens to obtain the S-N curve. The results show that the heat treatment decreased fatigue strength for all elements comparing with base metal, while ageing at 2 hrs gives the best fatigue strength due to participated phases.

**Key words:** Friction stir welding, 6061 Al-alloys, fatigue strength , solution heat treatment.

### الخلاصة

تضمن البحث دراسة تأثير المعاملات الحرارية على مقاومة الكلال لوصلات لحام الخلط الاحتكاكي لسبيكة المنيوم 6061-T6 تم فحص البنية المجهرية والصلادة المايكروية واختبار الشد والكلال للوصلات قبل وبعد المعاملة الحرارية التي تضمنت تسخين العينات الى درجة حراره 500°C ثم التبريد السريع بالماء ثم اجراء تعتيق صناعي حيث تم اعادة التسخين الى درجة 190°C لفرات زمنية 2,4,8 ساعة والتبريد بالهواء. انجز لحام الخلط الاحتكاكي على ماكينة التفريز المبرمجة باستخدام عدة تدور 1000 دورة بالدقيقة وسرعة لحام 20 m/min تم تطبيق اختبار الكلال على جميع العينات التي تم تصنيعها من وصلات لحام الخلط الاحتكاكي وفق المواصفة القياسية ASTM قبل وبعد المعاملة الحرارية للحصول على منحنى العمر (S-N) curve ومن النتائج التي تم الحصول عليها وجد ان المعاملات الحرارية تقلل من مقاومة الكلال للعينات الملحومة مقارنة بالمعدن الاساس وان افضل مقاومه للكلال كانت عند زمن تعتيق ٢ ساعه بسبب الاطوار المترسبه.

## **Introduction**

Aluminum alloys are widely used for high-strength and light mass structures in aerospace and automotive applications. Aluminum–magnesium–silicon (Al–Mg–Si) denoted as 6xxx series alloys are medium strength, heat treatable alloys, have good formability from simple to complex profiles by extrusion and corrosion resistance [1][2].

A great number of problems related to the welding of aluminum and its alloys occur because of the oxide layer, hydrogen solubility, electrical conductivity and thermal characteristics; they all result in crack sensitivity (both solidification and liquation cracking), porosity, and heat affected zone (HAZ) degradation. These problems can be eliminated by Friction stir welding (FSW) process. Friction Stir Welding (FSW) is a solid state joining technique using a tool with a probe attached to its tip rotated while being pushed against the butt sections of the pieces of metal to be welded. The frictional heat generated by this process softens the metal to produce a plastic flow that effectively stirs the metal from the sections on both sides and melting them together to create a weld Fig. (1)

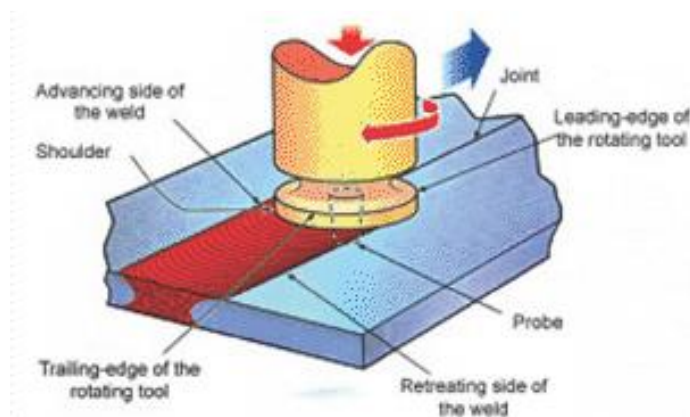


**Fig. 1** a Schematic of the FSW and tool geometry[4]

FSW is depend on the welding parameters such as pin rotation speed, travel speed and stirrer geometry. In order to increase the welding efficiency mechanical properties of joints must be maximized and the defects must be minimized in the friction stir welding (FSW) process [3][4]

The properties of various aluminum alloys can be altered by specific designated heat treatment. Some aluminum alloys can be solution treated to increase their strength and hardness. The heat treatment process can be classified into two processes; including solution heat treatment and artificial aging. This consists of heating the alloy to a temperature between 460<sup>0</sup>C and 530<sup>0</sup>C at which the alloying elements are in solution and water quenched then preheating to a temperature that investigate artificial ageing which generally carried out at temperatures up to approximately 200<sup>0</sup>C (for 6000 alloys between 160 <sup>0</sup>C and 200<sup>0</sup>C). Recently, some studies have been conducted on Friction Stir Welded joints after a heat

treatment to evaluate the stability of the fine grain structure at high temperature. One interesting details is the presence of Abnormal Grain Growth(AGG) in the nugget. The occurrence of this phenomenon may be a problem if it leads to a decay of mechanical properties of the weld [5].Therefore, studying the mechanical properties and related significant factors would be important [6] Although tensile test is the most popular type of material test, fatigue strength is very important from the viewpoint of strength design because most of the fracture of practical machine members is due to fatigue fracture fatigue is a problem that effected any structural component or part that moves. Automobiles on roads, airplanes principally the (wings) in air, ships on the high sea constantly battered by waves, nuclear reactors and turbines under cyclic temperature conditions, and many other components in motion are example in which the fatigue behavior of a material assumes a singular importance. It is estimated that 90% of service failure of metallic components that undergo movement of one form or another can be attributed to fatigue. If there is, in a mechanical component, a discontinuity such as a sudden change in cross section, a fillet, hole, groove, or notch, high localized stresses are induced at such places. Such discontinuities are called stress raisers and the localized stress effect produce stress concentration. Stress concentration must however considered if the component is subjected to fatigue loading [7]

Many researchers study the stir friction welding for AA6061 - T6 on mechanical properties, **Yoshiaki Yamamoto**[8] study the Fatigue Strength of Friction-Welded 6061 Aluminum Alloy Joints achieving that fatigue strength is decreased in friction stir welding method comparing with the base metal .

**J.D. Costa and J.A.M. Ferreira.** [9] studies the fatigue strength of friction stir welds and fusion inertly gas methods applied to AA6082-T6 under constant and variable amplitude loading and analyses the validity of Miner's rule for these specific welding conditions finding that FSW specimens present higher fatigue resistance than specimens welded by metal inert gas and tungsten inert gas processes. However, they still have lower fatigue lives than the base metal. Using the equivalent stress calculated by Miner's rule, a good agreement was observed between constant and variable fatigue loading results. The characteristic curve obtained for friction stir welds is higher than the International Institute of Welding (IIW) fatigue class for fusion welds with full-penetration both-sided butt joints.

**Benachour Mustapha** [10]studies the effect of the heat treatment or the state of material on the fatigue crack growth rate. The results show the influence of the heat treatment state on the shift of the fatigue life curves according to the propagated length.

The aim of this work is to investigate the effect of post-welding heat treatments on mechanical properties of butt FSW joints in6061T6 aluminum alloys.

**Experimental Work****Material Selected:**

The base metal used in this work was 12mm thick AA6061-T6 aluminum alloy plate, whose chemical composition is provided by using (Thermo ARL 3460, optical Emission spectrometer). The results, which is compared to the American standard, are summarized in Table (1)

**Table (1)** Chemical composition analysis of 6061 Al T6 – alloy [11]

Element wt%	Mg	Si	Fe	Mn	Cu	Cr	Zn	Al
Measured value	1.03	0.778	0.6	0.14	0.82	0.09	0.03	Rem
Slandered value	0.8- 1.2	0.4-0.8	Max 0.7	Max 0.15	0.15- 0.4	0.04- .35	Max 0.25	Rem

**Welding Process:**

As shown in Figure (2), the samples of 200mm\*70mm\*12mm were longitudinally butt welded using CNC milling machine (type Bridgeport). All similar welds of 6061-T6 aluminum alloy were performed using a welding tool made of tool steel .The welding tool is composed of shoulder of (20mm diameter) and probe of (10mm diameter and 11mm length). The welding tool is rotated at high speed and plunged into the joint line between two plates to be butt welded together. In this study, the welding parameters such as tool rotation speed of (1000 rpm) and travel or welding speed of (20mm/min) .



**Figure (2)** Friction stir welding process



**Categorizing of weld joint specimen**

After completing welding process, the joints categorized to groups as listed in **Table (2)**.

**Table (2)** Categorizing of weld joint specimen

Specimen symbol	state
A	As received
B	As welded
C	Solution heat treatment & artificial aging for 2h to weld joint
D	Solution heat treatment & artificial aging for 4h to weld joint
E	Solution heat treatment & artificial aging for 8h to weld joint

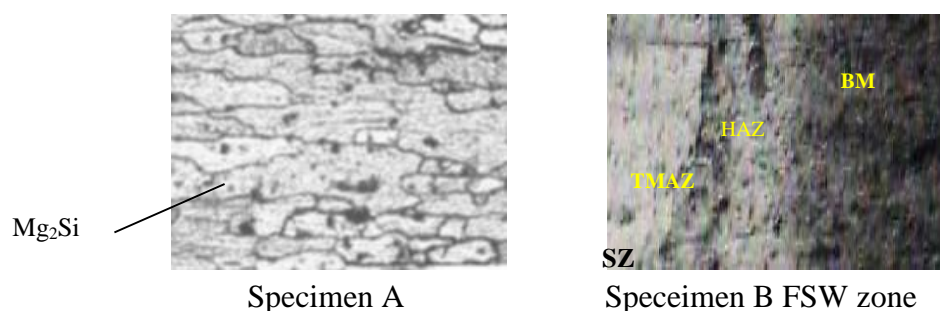
**Heat Treatment**

Precipitation heat treatment includes solution heat treatment and artificial aging were made for aluminum alloy AA6061-T6 welded joints in electric furnace at temperature of 500°C for 30min. Quenching in water then was followed by artificial aging process at 190°C for 2, 4, and 8hrs then cooled by air (ASTM Handbook,1991).

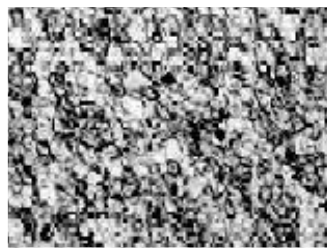
**Examination and tests****1-Microstructure test**

Samples made from a cross section of the FSW joints and base alloy were prepared including: ground, polished and etched and observed under optical microscope in sequences steps. Wet grinding operation with water was done by using emery paper of SiC with the different grits of (220,320,500, and 1000). Polishing process was done to the samples by using diamond paste of size (1µm) with special polishing cloth and lubricant. They were cleaned with water and alcohol and dried with hot air. Etching process was done to the samples by using etching solution (Keller's reagent) consisting of 95 ml distill water, 2.5 ml HNO<sub>3</sub>, 1.5 ml HCl and 1 ml HF washed after that with water and alcohol and dried in oven.

The friction stir welded joint samples were examined by Nikon ME-600 optical microscope provided with a NIKON camera, DXM-1200F. the microstructure results are shown in **Fig. (3)**







Specimen C in stir zone



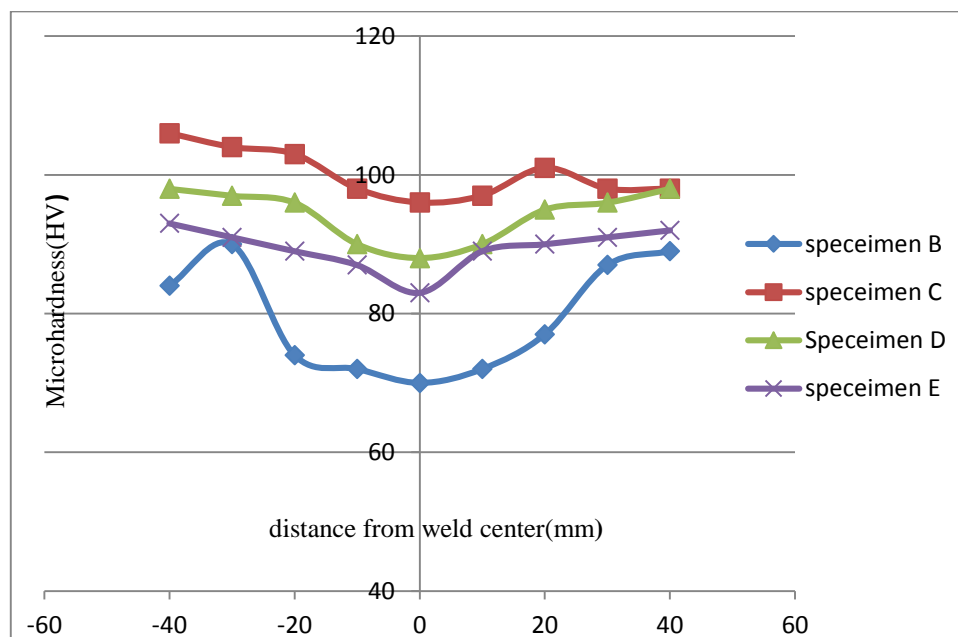
Specimen D in stir zone



Specimen E in stir zone

**Fig (3)** the microstructure of all specimens in Table(2) at (40X)**Mechanical properties****2- Hardness test**

The Vickers hardness instrument with a 300gf load was used for hardness profile across the friction stir weld joint where the results are shown in **Fig. (4)**.

**Fig. (4):** The VickersHardness profiles of a transverse cross section welds zone

### 3- Tensile test

Tensile test was implemented for specimens prepared in the dimensions which is shown in **fig.(5)** according to ASTM176000 by using Testing machine smart series with preload value (N) 100 and cross head speed (mm/min) or rate. 20. Extension or position measured by XHD \_ 100(XHD 100) for all specimens in **table (2)**, the obtained results are listed in table (4).

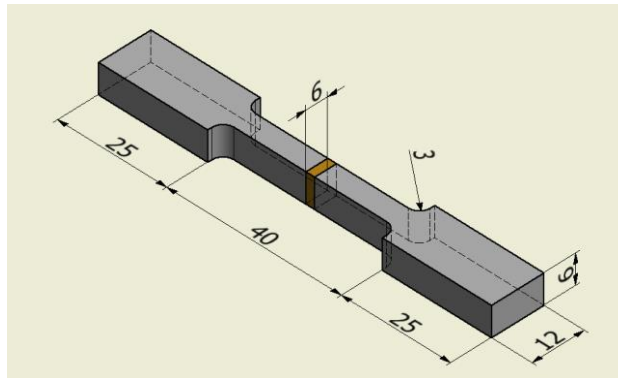


**Fig. (5)** Tensile test specimen dimensions (all dimensions in mm)

**Table (3)** Stander mechanical properties of 6061T6 [12]

Material	Yield strength MPa.	Ultimate tensile strength ( UTS) MPa.	Percentage of elongation %
6061-T6	295	342	10

**Table (4)** results of mechanical properties

Sample	$\sigma_u$ N/mm <sup>2</sup>	Yield stress $\sigma_y$ N/mm <sup>2</sup>	Elongation %	Hardness Hv(kg/mm <sup>2</sup> )
A	344	302	9	102
B	181	151	6	70
C	218	180	10	96
D	177	115	10	88
E	81	40	2	82

### 5-Surface roughness

The average value of the free surface roughness, which was measured at the surface area of all specimens in table(2) indicated by the parameter Ra which is the center-line average of adjacent peaks results are listed in Table (5)

**Table (5)** the results of Surface roughness

Specimen Symbol	A	B	C	D	E
Surface roughness Ra ( $\mu$ m)	0.18	0.13	0.09	0.12	0.095

**Rotating Bending Testing**

To get perfect dimensions of the specimens and to avoid mistakes, an accurate profile should be attained. All specimens were machined using programmable CNC machine. During manufacturing of the specimens, careful control was taken into consideration to produce a good surface finish and to minimize residual stresses. The test specimens are shown schematically in Figure (6).

A rotating bending fatigue – testing machine was used to execute all fatigue tests, The specimen was subjected to an applied load from the right side of the perpendicular to the axis of specimen, developing a bending moment. Therefore, the surface of the specimen is under tension and compression stresses when it rotates.

The bending stress ( $\sigma_b$ ) is calculated using the relation:

$$\sigma_b = \frac{p \cdot L \cdot 32}{\pi \cdot d^3} \quad (1)$$

where P is the load measured in Newton (N), and (L) the force arm is equal to 125.7 mm and (d) is the minimum diameter of the specimen in mm. The Test machine is Avery 7305 type and Fig.(7) shows the fatigue behavior of all specimens aluminum alloys 6061T6

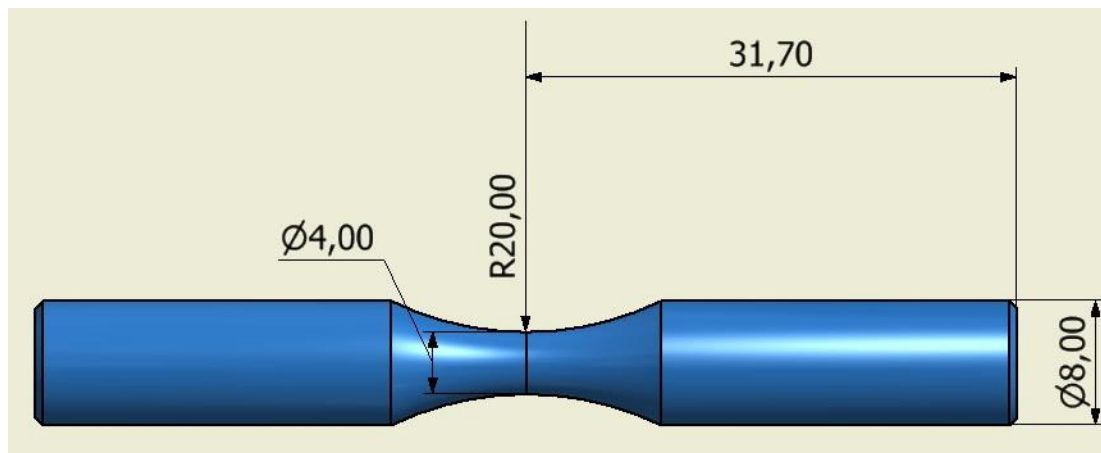


**Fig. (6)** Fatigue test specimen in mm

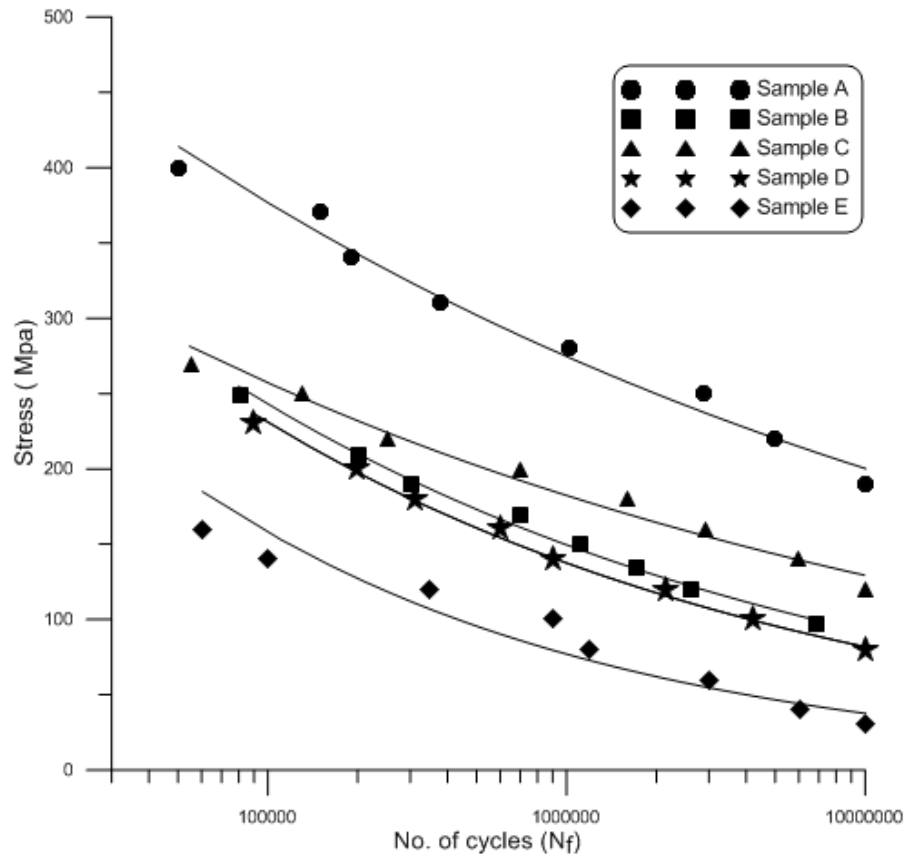


**Figure (7)** S-N curve of all specimens alloy 6061T6

The behavior may be described by the S-N curve equations as follows for all specimens

Specimen A	$\sigma_f = 1749 Nf^{-0,13}$
Specimen B	$\sigma_f = 2287 Nf^{-0,2}$
Specimen C	$\sigma_f = 1356 Nf^{-0,14}$
Specimen D	$\sigma_f = 2946 Nf^{-0,22}$
Specimen E	$\sigma_f = 4467 Nf^{-0,29}$

### Discussion

In **Fig.(3)** specimen(A) shows the microstructure of base metal aluminum alloy 6061T6 contains coarse and elongated grains with uniformly distributed very fine precipitates. Found that the higher strength of the base metal was mainly attributed to the presence of alloying elements such as silicon and magnesium. These two elements combined together and underwent precipitation reaction and form a strengthening precipitate of  $Mg_2Si$ . As the result, the fine and uniform distribution of these precipitates throughout the aluminum matrix provides higher strength to these alloys [13]. While a comparison between the base metal and fraction stir zone indicating by FSW we can see in sample (B) During FSW process, the material undergoes intense plastic deformation at

elevated temperature, resulting in generation of fine and equiaxed recrystallized grains . At the same time, after severe plastic deformation a fine, equiaxed grains due to the temperature difference between the tool shoulder side and base size and the tool centerline and the edge of the weld nugget which causes the grain size variations, this can be attributed to the mechanical forces operative during welding which causes both refinement and re – alignment of the matrix grains and should be beneficial with respect to various mechanical properties [14]

It also can be observed from **Fig.(3)** that variation in grain size of the alloy (6061-T6) depend mainly on the proportion of the silicon and magnesium elements in the alloy and the presence of the other alloying elements causing the forming of different soluble or insoluble compounds in solid state [15] . And also It had been observed that the aging time would have sufficient time to occur. The kinetics of phase precipitations are usually affected by the variations in aging time and heating temperature, this behavior can be attributed to the difference in microstructure of the specimens (C,D,E) [16]. The variations in the hardness measured across the welded specimens from the weld center towards the base metal are shown in fig. (4). In FSW processes specimen (B) the over aging and dissolving of the metastable precipitates lead to the decrease in the micro hardness in the weld zone of friction stir welding of Al 6061-T6 (70Hv) and generate a region of relatively low hardness value (78 Hv) around weld center. This zone extends up to the transition of TMAZ and HAZ. This is due to coarsening/ dissolution of strengthening precipitates ( $Mg_2Si$ ). Maximum hardness occurs in TMAZ because aging strengthens the welds [17]. Hardness a gain increases toward the base metal (100Hv). Because there is a difference in plastic deformation between advancing and retreating sides, a significant difference is produced in precipitate microstructure, as well as the difference in thermal cycles on both sides, unsymmetrical micro hardness profile can be pointed out and when we compare this result with sample (C,D,E) In table (4) we see the specimen group (C) gives the high result compared with the specimens group (B, D,E) which gives the least value and the base metal exhibits the best mechanical properties and the well-defined proportional limit. A reduction of tensile properties to weld metal specimen found in a percentage of 47% (specimen B) comparing with base metal while specimen (C) obtained a 36 % reduction of the strength with respect to the base metal and specimens D,C gives the highest reduction due to over-aging, when welding a 6061-T6 alloy is a fairly well-understood phenomenon and it is explained in terms of the precipitation sequence undergone by this alloy with temperature [9].

The experimental of fatigue tests have allowed recording the life of specimens of 6061-T6 alloys welded by friction stir welding and base metal at different loading conditions.

Fatigue life was calculated based on the average of five values, as presented in Fig (7). Theoretical analyses and experimental evidence reveal that the fatigue crack was initiated in the HAZ and then propagate into the weld metal to finally cause the failure. During the tests FSW welded specimens have been failed exactly in HAZ. [10]. The deformation and yielding are concentrated in the weld metal region in the case of lower strength for all weld specimens(B,C,D,E) compared with base alloy. The results of fatigue tests, which report compared fatigue strength of welded and parent metal (fig. 7), show rather reduced values of fatigue resistance for welded specimens. It is interesting to notice that, in spite of the fact that tensile tests generally gave rise to a fracture in the HAZ, all the welded fatigue specimens fractured in the stir zone, starting from outer surface.

### **Conclusion**

- 1- Grain refinement in weld metal has been achieved due to frictional heating and plastic flow.
- 2- In FSW operation, hardness of weld zone is low comparing with base alloy because of the plastic deformation and cooling rate.
- 3-Tensile strength of welded joints of 6061-T6 Al alloy, undergo a remarkable reduction of the initial value.
- 4-Fracture in tensile tests is located in the HAZ; on the contrary, fatigue test specimens fractured in the welded metal in all cases. Fatigue fracture in the welded specimens occurred earlier than in the un welded specimens, due to the presence of some porosity.
- 5- 2 hrs of artificial ageing improved fatigue strength for the weld joint due to precipitated ages ,on contrary 4 and 8 hrs decreased the strength because of grain growth

### **References**

- [1]Mostafa mansourinejad<sup>1</sup>, BAHMAN mirzakhani<sup>2</sup> Influence of sequence of cold working and aging treatment on mechanical behaviour of 6061 aluminum alloy Trans. Nonferrous Met. Soc. China 22(2012) 2072–2079.
- [2]F.F. Curiel, R. Garc´ia, and V.H. L´opez An alternative to increase the mechanical strength of 6061-T6 GMA weldments revistamexicana de f´ısica s **55** (1) 39–43 mayo 2009
- [3] M.A. Sutton , B. Yang, A.P. Reynolds, R. Taylor, " Microstructural Studies of Friction Stir Welds in 2024-T3 Aluminum", Materials Science and Engineering, Vol. A323, p160–166, 2002.
- [4]-S. RAJAKUMAR, C. MURALIDHARAN, V. BALASUBRAMANIAN.'’ empirical relationships to predict grain size and tensile strength of friction stir welded AA 6061-T6 aluminum alloy joints’’, transactions of nonferrous Metals Society China. 20, pp.1863-1872, 2010
- [5] I. Charit, R.S. Mishra. Abnormal Grain Growth in Friction Stir Processed Alloys. ScriptaMaterialia 58 (2008) 367–371

- [6] Hsing-Ta Hsieh<sup>1</sup> and Jahau Lewis Chen, "Influence of Welding Parameters on Mechanical Properties of Friction Stir Welded 6061-T6", *Materials Transactions*, Vol. 49, No. 10, pp. 2179 to 2184, (2008)
- [7] M.A. Meyers and K.K.Chawla, "Mechanical behavior of material", Prentice-Hall Inc,-3 USA, 1999
- [8] Yoshiaki Yamamoto<sup>1</sup>, Hiizu Ochi<sup>2</sup>, Takeshi Sawai<sup>3</sup>, Hiroshi Yamaguchi<sup>4</sup> and Koichi Ogawa, "Fatigue Strength of Friction-Welded 6061 Aluminum Alloy Joints", *Materials Transactions*, Vol. 48, No. 11 (2007) pp. 2909 to 2913
- [9] J.D. Costa and J.A.M. Ferreira, Influence of spectrum loading on fatigue resistance of AA6082 friction stir welds, *International Journal of Structural Integrity*, Vol. 2 Iss: 2 pp. 122 – 134
- [10] benachourmustapha\*, hadjouiabdelhamid\*, benguediabmohamed, "heat treatment effect on fatigue crack growth", 3rd international conference on integrity, reliability and failure, porto/Portugal, 20-24 July 2009
- [11]- *Metals Handbook*, Vol.2 - Properties and Selection: Nonferrous Alloys and Special-Purpose Materials, ASM International 10th Ed. 1990.
- [12] Nazar Abdulwadood<sup>1</sup>, Burak Sahin<sup>1</sup>, Nihat Yildirim "effect of welding parameters on the mechanical properties of dissimilar aluminum alloys 2024-t3 to 6061-t6 joints produced by friction stir welding" *Niğde Üniversitesi Mühendislik Bilimleri Dergisi*, Cilt 3, Sayı 1, (2014), pp.25-36
- [13]. T Senthil Kumar, V Balasubramanian, M Y Sanavullah, "Influences of pulsed current tungsten inert gas welding parameters on the tensile properties of AA 6061 aluminum alloy", *Materials and Design* 28 (2007) 2080-2092
- [14]- Bradley G.R. and James M.N., "Geometry and Microstructure of Metal Inert Gas and friction Stir Welded Aluminum Alloy 5383-h321", [www.plymouth.ac.uk](http://www.plymouth.ac.uk) October 2000.
- [15] K. Srinivasa Ro. "Pitting Corrosion of heat treble Aluminum alloys and Weld" *Trans. India in St. Md*, vol. 57 No. 6 pp(503-610) December 2004
- [16] Hilil Demir, Suleyman Gunduz, "The effect of aging on machinability of 6061 aluminum alloy", karabuk University Turkey Elsevier Ltd *Materials and design journal* 2008.
- [17] Prince Sainia\*, S.P.Tayala Experimental Study of Hardness by Friction Stir Welding of 6061-T6 Aluminium Pieces *International Journal of Current Engineering and Technology* ISSN 2277 – 4106 - 2013

## Effectiveness of film cooling process on flat plate using multi-rows of cooling

Assist. Prof. Dr. Ahmed K. Al Shara  
University of Misan  
Petroleum Engineering Dept.

Dr. Hussien S. Sultan  
University of Basrah  
College of Engineering

BSc. Haitham M. Bachi  
University of Basrah  
College of Engineering

### Abstract:

Film cooling process is one of the most important external cooling methods used for gas turbine blades. In the present study the effectiveness of multi – row film cooling process on flat plate was estimated. Three rows of film cooling were considered with three configurations which are: simple injection angle with uniform cooling holes distribution, compound injection angle with uniform cooling holes distribution and staggered distribution for film cooling holes with simple injection angle. The simulation of the three cases were performed for different Reynolds number under real operating conditions. Gambit – Fluent package was used for the numerical simulation. Three dimensional incompressible turbulent flow with  $k - \epsilon$  model for turbulence was used for the simulation. The results show that, the staggered distribution for the film cooling holes gives the best for effectiveness the cooled surface.

### فعالية عملية التبريد الغشائي على صفيحة مستوية باستخدام صفوف تبريد متعددة

#### الملخص:

تعد عملية التبريد الغشائي واحدة من اهم عمليات التبريد الخارجي المستخدمة في ريش التوربين الغازي. تم في هذه الدراسة تحديد فعالية عملية تبريد غشائي لصفيحة مستوية. استخدمت ثلاثة صفوف تبريد مرتبة بثلاث طرق هي: زاوية حقن بسيطة مع توزيع منتظم لثقوب التبريد، زاوية حقن مركبة مع توزيع منتظم لثقوب التبريد وتوزيع متخالف لثقوب التبريد مع زاوية حقن بسيطة. تم التمثيل النظري لهذه الطرق الثلاث باستخدام قيم مختلفة لرقم رينولدز تحت ظروف تشغيل حقيقية. تم الحل العددي لهذه الحالات الثلاث باستخدام الحقيبة البرمجية فلونت. التمثيل العددي تم بفرض جريان ثلاثي البعد، لا انضغاطي ومضطرب مع استخدام الموديل الرياضي  $k - \epsilon$  لنموذج الاضطراب. بينت النتائج ان فعالية التبريد الافضل كانت لحالة التوزيع المتخالف لثقوب التبريد.



## 1-Introduction:

A great improvement in gas turbine efficiency in the recent was resulted from the increased of the temperature of the gases inlet to the turbine. This increase in the turbine inlet temperature results from the efficient cooling of gas turbine blades. So, the turbine inlet temperature increased to the range of (2000 K)[1]. External cooling of gas turbine blades by using film cooling process, represents one of the most efficient cooling techniques. Simulation of film cooling process was important for improving the effectiveness of the process, and as a result the gas turbine efficiency.

Different theoretical studies were performed for the simulation of the film cooling process on flat plate. Some of these studies are for single hole film cooling process [2,3,4,5], single row with multi holes [6,7,8] and multi rows with multi holes [9,10,11,12]. Most of these studies were performed under operating conditions far from the real operating conditions of gas turbine. Also, most of these studies were focused on single parameter which effects the effectiveness of the process, such as injection angle and holes distribution.

In the present study, the simulation is performed under real operating conditions and also, the effect of different parameters (simple injection angle ,compound injection angle and holes distribution) on the film cooling effectiveness are considered.

## 2- Mathematical formulation:

### 2-1 Geometry:

The geometry for the three cases are performed and all dimensions were explain as shown in the (Figure 1). starts from drawing of the geometry of three cases, where the dimensions of main stream channel are:( $z=20\text{mm}$ ,  $x=80\text{mm}$ ,  $y=10\text{mm}$ ) and the dimension of cooling chamber are: ( $z=20\text{mm}$ ,  $x=34\text{mm}$ ,  $y=6\text{mm}$  ). The nozzles (holes) is inclined with angle  $\alpha$ , and the diameter of the hole is  $d$ , the distance between any hole and the vicinity one is  $d$ . For all cases, the diameter of the cylindrical cooling hole is  $d=2\text{mm}$  with an inclination angle of  $\alpha=20^\circ$ , and the ratio of the length of the cooling hole to the diameter is 5.8. The configurations of the holes are :

1-Simple injection angle.

2-Staggered simple injection angle.

3-Compound injection angle.

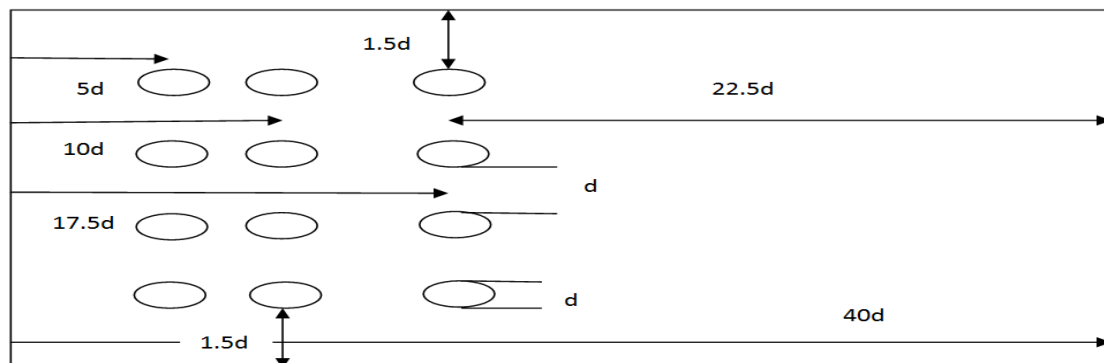


Figure 1 Simple injection angle configuration

## 2-2 Governing equations:

### 2-2-1 Conservation of Mass:

$$\frac{\partial}{\partial x_i} (\rho u_i) = 0 \quad (1)$$

### 2-2-2 Conservation of Momentum:

$$\frac{\partial}{\partial x_i} (\rho u_i u_j) = -\frac{\partial P}{\partial x_i} + \frac{\partial}{\partial x_j} \left[ \mu \left( \frac{\partial u_i}{\partial x_j} + \frac{\partial u_j}{\partial x_i} \right) - \rho \overline{u_i u_j} \right] + F_i \quad (2)$$

### 2-2-3 Conservation of Energy:

$$\frac{\partial}{\partial x_i} (c_p \rho u_i T) = \frac{\partial}{\partial x_j} \left[ k \frac{\partial T}{\partial x_j} - \rho \overline{u_j T} \right] \quad (3)$$

### 2-2-4 Cooling Effectiveness: ( $\eta$ )

$$\eta = \frac{T_{h,in} - T_f}{T_{h,in} - T_{c,in}} \quad (4)$$

## 2-3 Grid dependency analysis:

For all previous cases three dimensional numerical simulation with turbulent flow are performed by using the CFD code "FLUENT" which based on finite volume approach to solve the partial differential equation (mass, momentum and energy). The first step of the simulation process is to establish the mesh size, so that the results obtained are grid independent. In the present study the numerical simulation model for the simple injection case are checked with different mesh sizes. The comparison between all the mesh sizes are based on the average surface temperature in the spanwise direction for different location in the stream wise direction which are (X=40 and 80mm) as shown in the Fig.4. From the figure, the minimum percentage error of the predicted temperature lies between the mesh volume of (1150000) and the mesh volume (1300000). The percentage error between the two meshes for the three given locations is (0.09%) for (X=40mm) and error (0.2%) for (X=80mm). So the mesh size of (1150000) is used in the simulation in order to reduce the calculation time.

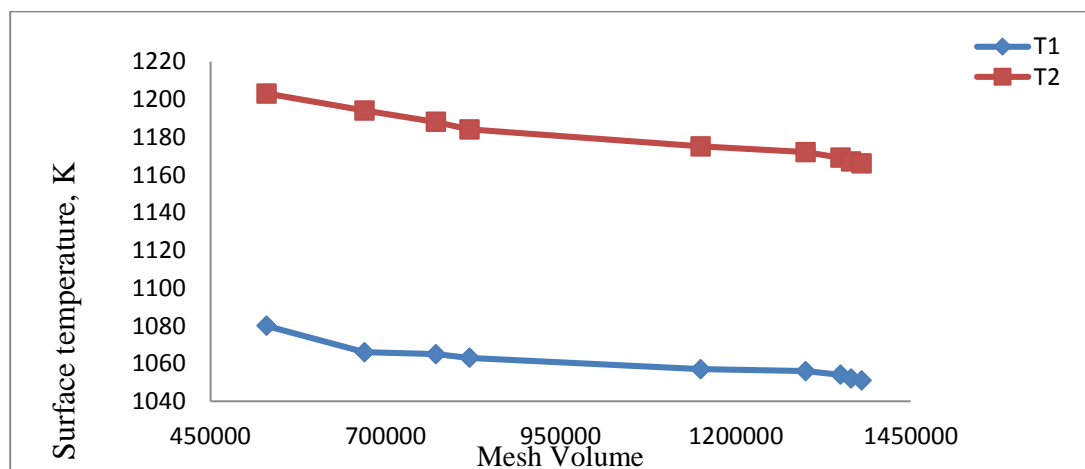


Fig.2. Grid independence for simple injection angle, B.R=0.5, Re=10000,  $\alpha=20^\circ$

**Model validation:**

Apreliminary investigation has been done to validate the present model with the results of Chenga et al.[2] The case study of Chenga was the simulation of film cooling process over a flat plate with single hole and simple injection angle. Different blowing ratio were used (0.5, 1, 1.5, 2) and compared between the film cooling effectiveness in stream wise direction, which is on flat plate cooling with single cylindrical hole. The hole diameter is  $d=12.7\text{mm}$  with an inclination angle  $\alpha=30^\circ$ , length to diameter ratio is 4, the main stream speed and temperature is 20 m/s and 300K respectively. Coolant temperature is 150K, with main stream turbulence intensity is 2%. The results of the film cooling effectiveness of the present simulation are compared with those obtained by Chenga. The comparison is shown in Figure.5. There is a good agreement with the Chenga results.[2]

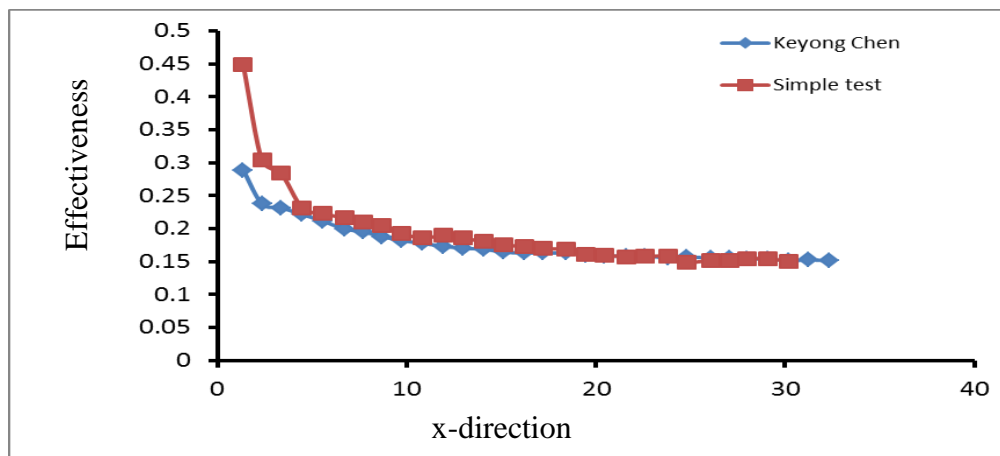


Fig.3. The validation of the present work with Chenga[2]

**3- Boundary conditions:****3.1 Boundary condition for inlet main stream(hot gases):**

- 1-The main stream temperature  $T=T_{in,h}=1500\text{K}$ .
- 2-Turbulence intensity is 5%.
- 3-The velocity  $U=U_{in,h}=31, 62, 124, 248$  and  $310\text{m/s}$ . Each value corresponds to a certain value of Reynolds number. ( for  $Re=10000, 20000, 40000, 80000$  and  $100000$  respectively).

**3.2 Boundary condition for inlet cooling stream:**

- 1-The inlet cooling temperature  $T=T_{in,c}=600\text{K}$ .
- 2-Turbulence intensity is 5%.
- 3-The velocity  $U=U_{in,c}=(7.299, 14.601, 29.1996, 58.464$  and  $73.08\text{ m/s})$ .

**3.3 Outlet boundary conditions:**

- 1- Outlet pressure is 5 bar.

### 3.4 Walls boundary conditions:

1- No-slip condition.

2- The walls are:

A- The bottom surface of main channel at constant temperature  $T = 1000\text{K}$ .

B- Other walls are insulated.

### 4- Results and discussion:

#### 4-1 Stream wise effectiveness:

The countours of film cooling effectiveness along the cooled flat plate surface at  $B.R=1.5$ ,  $\alpha=20^\circ$ , Reynolds number equal to 10000 & 100000. are given in Figures. (4 to 9), the red regions, represents the maximum effectiveness when the surface covered by the cooling air only and this value decrease when the mixing with hot gases increase and this decreasing is represented by the yellow, green and white blue regions. The dark blue regions, represents the regions subjected to the hot gases only. Also, for all cases the lateral spread of the film cooling layer decreases with increasing of Reynolds number due to decreasing the penetration of the cooling air through the hot gases, while the axial spread is increased.

The average effectiveness along a line in the stream wise direction located at ( $z=10\text{mm}$ ) is given in table 1. From the table its clear that the staggered distrebuton gives the best effectiveness due to the good coverage of the cooling air along the cooled surface.

Table 1. Average streamwise effectiveness at(  $Z=10\text{mm}$ ) at different Reynolds number.

Re	Eff.(Simple)	Eff.(Staggered)	Eff.(Compound)
10000	0.341	0.621	0.550
20000	0.3233	0.625	0.550
40000	0.313	0.628	0.5499
80000	0.305	0.629	0.5497
100000	0.303	0.630	0.5490

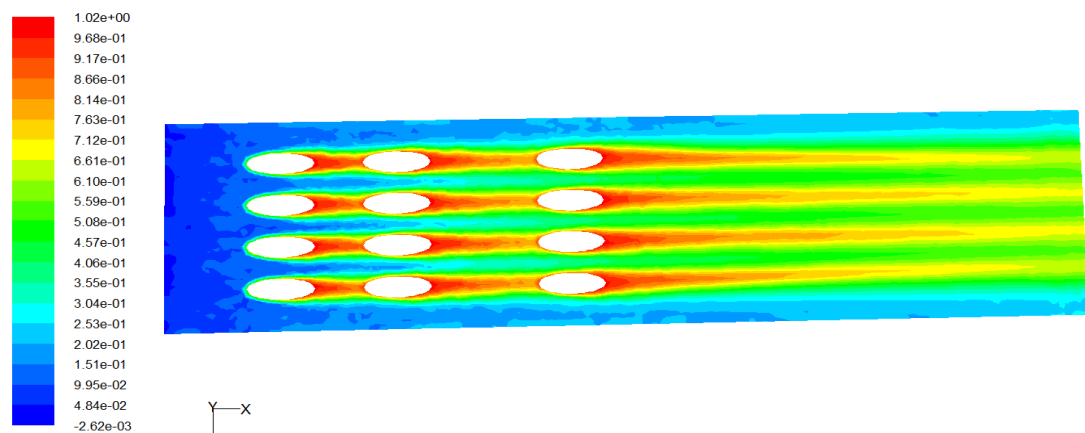


Fig.4 Contours of effectiveness at flat plate surface with simple injection angle,  $B.R=1.5$ ,  $\alpha=20^\circ$  and  $Re=10000$

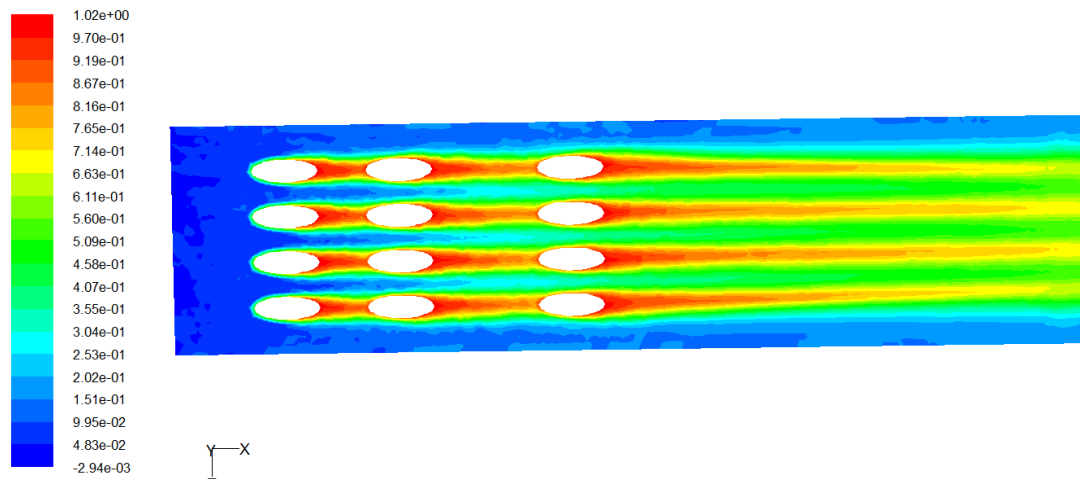


Fig.5 Contours of effectiveness at flat plate surface with simple injection angle, (B.R=1.5,  $\alpha=20^\circ$  and Re=100000)

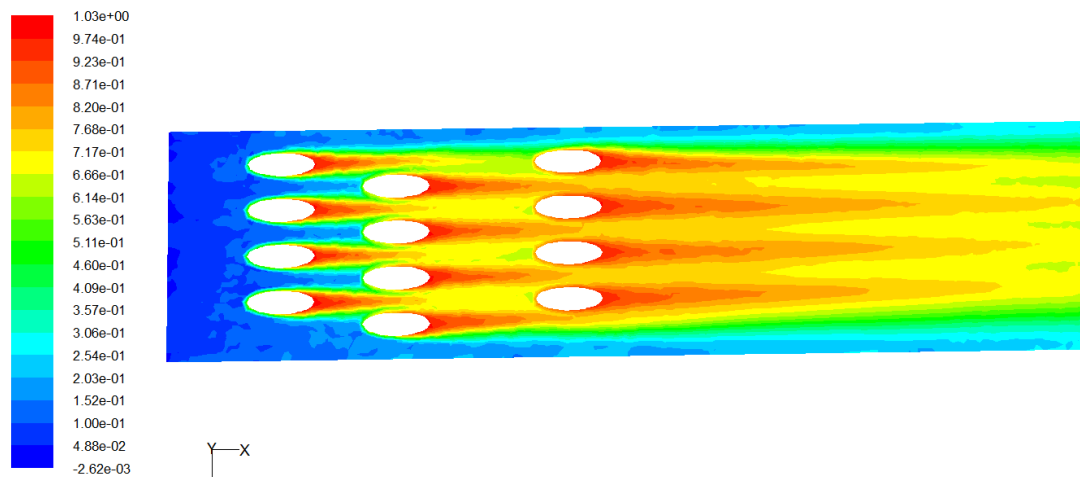


Fig. 6 Contours of effectiveness at flat plate surface with staggered simple injection angle, (B.R=1.5,  $\alpha=20^\circ$  and Re=10000)

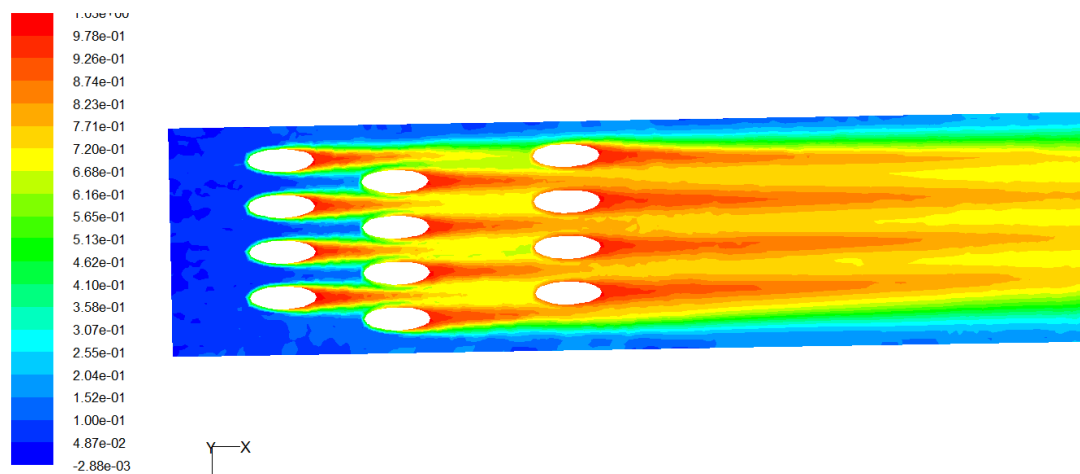


Fig. 7 Contours of effectiveness at flat plate surface with staggered simple injection angle, (B.R=1.5,  $\alpha=20^\circ$  and Re=100000)

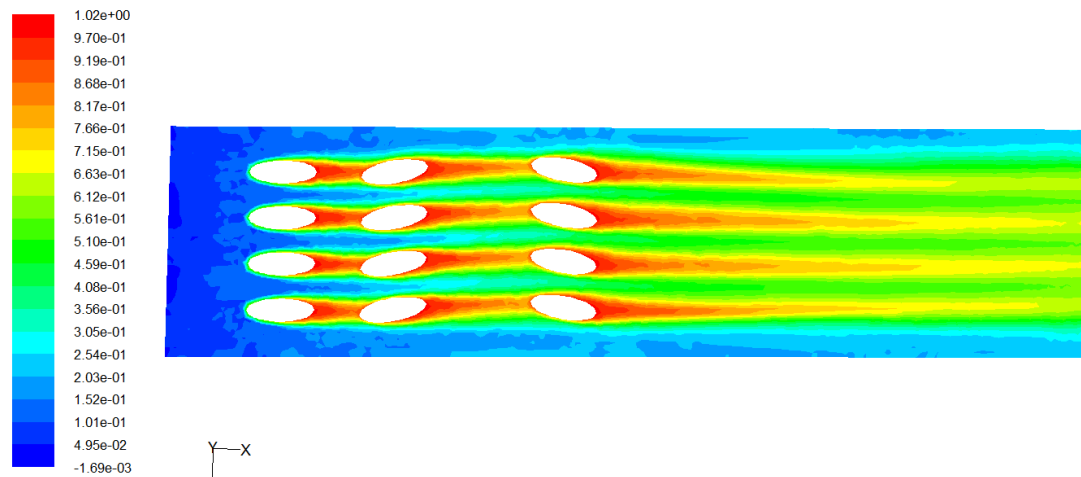


Fig. 8 Contours of effectiveness at flat plate surface with compound injection angle, ( $B.R=1.5$ ,  $\alpha=20^\circ$ ,  $\beta=10^\circ$  and  $Re=10000$ )

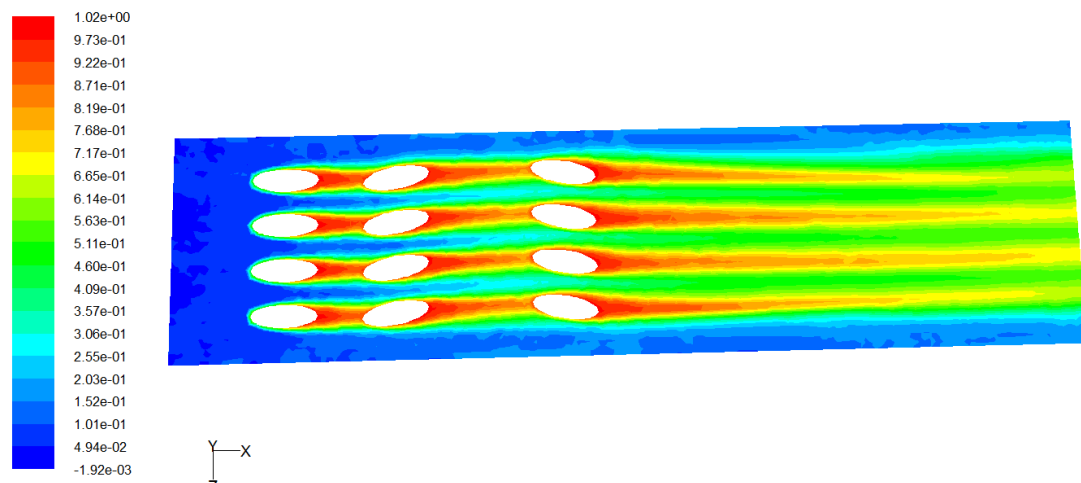


Fig. 9 Contours of effectiveness at flat plate surface with compound injection angle, ( $B.R=1.5$ ,  $\alpha=20^\circ$ ,  $\beta=10^\circ$  and  $Re=100000$ )

#### 4-2 Span wise effectiveness:

The variation of film cooling effectiveness in the span wise direction at different locations with stream wise direction at  $B.R=1.5$ ,  $\alpha=20^\circ$ , Reynolds number 10000 & 100000 are given in the Figs. (10 to 15), where simple case Figs (10 & 11), staggered case Figs. (12 & 13) and compound case Figs. (14 & 15). The variation of the film cooling effectiveness is given at the locations ( $X=15, 25, 40, 60$  and  $80\text{mm}$ ). Also, the maximum values of effectiveness at the film cooling holes, and beyond the holes there is decrease in the values of film cooling effectiveness due to the mixing of the two streams. The staggered case predicts the optimum values of the film cooling effectiveness along the cooled and protection flat plate surface due to the distribution of the cooling holes. There is accumulated effect between the successive rows results in good spread of the film cooling layer.

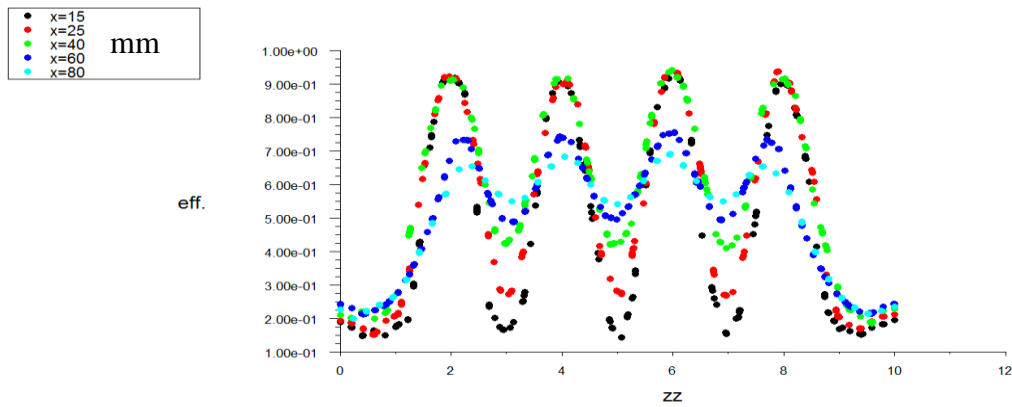


Fig. 10 Effectiveness for simple injection angle, (B.R=1.5,  $\alpha=20^\circ$  and Re=10000)

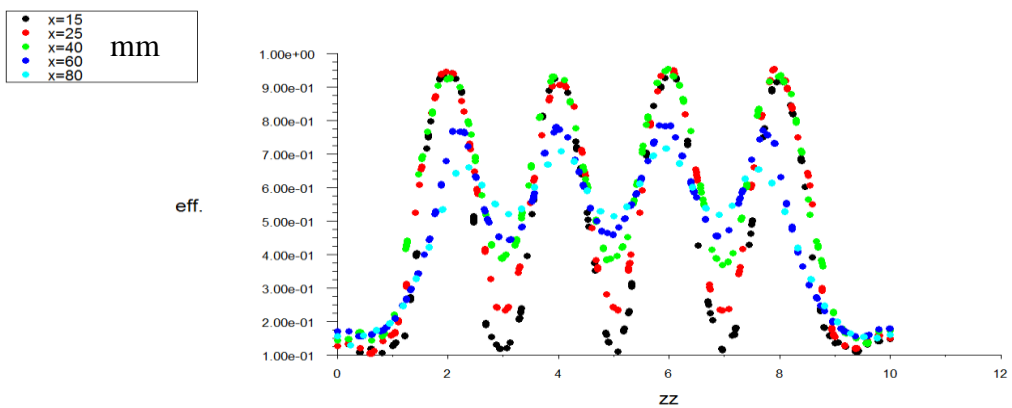


Fig. 11. Effectiveness for simple injection angle, (B.R=1.5,  $\alpha=20^\circ$  and Re=100000)

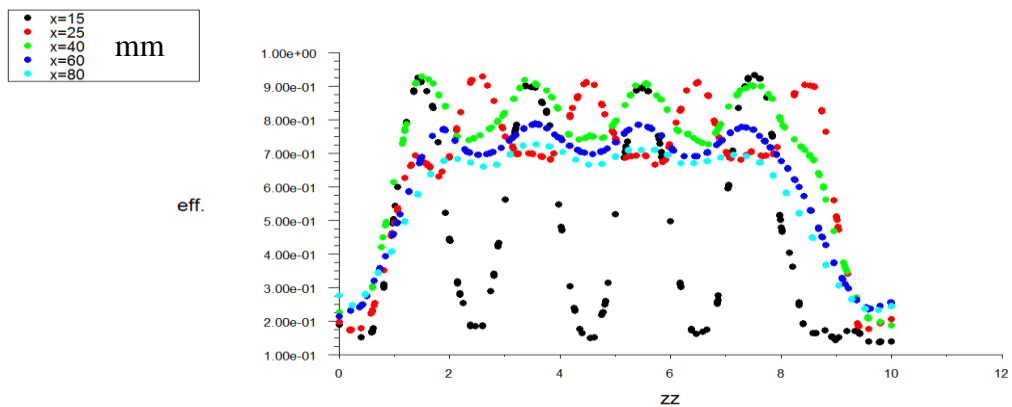


Fig. 12. Effectiveness for staggered simple injection angle, (B.R=1.5,  $\alpha=20^\circ$  and Re=10000)



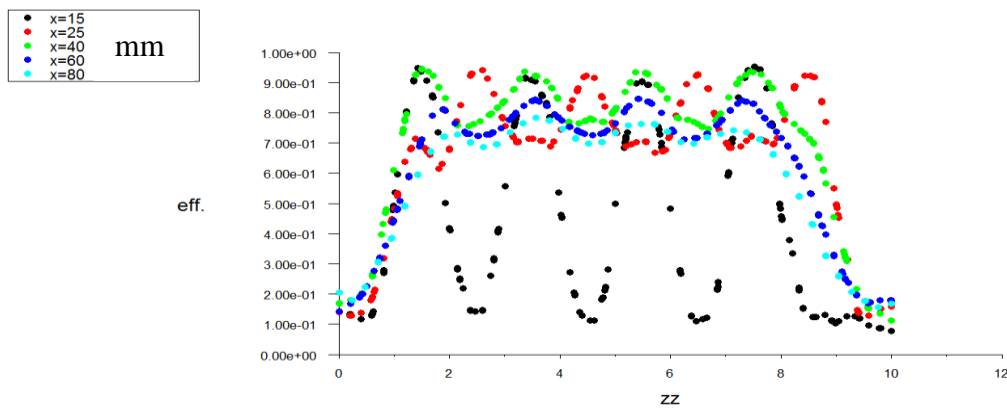


Fig. 13. Effectiveness for staggered simple injection angle, (B.R=1.5,  $\alpha=20^\circ$  and  $Re=100000$ )

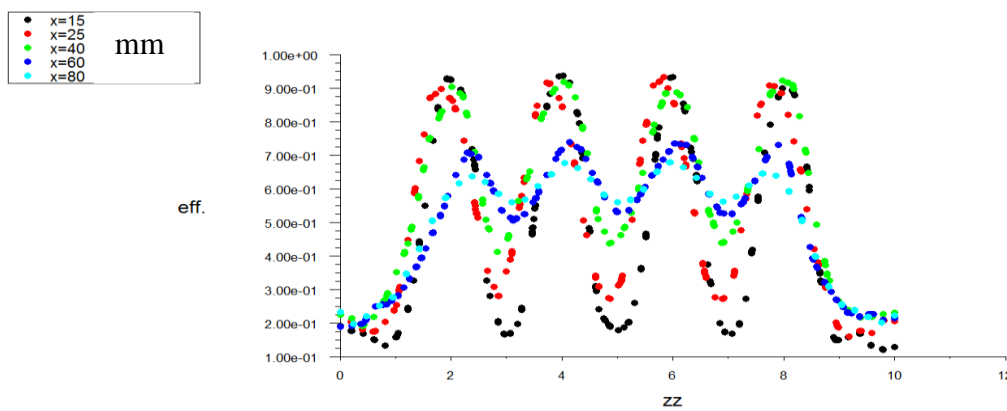


Fig. 14. Effectiveness for compound injection angle, (B.R=1.5,  $\alpha=20^\circ$ ,  $\beta=10^\circ$   $Re=10000$ )

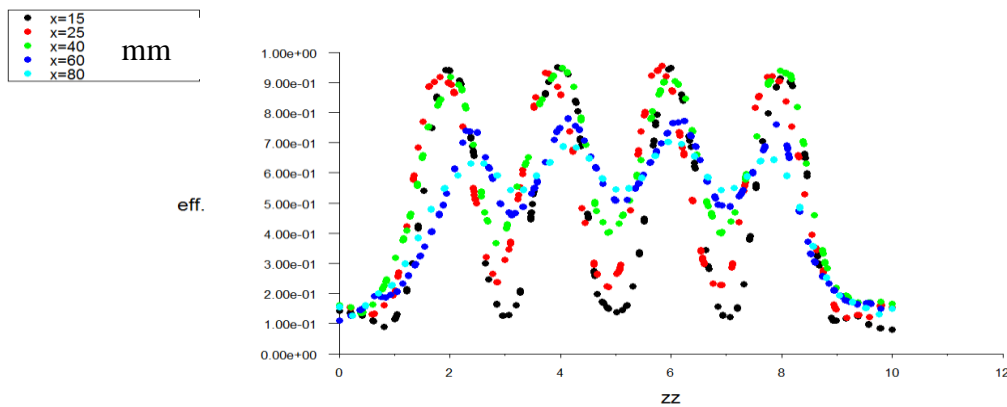


Fig. 15. Effectiveness for compound injection angle, (B.R=1.5,  $\alpha=20^\circ$ ,  $\beta=10^\circ$  and  $Re=100000$ )

## 5- Conclusions:

The film cooling flow over flat plate at constant temperature is investigated using numerical method (Finite Volume Method) with software package (Fluent). It is found that the main parameter that effect on the performance are Reynolds number, blowing ratio and holes configuration where three holes configurations (Simple distribution, Staggered distribution and Compound distribution) are studied. It can be concluded that from the present study:-

- 1- The staggered injection gives maximum effectiveness.
- 2- Increment of Reynolds number leads to decrease the effectiveness, except the staggered case.

## Nomenclature:

$\rho$ : Fluid density ( kg/m<sup>3</sup>)

$C_p$ : Specific heat at constant pressure( J/kg. k)

P: Pressure (Pa)

$F_i$ :External forces per unit area in the x, y , z direction (N/m<sup>2</sup>)

d: Hole diameter (m)

k: Thermal conductivity (W/m .K)

$\mu_t$ : Turbulent viscosity (N.s/m<sup>2</sup>)

U: Steady mean velocities in the x direction ( m/s)

T: temperature(K)

$T_{inh}$ : Hot stream inlet temperature (K)

$T_{inc}$ : Cold stream inlet temperature (K)

$T_f$ : Adiabatic Wall Temperature(K)

$Tu$ : Turbulent intensity

A: Inclination angle( degree)

$\beta$ : Orientation angle( degree)

k- $\epsilon$ : turbulent model

## References:

- 1- Suhaila Binti Mat Said " Modeling Study of Gas Turbine Burner Cooling Ring Efficiency in a Model Combustor Exit Duct " University Technical Malaysia Melaka, (2010).
- 2- Rajesh K. Gupta" Computational Investigation of Gas Turbine Blade Cooling" University Roll No. 10235, (2006).
- 3- Tobias Pihlstrand " Investigation of Converging Slot-Hole Geometry for Film Cooling of Gas Turbine Blades" Project Report Mvk160 Heat and Mass Transport, (2010).
- 4- Keyong Chenga, B. , Chunzi Zhanga, Wei Chena, B, Shiqiang Lianga, Yongxian Guoa and Xiulan Huaia" Numerical Investigation of Film Cooling with Chemical Heat Sink" Frontiers in Heat and Mass Transfer (FHMT), DOI: 10.5098/hmt.v3.3.3003, ISSN: 2151-8629, (2012).
- 5- Reaz Hasann, Aginpuhukkudi" Numerical Study of Effusion Cooling on an Adiabatic Flat Plate" National Laboratory for Aeronautics and Astronautics, <http://dx.doi.org/10.1016/j.jppr>. (2013).

- 6-Weiguo Ai, Nathan Murray and Thomas h. Fletcher " Deposition Near Film Cooling Holes on a High Pressure Turbine Vane" Master Senesce, Journal of Turbo Machinery, DOI: 10.1115/1.4003672, (2012).
- 7- Fayyaz Hussain Asghar, and Muhammad Javed Hyder" Film Cooling Effectiveness from Single and Two in Lined / Staggered Rows of Novel Semicircular Cooling Holes" Research Journal of Engineering & Technology, Volume 31, No. 2 ISSN: 0254-7821, (2012).
- 8- Abdel-Mohimen and Higazy" Les of Turbulent Mixing in Anti-Vortex Film Cooling Flows" International Journal of Multidisciplinary and Current Research, ISSN: 2321-3124, (2013).
- 9- S. F. Shaker, M.Z. Abdullah, M. A. Mujeebu, K.A. Ahmad and M.K. Abdullah "Study on the Effect of Number of Film Cooling Rows on the Thermal Performance of Gas Turbine Blade" Journal of Thermal Science and Technology, ISSN 1300-3615, (2012).
- 10- M-N Nguyen, M Fénot, G. Lalizel and E. Dorignac" Experimental Study of Full Coverage Film Cooling Optimization" Journal of Physics: Conference Series 395, DOI:10.1088/1742-6596/395/1/012031, (2012).
- 11- Kamil Abdullah, Onodera Hisato, Funazaki Ken-Ichi1 and Ideta Takeomi" Heat Transfer and Aerodynamics Studies of Multiple Cooling Holes" International Journal of Gas Turbine, Propulsion and Power Systems, Volume 4, Number 1. February (2012).
- 12- Assim H. Yousif, Amer M. Al-Dabagh and Muwafag Sh. Alwan" Thermal Performance of Film Cooling for Two Staggered Rows of Circular Jet" Eng. & Tech. Journal Vol.31, No.1, (2013).

# Effect of using waste-iron on the mechanical properties of concrete

Wasan Q. Fayyadh

Civil engineering Department  
College of Engineering Thi-Qar University  
wasan\_rwsna@eng.thiqaruni.org

## Abstract

The aim goal of this research was to study the effect of using the waste-iron which product from milling processes on the mechanical properties of concrete. The tests performed to evaluate waste-iron concrete are compressive strength, splitting tensile strength and flexural strength tests. Sixty cubes of concrete for the compressive strength, sixty cylinders of concrete for the tensile strength, and Sixty prisms of concrete for the flexural strength tests with different volume fractions of waste-iron (1%, 2%, 3% and 4%) were prepared. The specimens were tested at 7, 14 and 28 days age. The results show that the concrete mixes with waste-iron have a higher compressive strength, tensile strength and flexural strength than the plain concrete mixes. Concrete containing volume fractions 3% ratio of waste-iron has the maximum value of compressive strength, tensile strength and flexural strength. The primary effect for adding the waste-iron to the concrete is to improve the post-cracking behavior.

**Keywords:** plain concrete, waste-iron, Slump test, compressive strength, tensile strength and flexural strength.

## تأثير استعمال برادة الحديد على الخواص الميكانيكية للخرسانة

### الخلاصة

الهدف من هذا البحث هو دراسة تأثير اضافة برادة الحديد الناتجة من عملية التفريز الى الخرسانة ودراسة تأثيرها على الخواص الميكانيكية للخرسانة ، لقد تمت دراسة مقاومة الإنضغاط ومقاومة الشد ومقاومة الإنثناء. في هذه الدراسة تم صب ٦٠ مكعب لفحص مقاومة الإنضغاط و ٦٠ أسطوانة لفحص مقاومة الشد و ٦٠ موشور لفحص مقاومة الإنثناء بنسب حجمية مختلفة من برادة الحديد (١%، ٢%، ٣%، ٤%) ، هذه الفحوصات تمت بأعمار مختلفة للخرسانة ٧ و ١٤ و ٢٨ يوم. أظهرت النتائج بأن الخلطات الحاوية على برادة الحديد لها مقاومة أنضغاط ومقاومة شد انشطاري ومقاومة أنثناء أعلى في الخلطات الحاوية على برادة الحديد. الخرسانة الحاوية على برادة الحديد بنسبة ٣% أعطت اعلى زيادة في مقاومة الإنضغاط ومقاومة الشد ومقاومة الإنثناء. والتأثير الأكبر لبرادة الحديد هي زيادة مقاومة التشقق للخرسانة.

## Introduction

The main goal of this research is to improve the mechanical properties for the concrete by using the recycle material, waste-iron. The reuse of waste is important from multiple points of view: it helps to save and sustain natural resources which cannot be replenished, it decreases the pollution of the environment and it helps to save and recycle energy in production processes.[8]

The concrete industry has begun adopting a number of methods to achieve goals [9] and [10] investigated the use of steel slag as an aggregate for concrete mixes; based on the short-term results and the crushing strengths; “slagcrete” appeared to have potential in the construction industry. Ghailan, [7] Utilized an industrial solid waste produced from the iron and steel industry. It was physically treated, fully inspected and incorporated into concrete coarse aggregate. The results confirmed that concrete mixes made with the waste material gave a higher modulus of rigidity, higher rebound number and higher chemical resistance towards the exposure to acids/ salts solutions as compared with conventional concrete mixes. [12] demonstrated that using waste iron filings as partial replacement of fine aggregate in concrete mixes offers higher strength values than that for the plain mixes.

Iron represents one of the major constituents of industrial solid waste are likely to include iron and steel manufacturing plants, as well as small and medium –sized workshops. Although there are no reliable data on the quantities of these wastes generated in Iraq. There are clear signs of a sharp increase in their accumulated quantities as discarded solid wastes due to the absence or poor functioning of systems for the collection, treatment and disposal of these wastes. The main goals of this study were to investigate the following:-

- Improve the properties of concrete by using the cheaper method, using the waste iron.
- The feasibility of reusing waste iron in concrete mixes in order to reduce the environmental impact resulting from waste iron disposal.

## 1. Materials

### 2.1 Cement:-

Type I Portland cement was used in this investigation, chemical analysis of the cement was carried out according to ASTM C150 and Iraqi standard No.5/1984. The chemical composition and physical properties of the cement are determined by the structural lab in the Engineering collage at Thi-Qar University. The chemical composition and physical properties presented in Table 1 and 2 respectively.

**Table 1. Chemical composition of cement**

Compounds	% (by weight)	Limit of Iraqi specification No. 5/1984
Lime	64.43	-
Silica	21.14	-
Alumina	5.78	-
Iron oxide	3.59	-
Sulfite	2.35	< 2.8%
Magnesia	1.52	< 5%
Loss of ignition	0.89	< 4%
Lime saturation factor	0.92	0.66 – 1.02
Insoluble residue	0.34	< 1.5
Main compounds (Bogue's equation) % by weight		
Name of compounds		
Tricalcium silicate	50.83	
Dicalcium silicate	22.30	
Tricalcium aluminate	9.25	
Tetra calcium aluminoferrite	10.90	

**Table 2:- Physical properties of cement**

Properties	Limit	Limit of Iraqi specification No.5/1984
Fineness ( $\text{m}^2/\text{kg}$ )	269.50	230 (min)
Initial setting time (min)	3:20	0:45 (min)
Final setting time (h)	4:15	10:0 (max)
Soundness	0.19	0.8 (max)
3 days age compressive strength (Mpa)	24.96	15 (min)
7 days age compressive strength (Mpa)	30.80	23 (min)

## 2.2 Coarse aggregate

Natural crushed stone aggregate with bulk density of  $1545 \text{ kg/m}^3$  and was used in this study. The properties and gradation of the coarse aggregate are shown in Table (3).

**Table 3:- Properties and gradation of the coarse aggregate**

No. Sieves (mm)	Percentage of Passing	Limit of Iraqi specification No. 45/1984
37.5	100	100
20	98	95-100
10	46	30-60
4.75	3	0-10
SO <sub>3</sub> %	0.085	≤ 0.1

### 2.3 Fine aggregate:-

Natural sand of desert origin the properties and gradation of the fine aggregate in the third zone are shown in Table (4).

**Table 4:- Properties and gradation of the fine aggregate**

No. Sieves (mm)	Percentage of Passing	Limit of Iraqi specification No. 45/1984
9.5	100	100
4.75	97	90-100
2.36	87	85-100
1.18	79	75-100
0.6	65	60-79
0.2	22	12-40
0.15	3	0-10
SO <sub>3</sub> %	0.482	≤ 0.5

### 2.4 Waste iron:-

Waste iron was obtained from the Engineering workshops in the Engineering collage at Thi-Qar University. This type of waste iron is normally generated in tremendous quantities from the milling operation in these workshops. A sample of the waste iron utilized in this study was shown in Fig. 1. The shape of this waste iron was spiral and it had a range length of 4cm. the aspect ratio is 1:8. The effect on workability is the aspect ratio ( $l/d$ ) of the fibers. The



workability decreases with increasing aspect ratio, in practice it is very difficult to achieve a uniform mix if the aspect ratio is greater than about 100.[15]

The chemical composition of the waste iron was determined by the state Company for Geological Survey and Mining in Iraq. The chemical composition and physical properties of the waste iron are presented in Tables 5 and 6, respectively.

**Table 5:- Chemical composition of waste iron**

Compounds	% (by weight)	Test method
Fe <sub>2</sub> O <sub>3</sub>	93.14	Titration with potassium dichromate using biphenyl amine as the indicator
Al <sub>2</sub> O <sub>3</sub>	<0.03	Auto color analyzer

**Table 6:- Physical properties of waste iron. [2]**

Properties	Limit	Test method
Fineness modulus	2.65	F.M=Accumulative percentage retained/100
Specific gravity	4.50	Somayaji, 1995
Density (kg/m <sup>3</sup> )	1946.70	ASTM C29-87
Color	Black-gray	



**Fig. (1) Waste-iron produced from milling process**

## **2. Experimental Work:-**

### **2.1 Mix Proportions:-**

Two types of concrete mixes were prepared according to the British standard in this study reference concrete mixes consisted of sand ( $715 \text{ kg/m}^3$ ), gravel ( $1020 \text{ kg/m}^3$ ), cement ( $380 \text{ kg/m}^3$ ) and a water-to-cement ratio of 0.53. The other concrete mixes were made with waste iron with different volume fractions (1%, 2%, 3% and 4%). Both types of concrete mixes were cured for 7, 14, and 28 days.

### **2.2 Preparation of concrete specimens :-**

Sixty cubes of concrete were molded for test the compressive strength. Sixty cylinders of concrete were molded for test the tensile strength. Sixty prisms were casted for testing the flexural strength. Casting, compaction and curing were conducted according to B.S. 1881-111:1997. Concrete casting was accomplished in three layers of 50 mm each. Each layer was compacted using a vibrating table for (1-1.5) min according to B.S. 1881-116:1997. until no air bubbles emerged from the surface of the concrete mold. The specimens were then left at room temperature. After 24 hours the concrete was removed from the molds, marked and submerged in fresh, clean water and then tested at a specified age. The slump test was carried out according to B.S. 1881-102:1997.

### **2.3 Testing of concrete specimens:-**

The most common concrete tests carried out in this study are the Compressive Test, Tensile Test and Flexural Test.

#### **3.3.1 Slump Test**

Slump test was carried out according to B.S. 1881-102:1997.

#### **3.3.2 Compressive Strength Test**

Concrete 150mm cubes, compressive test machine hydraulic test machine (MATEST) was used to complete this test. Sixty cubes with 0, 1%, 2%, 3% and 4% volume fraction of waste iron; four cubes for each ratio and for each curing periods 7, 14 and 28 days were used for this test. The compressive strength was carried out according to B.S. 1881-128:1997.

#### **3.3.3 Splitting tensile Strength Test**

Sixty cylinders (150x300) mm with different volume fractions 0, 1%, 2%, 3% and 4% volume fraction of waste iron, four cylinders for each ratio and for each curing periods 7, 14 and 28 days were tested. Splitting tensile strength was carried out according to B.S. 1881:1997.

### 3.3.4 Flexural Strength Test

Flexural test machine was used to complete this test. Sixty prisms (100 x 100 x 500mm) with different volume fractions (0, 1%, 2%, 3% and 4%) of waste iron were prepared, four prisms for each ratio and for each curing periods 7, 14 and 28 days. The specimens were cured; then tested according to B.S. 1881-128:1997.

## 3. Results and Discussion

The performance of the waste-iron was evaluated by determining the compressive strengths, tensile strengths and flexural strengths of the concrete specimens containing different volume fractions of waste-iron.

### 4.1 Workability of mixes

The results of the slump tests are presented in Table 7. The results demonstrate the tendency of the slump to decrease below the reference mix by 4.32%, 13.11%, 17.84%, and 29.60% for concrete mixes with different volume fractions 1%, 2%, 3% and 4% waste-iron respectively. This tendency might be due to the heterogeneity and shapes of the waste-iron particles, which lead to lower fluidity of the mixes.

**Table 7: Slump of waste iron concrete mix**

% Waste iron	0	1%	2%	3%	4%
Slump (cm)	7.4	7.08	6.43	6.08	5.21
Percentage decrease in slump	0	4.32	13.11	17.84	29.60

### 4.2 Compressive Strength

Compressive strength test results show that the compressive strength of waste-iron specimens increased with the increasing the ratio of waste-iron for all curing periods. Table 8 presents the increasing ratios of the compressive strengths of these mixes.

**Table 8: Compressive strength of waste iron concrete mix**

Volume fraction of waste iron	Comp. strength at 7 days (MPa)	Increasing ratio in 7 days	Comp. strength at 14 days (MPa)	Increasing ratio in 14 days	Comp. strength at 28 days (MPa)	Increasing ratio in 28 days
0	25.05	0.00	28.85	0.00	31.15	0.00
1	27.87	11.25	31.37	8.75	34.57	10.97
2	29.47	17.64	33.02	14.47	37.89	21.65
3	31.53	25.87	34.33	18.98	40.26	29.24
4	30.76	22.78	33.94	17.65	38.79	24.52

The results show that using waste-iron on the compressive strength of concrete for all curing periods relative to the reference mix. The effect of this type of waste-iron was similar to that for steel fiber reinforcement. The result shows that adding the waste-iron in the concrete result the increasing in compressive strength at all curing periods. The highest compressive strength was that in the concrete mixes made of volume fraction 3% of waste-iron fiber at 28 days curing period, which is 29.24% higher than the reference mix at the same curing period. In the volume fraction 4% of waste-iron had lower increasing in compressive strength than in the volume fraction 3% of waste-iron, this caused by the percentage decrease in slump was higher in the volume fraction 4% of waste-iron and this lead to decreasing the compact factor. However, the waste-iron does substantially increase the post-cracking ductility, or energy absorption of the material.[17]. The results shown in Fig.(3).

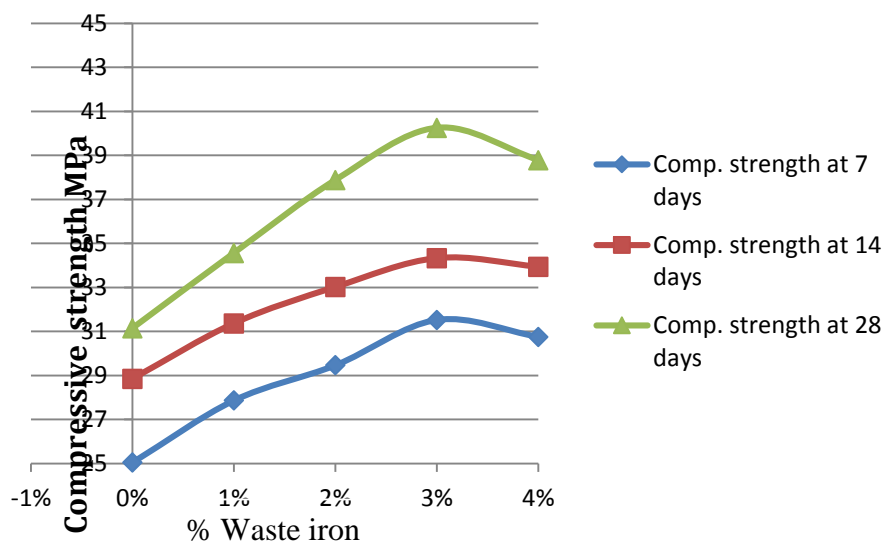


Fig.( 3 ). Compressive strength of waste iron concrete mixes

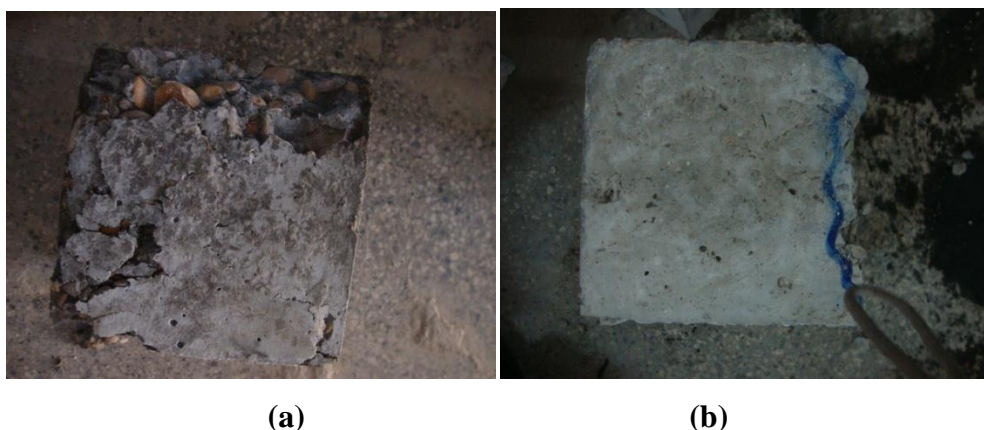


Fig.(4) Concrete specimens after failure in compressive strength test

(a) without waste-iron. (b) with waste-iron

### 4.3 Tensile Strength

The result of the tensile strength tests show that the tensile strengths of the waste-iron specimens increased with the increasing the ratio of waste-iron at all curing periods. Table (9) and Fig. (5) presents the tensile strengths of these mixes.

**Table 9: Splitting tensile strength of waste iron concrete mix**

Volume fraction of waste iron	Splitting tensile strength at 7 days (MPa)	Increasing ratio in 7 days	Splitting tensile strength at 14 days (MPa)	Increasing ratio in 14 days	Splitting tensile strength at 28 days (MPa)	Increasing ratio in 28 days
0	1.89	0.00	3.12	0.00	4.95	0.00
1	2.15	13.54	3.49	11.74	5.62	13.56
2	2.22	17.49	3.64	16.54	5.87	18.69
3	2.32	22.83	3.76	20.37	6.35	28.24
4	2.31	21.97	3.7	18.45	6.16	24.43

The result of the splitting tensile strength tests show that the tensile strengths of the waste-iron specimens increased with all the ratio of waste-iron at all curing periods.

Concrete containing 3% of waste-iron shows maximum tensile strength in comparison with other mixes. Concrete containing 4% of waste-iron had lower increasing in tensile strength than that containing 3% of waste-iron. This attribute to the decrease in the workability which leads to a decrease in the compact factor. For more or less randomly distributed fibers, the increase in strength is much smaller.[10]. However, adding the waste-iron is probably not worthwhile in tensile strength. However, as in compression, waste-iron does lead to major increases in the post-cracking behavior.[16].

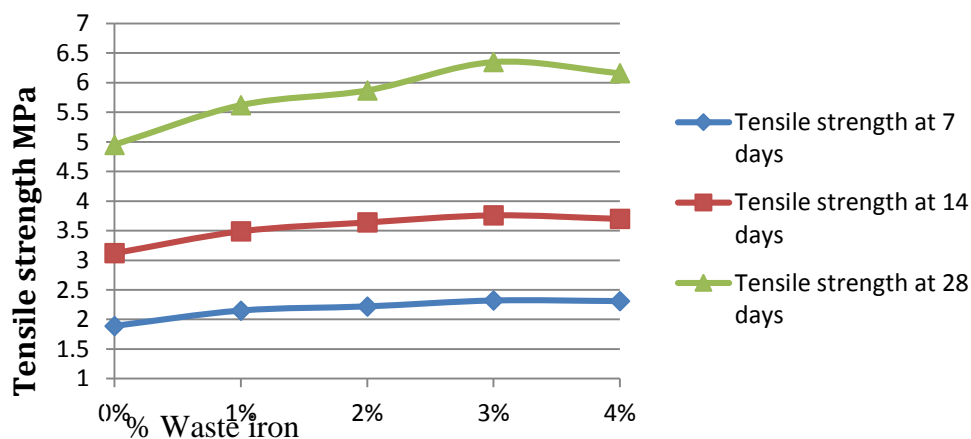


**Fig.( 5 ). Splitting tensile strength of waste iron concrete mixes**

#### 4.4 Flexural Strength

The result of the flexural strength tests show that the flexural strengths of the waste-iron specimens increased with all the ratio of waste-iron at all curing periods. For fiber reinforced concrete, the increase in flexural strength is particularly sensitive, not only to the fiber volume, but also to the aspect ratio of the fibers. The higher aspect ratio leading to larger strength increases.[18]. The maximum increase in flexural strength was for concrete containing 3% of waste-iron. Concrete specimens containing 4% of waste-iron had the lower increase in flexural strength than that containing 3% of waste-iron. This may be due to the decrease in workability which leads to decrease the compact factor of the concrete mix. Fibers are added to concrete not to improve the strength, but primarily to improve the toughness, or energy absorption capacity. [10]. Table (10) and Fig.(5). Presents the flexural strengths of these mixes.

**Table 10: Flexural strength of waste iron concrete mix**

% waste iron	Flexural strength at 7 days (MPa)	Increasing ratio in 7 days	Flexural strength at 14 days (MPa)	Increasing ratio in 14 days	Flexural strength at 28 days (MPa)	Increasing ratio in 28 days
0	2.1	0.0	4.5	0.0	6.1	0.0
1	2.32	10.4	5.2	15.2	8.8	44.3
2	2.98	42.1	6.77	50.4	11.6	90.2
3	3.64	73.2	8.08	79.5	12	96.7
4	3.32	58.1	7.26	61.4	10.2	67.2

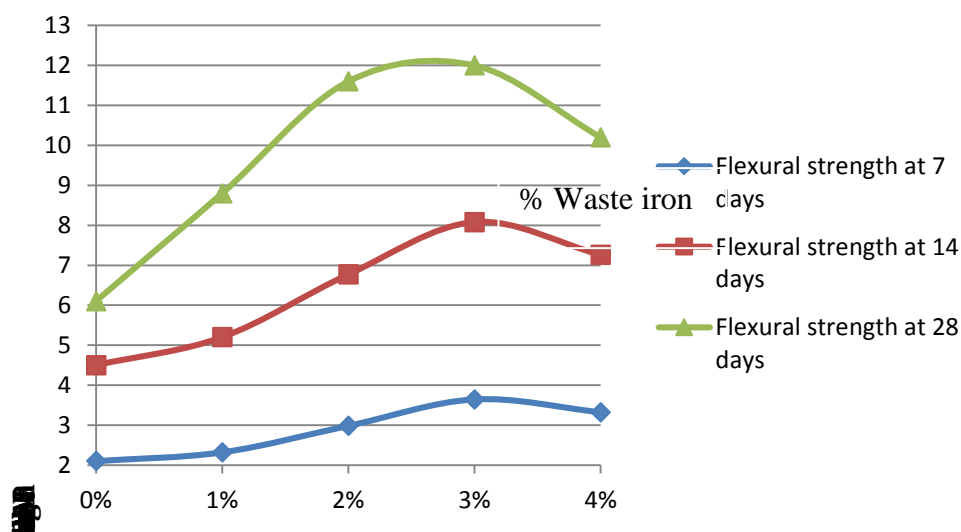


**Fig.( 6 ). Flexural strength of waste iron concrete mixes**



## Conclusion

The results of this investigation show that the use of waste-iron which product from milling processes performed efficiently to improve most properties:

1. The compressive strengths of waste-iron concrete mixes at all curing periods tend to increase relative to the reference mix. The highest compressive strength was that in the concrete mixes made of volume fraction 3% of waste-iron fiber at 28 days curing period, which is 29.24% higher than the reference mix at the same curing period.
2. The tensile strengths of waste-iron concrete mixes at all curing periods tend to increase relative to the reference mix. The highest tensile strength was that in the concrete mixes made of volume fraction 3% waste-iron fiber at 28 days curing period, which is 28.24% higher than the reference mix at the same curing period.
3. The flexural strengths of waste-iron concrete mixes at all curing periods tend to increase relative to the reference mix. The highest flexural strength was that in the concrete mixes made of volume fraction 3% ratio of waste-iron fiber at 28 days curing period, which is 96.7% higher than the reference mix at 28 days curing period.
4. The slump values of the waste-iron concrete mixes decrease with increasing the content of the waste-iron. In spite of this decline in the slump values of the concrete mixes, they remain easy to work. In practice it is very difficult to achieve a uniform mix if the aspect ratio is greater than about 100
5. Adding the waste-iron increases in the post-cracking behavior.
6. The color of the waste-iron concrete products did not change due the black-gray color of waste-iron.

## 4. References

1. Akinmusuru, J.O., 1991. Potential beneficial uses of steel slag wastes for civil engineering purposes. *Resources, Conservation and Recycling* 5 (1),73-80.
2. Somayaji,s. 1995. *Civil Engineering Materials*, prentice-Hall, Inc., Englewood cliffs, New Jersey.
3. British Standard Institution, 1997. *Methods of Testing Concrete*, B.S.1881, BSI, London.
4. Limit of Iraqi specification No. 5/1984 for Portland cement.
5. Limit of Iraqi specification No. 45/1984 for coarse aggregate.
6. Limit of Iraqi specification No. 45/1984 for fine aggregate.
7. Ghailan, A.H., 2005. Modified concrete by using a waste material as a coarse aggregate, in: *Construction Research Congress*. pp. 217-226.



8. Hassani, A., Ganjidoust, H., Maghanaki, A.A., 2005. Use of plastic waste (poly-Ethylene Terephthalate) in asphalt concrete mixture as aggregate replacement. *Waste Management & Research*. 23, 322-327.
9. Sear, L., 2005. Towards zero waste. *Concrete* 39 (5), 50-52.
10. Pezzi, L., De Lice, P., Vuono, D., Chiappetta, F., Nastro, A. (2006). "Concrete Products with Waste's Material (Bottle, Glass, Plate)." *Materials Science Forum*, 1753-1757.
11. Marzouk, O.Y., Dheilily, R.M., Queneudec. M. (2007). "Valorization of Post-Consumer Waste Plastic in Cementitious Concrete Composites." *Waste Management*, 27, 310-318.
12. Ismail, Z.Z., and Al-Hashmi, E.A. (2008). "Reuse of Waste Iron as a Partial Replacement of Sand in Concrete." *Waste Management*, 28, 2048-2053.
13. Kou, S.C., Lee, G., Poon, C.S, Lai, W.L. (2009). "Properties of Lightweight Aggregate Concrete Prepared With PVC Granules Derived from Scraped PVC Pipes." *Waste Management*, 29, 621-628.
14. M. Arabani, S. M. Mirbdolazimi (2011). "Experimental investigation of the fatigue behavior of asphalt concrete mixtures containing waste iron powder" *Materials science and engineering A*, 10-11, 3866-3870.
15. Maltigod shas V., Parker kent E., Wellman Dawn M., Wood Mrcus I. (2011). "Diffusion and leaching behavior of radio nuclides in category 3 waste. Encasement concrete and soil fill material". Department of Energy OSTI.
16. Archana Agrawal, S. Kumari, K. K. Sahu. (2011). "Studies on solvent extraction of iron (III) as a step for conversion of a waste effluent to a value added product". *Environmental Management*, 12, 3105-3111.
17. Maina, P. Mbarawa, M. (2012) "Blending lime and iron waste to improve sorbents reactivity towards desulfurization". *Fuel*, 162-172
18. Hamidul Bari, Mahbub Hassan, K. Ehsanul Haque, (2012). "Solid waste recycling in Rajshahi of Banhladesh". *Waste Management*, 11, 2029-2036.

## Wear Behavior of An Aluminum Alloys Using Nd:YAG Laser Treatment

Dr. Khansaa Dwood Salman and Dr. Muhannad Zedain Khalifa  
University of Technology- Electromechanical Engineering Department

### Abstract

This research aims to study the effect of laser surface treatment on wear resistance of different aluminum alloys (5086H-32, 6061T). The specimens were hardened by using pulse Nd:YAG laser with wave length 1064 nm and pulse duration 100 ns with constant energy 1 J and spot size 1–5 mm.

Wear behavior of the specimens as – received and specimens treated by laser being studied by using pin-on-disc technique under dry sliding wear conditions at different applied loads and different sliding speeds.

This study shows that the wear rate increases by increasing values of applied loads and decreases with increasing sliding speed, and wear rate for 6061-T6 alloy is less than 5086-H32 alloy. Also the results show that the micro hardness decreases by increasing hardening depth and the micro hardness values for 6061-T6 alloy more than 5086-H32 alloy at the same depth.

سلوك البليان لسبائك الألمنيوم باستخدام المعاملة السطحية بالليزر نيتيديوم – ياك

### الخلاصة

يهدف البحث لدراسة تأثير المعاملة السطحية بالليزر على مقاومة البلى لسبائك مختلفة من الألمنيوم (5086-T6, 6061-T6). تم تصليد العينات باستخدام ليزر نيتيديوم – ياك النبضي ذو الطول الموجي 1064 nm وزمن النبضة 100 ns عند طاقة ثابتة 1 J وقطر النبضة 1-5 mm.

تمت دراسة سلوك البلى للعينات قبل وبعد المعاملة بالليزر باستخدام تقنية المسمار-على-القرص تحت تأثير ظروف البلى الانزلاقي الجاف عند أحمال مختلفة وسرعات انزلاق مختلفة. أظهرت النتائج بأن معدل البلى يزداد بزيادة الحمل المسلط ويقل بزيادة سرعة الانزلاق، وأن قيمة معدل البلى للسبيكة 6061-T6 أقل مما هو عليه للسبيكة 5086-H32. كذلك أظهرت النتائج بأن الصلادة المايكروية تقل بزيادة عمق التصليد، وأن قيم الصلادة المايكروية للسبيكة 6061-T6 أكثر مما هو عليه للسبيكة 5086-H32 عند نفس العمق.

## 1- Introduction

Laser surface treatment for aluminum alloys have experienced extensive development in the past 10 years, aiming at modifying the shape and properties of aluminum components, particularly in the aerospace industry [1]. Aluminum is widely used in industry due to its low density, light thermal conductivity and good resistance to the corrosion ambient at room temperature. However the tribological properties of aluminum surface are poor and need improvement used in wearing environment [2].

More recently there has been a growing interest to improve the corrosion and wear performance of aluminum alloys by laser technique similar to those used for steel. The techniques principally involved are laser surface melting (LSM) and laser surface alloying (LSA). Laser surface hardening offers many advantages over conventional techniques (physical vapor deposition, chemical vapor deposition, sputtering, Sol-gel), localized/ bulk surfaces with superior surface resistance properties (wear, fatigue, corrosion, fracture, erosion) can be obtained. Laser surface hardening is a non contact process that in turn provides a chemically inert and clean environment as well as flexible integration with operating systems. High volume of production with superior surface quality and reasonable manufacturing cost are the foremost advantages [3,4].

On the other hand, high power pulse energy irradiation can modify metal surface and its process can be expected to increase hardened layer and then to improve the resistance of aluminum alloys [5]. Depending on the intended application, laser surface treatment can either improve wear behavior enhance fatigue properties or increase corrosion resistance. In some case all three properties can be improved [6].

There are many investigations were published in this field. P.H. change et al [7], they studied the influence of overlapped regions on corrosion and wear behavior of laser melted aluminum 2014-T6 alloy. Laser melting was carried out using a 3KW CW Nd:YAG laser with a line beam profile. The work revealed enhancement of wear resistance and pitting potential by 170 mv compared with that of untreated alloy. While F. Fariant et al. [8] reported the excimer laser cementation process which is developed to enhance the mechanical and chemical properties of a aluminum alloys. Fretting test measurements exhibit an improvement of the surface mechanical behavior for some experimental conditions. Majid Hamed Ismaiel and Mohamed Abdul Wahhab [9], they studied the effect of laser parameters which includes the effect of the pulsed Nd: YAG laser energy and the effect of number of shots (pulse) on wear rate of [Al-Cu-Si], [Al-Si-Mg] and [Al-Zn-Mg].

The aim of this paper is studying the performance of the effect of laser surface treatment at cryogenic conditions on microstructure, microhardness and wear characteristics of casting alloys 5086-H32 and 6061-T6.

## 2. Experimental Procedure

### 2.1 Materials under Test

The starting materials were aluminum alloys (5086-H32 and 6061-T6). Alloy 5086-H32 is solid solution strengthen is not age hardenable, widely used in cold worked conditions. While alloy 6061-T6 is age hardenable and is often used in construction of aircraft structures, such as wings and fuselages. The chemical compositions of these alloys were given in table (1), while table (2) shows the mechanical properties of these alloys.

**Table (1-a): Chemical Compositions of 5086-H32 Alloy.**

Element	Mg	Mn	Cr	Cu	Si	Fe	Ti	Zn	Al
Actual value wt%	4-6	0.45	0.15	-	0.52	0.35	-	0.19	Rem
Standard value wt%	3.5-4.5	0.2-0.7	0.058-0.25	0.1	0.4	0.5	0.15	0.25	Rem

**Table (1-b): Chemical Compositions of 6061-T6 Alloy.**

Element	Mg	Mn	Cr	Cu	Si	Fe	Ti	Zn	Al
Actual value wt%	1.0	-	0.2	0.27	0.63	0.57	-	0.2	rem
Standard value wt%	0.8-1.2	0.15	0.04-0.35	0.15-0.4	0.4-0.8	0.7 max	0.15 max	0.25	rem

**Table (2-a): The Mechanical Properties of 5086-H32 Alloy[10].**

Yield Strength (MPa)	Ultimate Tensile strength (MPa)	Elongation (%)	Modulus of Elasticity (GPa)	Hardness Hv (Kgf/mm <sup>2</sup> )	Poisson's Ratio
207	290	6-12	71.0	88	0.33

**Table (2-b): The Mechanical Properties of 6061-T6 Alloy[11].**

Yield Strength (MPa)	Ultimate Tensile strength (MPa)	Elongation (%)	Modulus of Elasticity (GPa)	Hardness Hv (Kgf/mm <sup>2</sup> )	Poisson's Ratio
276	310	12	68.9	107	0.33

## 2.2 Laser Surface Treatment

The laser-shock experiments were performed with a pulse Nd:YAG laser system. The laser was operate in a pulsed mode with wave length 1064 nm and pulse duration 100 ns for constant energy 1 J and spot size 1.5 mm while the frequency of laser system (1-6 Hz). The same conditions were done for the specimens of microhardness test.

## 2.3 Specimens Preparation

For microhardness test, the aluminum alloys samples have a diameter of 15 mm with 10 mm thickness, while in wear tests the samples have a diameter of 10 mm with 20 mm in height.

Before laser treatment, grinding and polishing were done to remove any foreign impurities, grinding was done by using emery papers 220, 500 and 1000  $\mu_m$  of Silicon Carbide to obtain smooth and uniform surfaces, and then the specimens were polished by using diamond paste for 1  $\mu_m$  in size.

## 2.3 Microhardness Test

Assessment of surface microhardness was done by using (Hensddt Wetzlar No. 23298) with applied load 300 gm. Microhardness calculates according to the following formula:

$$HV = 1.8544 \times \frac{F}{d_{ave}^2} \quad (Kgf / mm^2) \quad \dots(1)$$

where:

F : applied load (Kgf)

$d_{ave}$  : the mean diagonal of indentation (mm).

Case depth hardening is defined by three readings from the surface to the point at which the change in hardness, chemical composition or microstructure of the case and core can not be distinguished.

## 2.5 Microstructure Examination

A computerized optical microscopy was used to examine the microstructure of the specimens before and after surface treatment with Nd:YAG laser.

## 2.6 Wear Test

Wear test was done by using pin-on-disc machine. The instrument consists of an electric motor rotating at 750 r.p.m to a gear box and shaft where the specimen is mounted. Weight loss method was used to calculate the material that might be lost as a result of sliding wear. The specimen was mounted on its position in the instrument by direct contact with a very hard reference disc which has 45 HRC. Applied loads were changing by 2, 4, 6, 8, 10 N at the first stage with constant sliding speed equal to 1.5 m/s, while in the second stage the sliding speed was changing by 0.5, 1, 1.5, 2 m/s with constant load 6N for all aluminum specimens before and after laser surface treatment.

Wear rate can be calculated by the following equation [12].

$$W.R = \frac{w_1 - w_2}{S_D} \quad (gm/mm) \quad \dots\dots(2)$$

where :

W.R: wear rate (gm/mm).

w<sub>1</sub>: weight of the specimen before wear test (gm).

w<sub>2</sub>: weight of the specimen after wear test (gm).

S<sub>D</sub>: the distance of sliding (mm).

$$S_D = S \times t \quad \dots\dots(3)$$

where :

S: the sliding speed (m/s).

t : the time for the sliding (min).

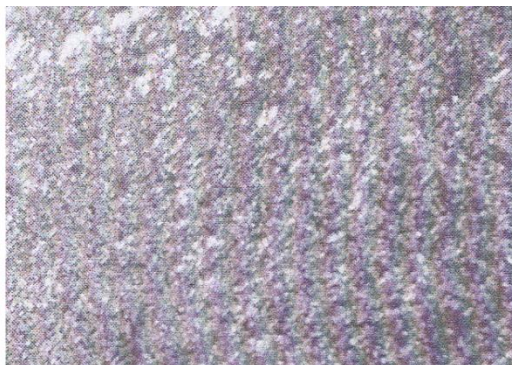
Before and after the wear test, the wear test, the specimens weight was separately measured to calculate the weight loss in the test by using an analytical balance with accuracy of 0.1 mg.

**Note: In this study the time is constant = 20 min.**

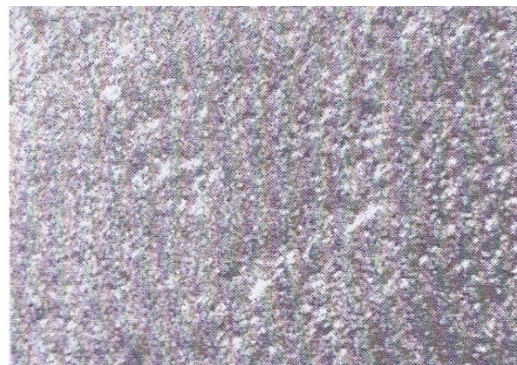
### 3. Results and Discussion

#### 3.1 Metallographic Evaluation

The specimens of aluminum alloys were heated by laser heat treatment. Subsequent rapid cooling led to the formation of a hardened surface layer. Because of the very short time involved during laser heat treatment, the finer grain size resulting in the formation of unusually fine structure was obtained. Figure (1) shows the microstructure of the specimens of Al alloys 5086-H32 and 6061-T6 before and after laser surface treatment.

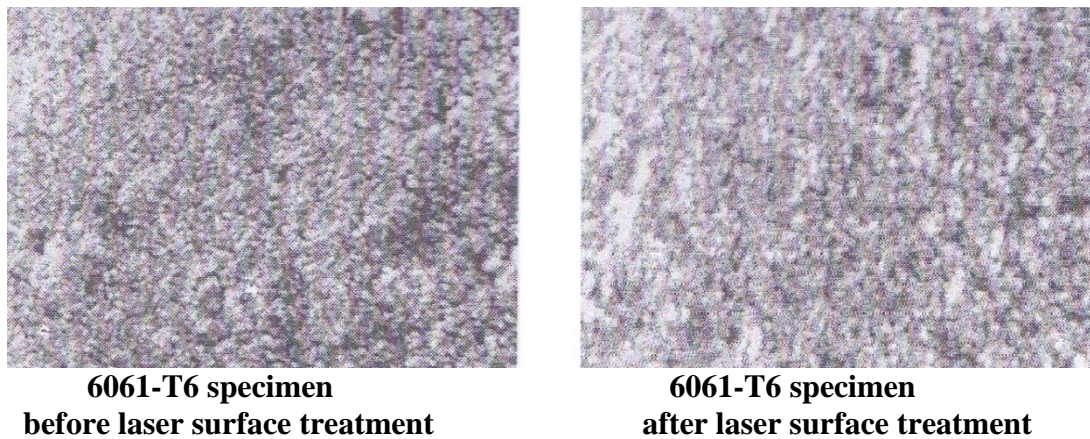


**5086-H32 specimen  
before laser surface treatment**



**5086-H32 specimen  
after laser surface treatment**





**Figure(1): Photomicrographs of surface microstructure of the specimens before and after laser surface treatment with magnification (200x).**

### **3.2 Microhardness Analysis**

Figure (2) shows that the laser surface treatment leads to increase the microhardness of 6061-T6 alloy more than for 5086-H32 alloy, it is attributed to that the effects of high amplitude stress waves on the microhardness. These stress waves are often generated by explosive changes or impact between a project and target specimen. One of the most interesting effects is that the shock waves can develop significant plastic strains in the metal.

When the intense laser beam strikes the metal surface, the surface layer is instantaneously vaporized. The rapidly expanding high temperature vapor exerts a pressure on the target surface which then propagates into the specimen as a stress wave. High surface pressures are obtained by placing on the target surface an overlay transparent to the laser beam for 6061-T6 alloy more than 5086-H32 alloy, which confines the blow-off material between it and the specimen surface for duration of laser pulse.

Figure (2) shows that the microhardness decreases below the surface of the specimens toward the core of them, and the microhardness for 6061-T6 specimen more than 5086-H32.

### **3.3 Effect of The Applied Loads and Sliding Speeds on Wear Behavior**

The wear rate is an important factor to be considered in surface treatments. At the steady state and in all contact pressure range, the friction of the 6061-T6 treated specimens presented a lower wear rate than 5086-H32.

As a result, for all loads, 6061-T6 specimen presented a lower wear rate (higher wear resistance) and the friction increased with increasing applied load. While the high hardness of the specimens makes laser surface layer very difficult to be plastically deformed with little adhesive features, the surface of the specimen 5086-H32 is soft, having much adhesive features. Therefore, the friction of the laser treated specimens 6061-T6 present a lower wear rate than the specimens 5086-H32.

The fluctuation of the friction caused by materials transfer and oxidation occurred in the wear process. These oxide films could act as solid lubricant and avoid direct metallic contact with the coupling counterpart with the advantage of diminishing the friction. The friction heat produced during the sliding friction test resulted in the formation of oxide films on the contact surfaces. Furthermore, higher friction contact temperature may cause larger areas of oxide films formed on the wear surfaces. Wear rate was measured to compare the weight losses of the specimens 6061-T6 and the specimens 5086-H32. Wear weight loss and wear track depth of the laser treated specimens 6061-T6 were lower than those of 5086-H32. Because the hardness of the specimens surfaces of 6061-T6 was higher than that of 5086-H32 and then the wear rates of them were low.

The wear rate is often used to evaluate wear resistance performances. It shows that the specimens of 6061-T6 are more resistant to wear than the specimens 5086-H32 with excellent abrasive and adhesive wear resistance under sliding wear test conditions, because the surface strength and hardness of the specimens are significantly enhanced by laser treatment. Figure (3) shows that increasing applied loads lead to increase the wear rate, and the wear rate for the specimens 6061-T6 lower than for the specimens 5086-H32. While increasing the sliding speed lead to decrease the wear rate because of the strain hardening occurred in the specimens which lead to increasing strengthening, and for the specimens 6061-T6 lower than for the specimens 5086-H32. Figure (4) shows that increasing the sliding speed leads to decrease the wear rate, and the wear rate for the specimens 6061-T6 lower than for the specimens 5086-H32.

### 3.4 The Roughness Values Under Sliding Wear Test Conditions

The quantitative characterization of the worn specimen surface roughness in table (3) indicates that the wear processes in the specimen of 6061-T6 were dominated by polishing wear and the wear surface was relatively smooth and the roughness values decreased. An increased in the roughness values is observed in the surface of the specimen 5086-H32 after wear test.

The laser-hardened surface exhibited good wear resistance, the grooves of the laser-hardened surfaces are relatively shallow due to the higher hardness of the surface and the severity of micro ploughing is comparatively less pronounced on the worn surfaces of 6061-T6 hardened specimens. But the results of wear tests of 5086-H32 hardened specimens presents deeper grooves.

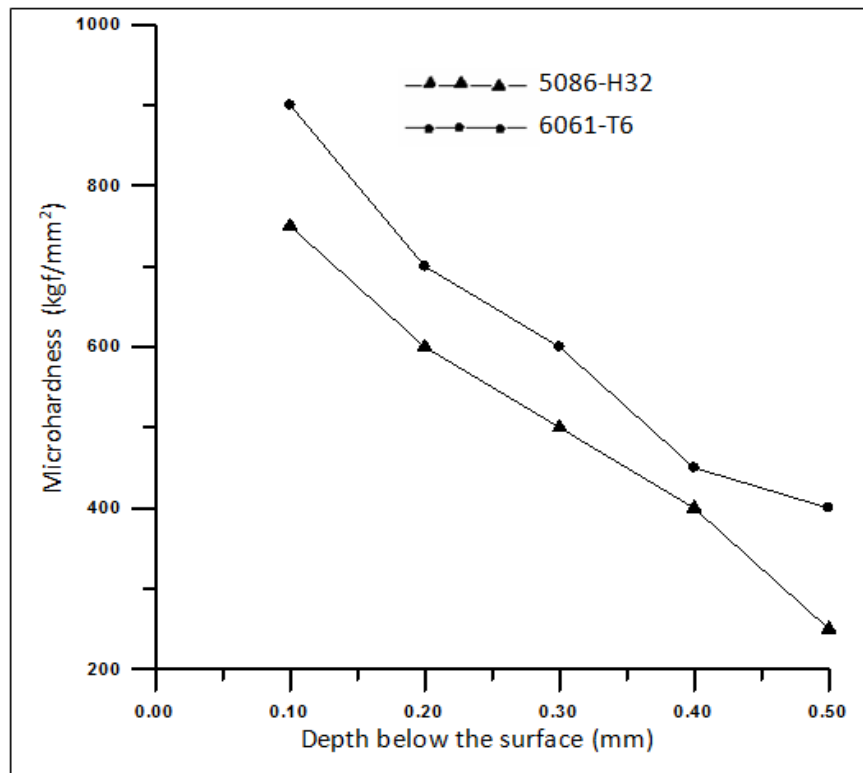


**Table (3): The Roughness Values Of The Specimens Treated By Laser.**

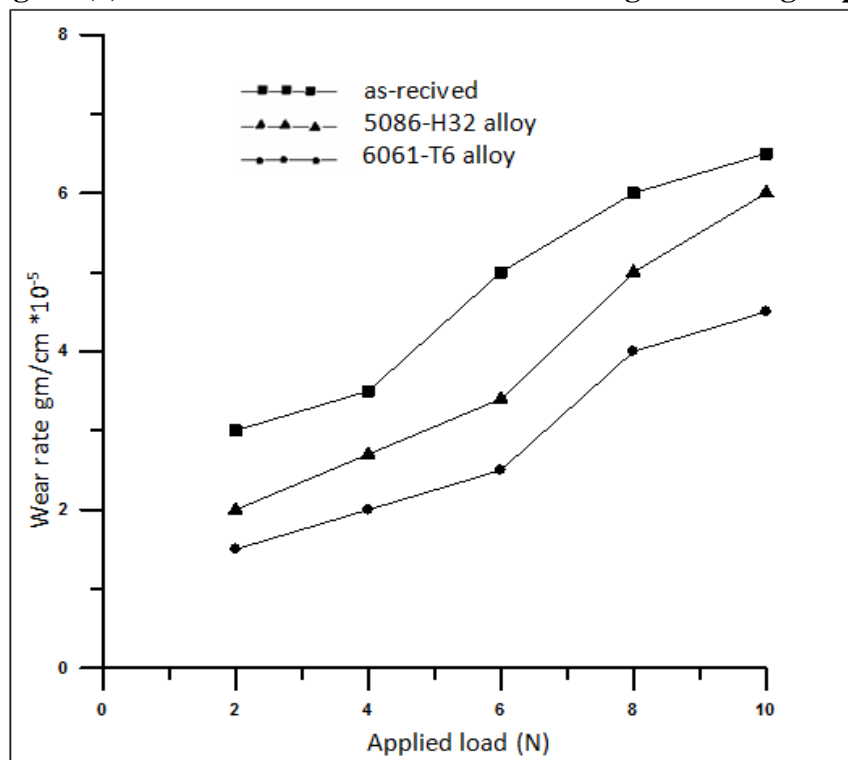
<b>Specimen</b>	<b>The roughness values Ra (<math>\mu\text{m}</math>) before wear test</b>	<b>The roughness values Ra (<math>\mu\text{m}</math>) after wear test</b>
<b>5086-H32</b>	<b>0.089</b>	<b>0.185</b>
	<b>0.111</b>	<b>0.376</b>
	<b>0.204</b>	<b>0.823</b>
<b>6061-T6</b>	<b>0.075</b>	<b>0.086</b>
	<b>0.098</b>	<b>0.115</b>
	<b>0.125</b>	<b>0.277</b>

Figure (5) shows the optical micrographs of the top view of the wear surface of the specimens 5086-H32 and 6061-T6, it can be observed that the main wear mechanism for each specimen treated by laser are similar, generally involving adhesive and material transfer and wear induced oxidation and plowing. Adhesive between the specimens and counter body according accompanied by material detachment and transfer to the counter body occurred during sliding processes. In the specimens of 6061-T6, the worn surface of the specimen is relatively smooth Fig (5-a), the relatively smooth and slight micro-cutting worn surface without significant plastic deformation and deep parallel plowing grooves are visible. The worn surface shows fine wear debris, reaction products (oxides) Fig (5-b). Their counter surface is covered with large black oxide layer on the worn surface.

In the specimens of 5086-H32, the basic mechanism remains unchanged and only the grooves become slightly deeper. Fig(5-c) presents an optical micrograph showing plowing marks on the worn surface as well as some very small debris, reaction products (oxides). While as shown Fig (5-d), some rugged areas are visible on the cleaned worn surface. Their counter surface exhibits no plowing marks and is covered with thin black oxide layer on the worn surface.



**Figure (2): Hardness Distribution Curves Along Hardening Depth**



**Figure (3): The Relationship Between Wear Rate And Applied Load With Constant Speed (1.5 M/S).**

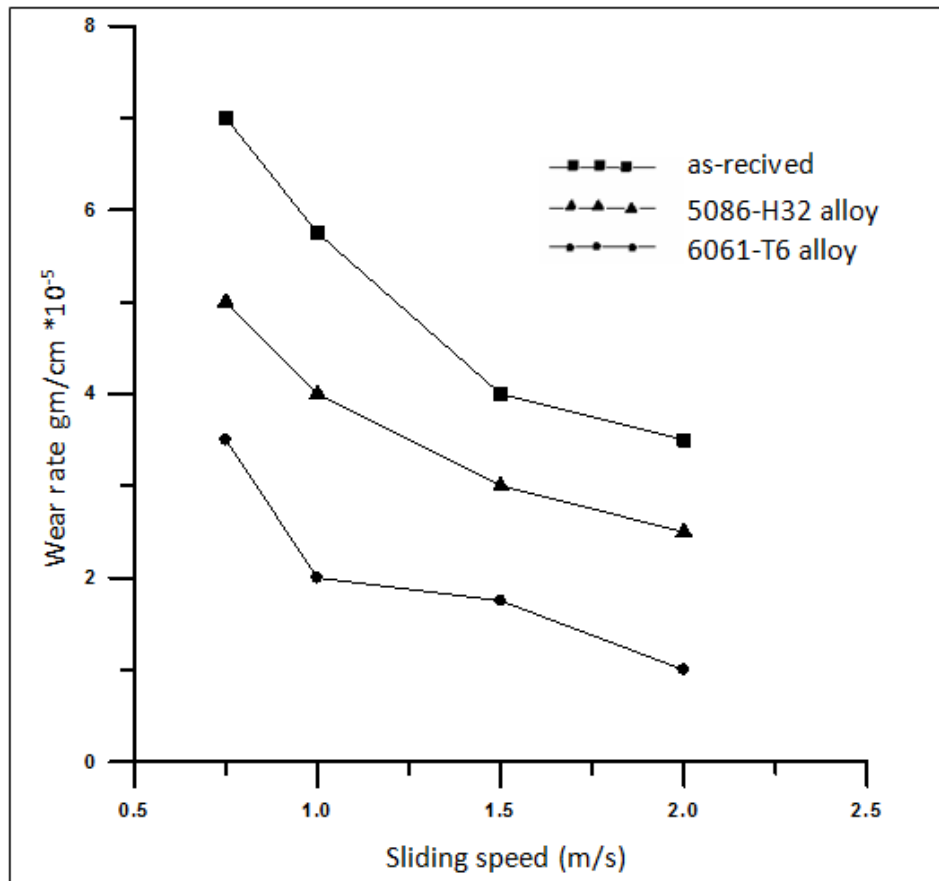
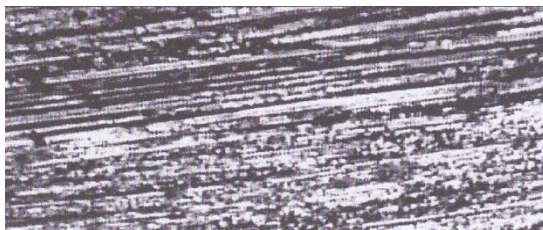
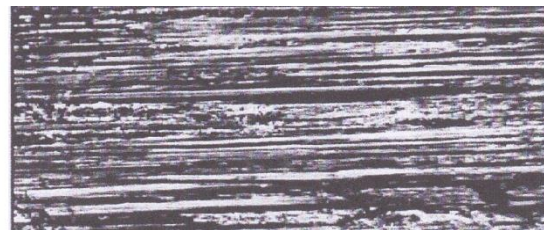


Figure (4): The Relationship Between Wear Rate And Sliding Speed With Constant Load (6 N).



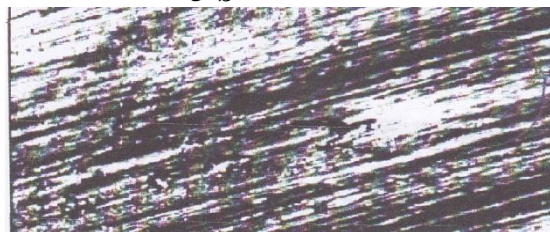
5-a



5-b



5-c



5-d

Figure (5): Photomicrographs of Worn Surface of The Specimens.

#### 4. Conclusions

1. Laser surface treatment leads to improve wear resistance for two aluminum alloys (5086-H32, 6061-T6).
2. The microhardness decreases by increasing the hardening depth and the microhardness values for 6061-T6 alloy more than 5086-H32 alloy at the same depth.
3. Increasing the applied loads leads to increase wear rate for the specimens 5086-H32 more than for the specimens 6061-T6 after laser treatment.
4. Increasing the sliding speeds leads to decrease the wear rate for the specimens 6061-T6 more than 5086-H32 after laser treatment.

#### References

- [1]. G. Fribourg, A. Deschamps. Y. Brechet. G. Mylonas, G. Labeas, U. Heckenberger, M. Perez, " Microstructure Modifications Induced by a Laser Surface Treatment in an AA7449 Aluminum Alloys", Materials Science and Engineering A528, pp.2736-2747, 2011.
- [2]. B.S. Yibas, A.F.M. Arif, C.Caratas and K. Raza, "Laser Treatment of Aluminum Surface : Analysis of Thermal Stress Field the Irradiated Region, Journal of Materials Processing Technology, Volume 209, Issue 1, pp.77–88,2009.
- [3]. K.G. Wakins, M.A. Memahon and W. M steen, " Microstructure And Corrosion Properties of Laser Surface Processed Aluminum Alloys " , Materials Science and Engineering: A, Volume 231, Issues 1–2, pp. 55–61, 1997.
- [4]. Narendra B. Dahotre, "Laser Surface Hardening", ASM Handbook, Volume 4A, Steel Heat Treating Fundamentals and Processes, 2013.
- [5]. Masatosgi Enomoto, Sadao Kokubo and Kazuhiro Nakata, " Surface Treatment of Aluminum Alloy with Laser Irradiation To Increase Wear Resistance ", Materials Science forum vols.(539-543), pp. 404-410, 2007.
- [6]. H .W. Bergman, D. Muller, T. Endres, R. Damascheck, J. Domes and A. S. , "Industrial Applications of Surface Treatments with High Power Lasers", Materials Science forum vols. (163-165), pp. 377-404, 1994.
- [7]. P.H. Chong, Z. Liu, P. Skeldon and G.E. Thompson, " Large Area Laser Surface Treatment of Aluminium Alloys For Pitting Corrosion Protection" , Applied surface Science vols. (208-209), pp. 399-404, 2003.
- [8]. F. Fariout, C. Boulmer-leborgn , E. Le Men, T. sauvage, C. Andeeazza, P. Andeeazza, . Langlade, " Surface Carburization Of Aluminum Alloys By Excimerlaser ", Proceedings of the 28th International Conference on Metallurgic Coatings and Thin Films, Vols. 146–147, pp. 324–330, 2001.
- [9]. Majid Hamed Ismaiel and Mohamed Abdul wahhab, " Surface Treatment of Aluminum Alloys using Nd: YAG laser "En& .Tech. Journal, Vol .29 ,No .14, pp. 3006-3018, 2011.
- [10]. <http://asm.matweb.com> , 5086-H32 -ASM Material Property Data-Matweb.
- [11]. <http://asm.matweb.com> ,Glemco, Aluminum 6061-T6 -ASM Material Property Data-Matweb.
- [12].<http://books.google.iq>, Colin E. Webb, Julian D. C. Jones, " Handbook of Laser Technology and Applications: Laser Design And Laser Systems", Volume II, ©IOP Publishing Ltd 2004.

## **Identification of Impressed Current Cathodic Protection System (ICCP) By Artificial Neural Network.**

MARWA S.HASHIM \*, DR. KHEARIA A.MOHAMMED A. \*, DR. NAWAL JASIM  
HAMADI\*\*

\*Basra University ,College of Engineering ,Department of Electrical Engineering.

\*\* Basra University ,College of Engineering ,Department of Material Engineering.

### **ABSTRACT**

The corrosion of metallic structures buried in soil or submerged in water which became a problem of worldwide significance and cause most of the corrosion in petroleum industry can be controlled by cathodic protection. Cathodic protection (CP) is a popular technique used to minimize the corrosion of metals in a variety of large structures . In this study the identification of impressed current cathodic protection system was presented and the results were simulated by artificial neural networks for system identification which was implemented using MATLAB R 2010 A programming. The best network architecture was chosen for protection system. The multilayer feed forward network for neural network was used. The four environment variables (conductivity C, temperature T, aeration factor A, and potential reading V) were used as the input to the network to identify the minimum current density as output in a feed forward network structure with one hidden layer using the practical results data for the learning process which was concluded.

### **1.INTRODUCTION**

In order to occur the corrosion ,four components must be exist and active. These components are the anode, cathode , electrolyte, and metallic path .All of these parts must present for corrosion to occur [1-3].Major pipelines across the world transport large quantities of crude oil, natural gas, and petroleum products[4]. Changing a pipeline in the case of oil and gas industry is a very time consuming and expensive procedure [5]. To control pipeline's corrosion the cathodic protection is used throughout the world [6].

Cathodic protection(CP) is an electrical method to prevent corrosion on metallic structures which are buried or submerged in electrolytes such as soil or water.CP does not work on structures exposed to air environments. The air is a poor electrolyte (non conductive) , and it prevents current from flowing from the anode to the cathode[6]. The principle is to make the potential of the whole surface of the structure sufficiently negative with respect to surrounding medium to ensure that no current flows from the metal to the medium. This is done by forcing an electric current to flow through the electrolyte towards the surface of the metal required to be protected[7]. There are two ways of applying CP system in environment such as water or soil [8-10]:

(i) Sacrificial anode method(SACP)which uses an active anode of more negative potential than the structure to be protected and electrically connecting it to form a cell and buried in the electrolyte. The active metal anode corrodes (is sacrificed) while the metal structure cathode is protected. It is used mostly on underground structures, where CP current requirements are relatively small and where the soil resistivity is low, say less than 10,000  $\Omega \cdot \text{cm}$  .(ii) Impressed current method(ICC) which uses an inert anode to impress current from an external source. In this study we concerned with(ICC). In South Oil Company (SOC) in Basra , there are many ICC stations, 10% of them are worked by solar energy ,5% worked by gas and 85% remainder worked by rectifier .These stations are a wide spread at a variety of locations. The pipes of SOC are tested periodically to ensure that they are protected cathodically according to the standard method[10]. This is typically done by field engineers or technicians who travel to each rectifier and test station and conduct a series of measurements for the potential and current with hand-held meters..The intelligent techniques are used successfully in a variety of applications. One of them is the cathodic protection system. Examples of these techniques used in cathodic protection are artificial neural network and fuzzy logic. The present work aims to installation Impressed Current Cathodic Protection (ICC) System and use the neural network to identify the proposed system to protect carbon steel pipe.

## 2.EXPERIMENTAL WORK

### A. Materials

The material used in present study is carbon steel pipe (ASTM API-5L) type as X60 steel because it is widely used in the oil field-Basrah as its price is relatively low, while it provides material properties that are acceptable for such application. It is neither extremely brittle nor ductile due to its low carbon content. It has relatively good tensile strength and is malleable. Its chemical compositions are (C=0.18, P=0.063, Mn=0.52, S=0.039, Si=0.24, Ni=0.10, Cu=0.29, Fe=Remainder).It is placed horizontally at a depth of 5 cm below the corrosive solution and 5 cm above the bottom of the bath. The glass bath was provided with aeration facility with dimension of (10 cm length, 5.2 cm inside diameter , 6 cm outside diameter , 4 mm wall thickness).

The auxiliary electrode used was a rod made of graphite with dimension of (20 cm length, and 1cm diameter) . This rod was located horizontally opposite to the working electrode (cathode) at the same level. The graphite anode is one of the most commonly used for impressed current systems, and was chosen for the following reasons [11]: a) Low in cost and it is non consumable, b) Readily available in a variety of sizes, c) Dose not form a high resistance layer of corrosion product, d) Environmentally safe, e) Application of these anodes



is restricted to those with low current requirement and f) Graphite anode performance is better in seawater than in fresh water. The other materials used are shown in Fig.(1).

### **B. Solutions**

The solutions used were experimentally prepared in different concentrations of (0 , 0.75 , 1.5 , 2.25 , 3 & 3.5 ) % by adding different weights of (7.5, 15, 22.5, 30 & 35) gm sodium chloride NaCl to 1 litter of distilled water which was supplied by Najibia Power Station Basra with a pH of 6.8 to obtain corrosive solution with different conductivities as (0.025, 17.5, 32.9, 46.6, 60.8, 69.8 ) mS/cm respectively. The NaCl was a commercial type with purity of about 90% which was used as corrosive solution. The cathodic protection system rig was assembled as shown schematically in Figure (1). ) on the basis of the design criteria proposed by some research workers [ 11, 12, 13].

### **3.EXPERIMENTAL PROCEDURES**

#### **A. Sample Preparation and Connections :-**

The pipe segment (cathode) which was placed in the ICCP system was abraded successively using emery paper to 800  $\mu$  in sequences until obtaining a smooth clear surface, then washed with distilled water, and dried with cleaned tissues and finally left to dry by air. A couple of copper wires were connected to the clean pipe surface by braze welding. One of these wires was connected to the negative terminal of DC power supply and the other was connected to the reference electrode which was used to measure the cathodic potential .

#### **B.INSTALLATION AND MEASUREMENTS OF ICCP SYSTEM :-**

The ICCP system was installed as shown in Figures (1). A Luggin capillary bridge leading to the reference electrode was mounted at the first edge at the center point of the cathode length within  $\approx$  (1-2) mm from the side of the cathode. The opening of the capillary tube located near working electrode (cathode) was equal to ( $\approx$  1mm) in diameter. The working and auxiliary electrodes were 40 cm apart and immersed in the solution at a depth of 5 cm from the top and the bottom respectively. Different weights of NaCl were dissolved in distilled water to 24 liter .The electrolytic solution was stirred by electrical stirrer to obtain a homogenous solution and the temperature of the solution was adjusted and changed in the range (20-45)  $^{\circ}\text{C}$  at each run. Another parameter was also aimed to be studied such as aeration from air pumping device which was placed at the centre point of the tank between the anode and cathode. The aeration flow rates employed were adjusted at (600, 1500, 1800) L/m to promote various corrosion rates of steel at the specified salt concentrations and at definite temperature. At these conditions the electrode potential was measured with respect to saturated calomel electrode using multi-range voltmeter. The voltage of the D.C power supply was constant at 10 V. To make the protection value of potential at required level the resistance of the circuit was

changed until the optimum value was obtained. The current was recorded each 15 min, when the value reached the steady state value i.e. giving the best value of impressed current required for complete cathodic protection, the corresponding voltmeter reading was also recorded. Continuous stirring of the corrosive environment was adapted to accelerate the corrosion process under dynamic condition compared to unstirred static one.

#### **4. EXPERIMENTAL RESULTS & DISCUSSION**

##### **A. Effect of Conductivity**

Numbers of experiments were carried out to show the effect of solution conductivity on cathodic protection current. It was clear that, whenever the electrical conductivity of a solution increased with salt concentration increment, the impressed current required for protection increased. That is because NaCl is an ionic compound, thus when it is dissolved in water conducts electricity and cause more current flow which leads to more CP current to be required. Figures (2) & (3) show the increment of CP current as conductivity of solution increased in different conditions of temperature with aeration.

##### **B. Effect of Temperature**

From data measurements, it is apparent that the cathodic current increased as the solution temperature increased. The increase of temperature reduces the solubility of dissolved oxygen with subsequent decrease in the rate of oxygen diffusion to the cathode surface then the rate of corrosion was diminished. Figures (4) & (5) show the increment of CP current as temperature increased at different conditions of solution conductivity at different aeration flow rates.

##### **C. Effect of Aeration Flow Rate**

The results showed that there is an increase in the current required as aeration flow rates of the solution increased, but this increment is relatively so small. This is due primarily to the increased availability of reducible species (i.e. oxygen) at the structure surface and the resulting increase in the rate of the reduction reaction, i.e. consuming more electrons. When the introduced oxygen to the solution by air pumping and allowed it rapidly to penetrate from the air to the solution (for open systems as in the experiments presented in this study), and through the solution to the metal surface, besides other reducible species, which increase the current required for protection. After a definite time interval when the solution becomes saturated by oxygen, it reaches a steady state condition and the current did not changed. Figures (2), (3), (4), (5) show the increment of CP current as aeration flow rates increased at different solution conductivity and at different temperatures.



## 5. THEORETICAL RESULTS

### Identification of CP System by ANN

System identification is the methodology of building mathematical models of dynamical systems based on input- output data[14]. The area of system identification is one of the most important areas in engineering because most of the dynamical system behavior can be obtained exploiting system identification techniques. Because of the function approximation properties and learning capability, Artificial Neural Networks (ANN's) have become a powerful tool for these complex applications. At present, most of the work on system identification using neural networks are based on multilayer feed-forward neural networks with back propagation learning or more efficient variations of this algorithm[15]. for cathodic protection application; a neural network model was chosen as the performance of the chosen model which was tried to maximize the convergence and accuracy of prediction between cathodic protection experimental results and neural network output. In the case study of cathodic protection system the parameters which introduced as components of input vectors indicated by the solution conductivity which were obtained by variation of NaCl solution concentration v. Also, the temperature , aeration factor, reference electrode (CSE) reading (in range of cathodic protection). The output vector will be the target i.e. the protection current required to accomplished full protection for submerged pipe. In this study the testing set contains 25 % of total experimental data while the rest were used for training.

#### 1. Weights initialization

The first step in the neural networks computations, prior to training a neural network, is to initialize the weight factors between the nodes of the different layers such as input to hidden layer and hidden to output layer. Since no information about the system being modeled is available, in the present study random numbers were used to initialize the weight factors of the neural network. This selection was found to generate the different MSE error at any time the neural program is executed [16,17] .

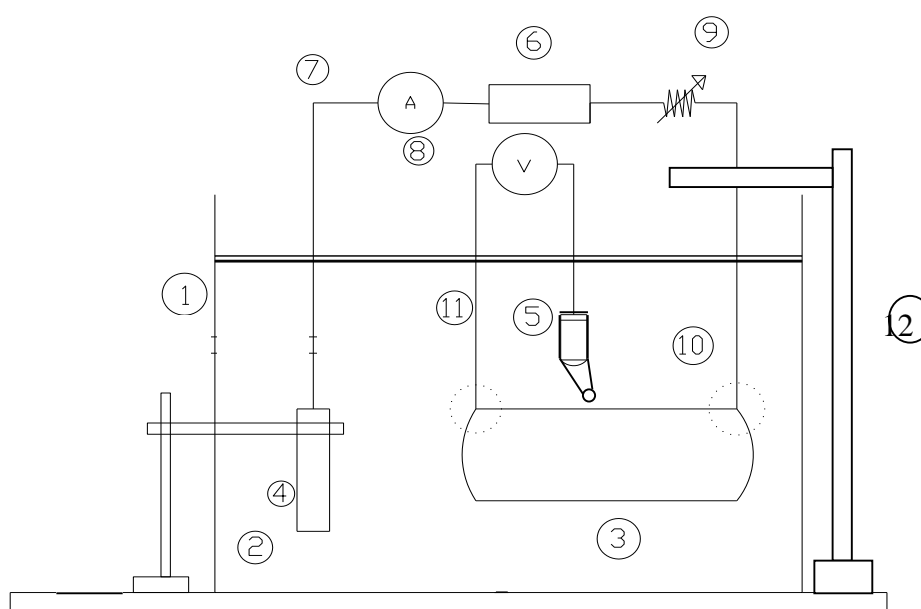
#### 2. Number of Hidden Layers & Number of Nodes in Each one

In the present study the artificial neural network was tested by one hidden layer, when single hidden layer was used with tansig as a transfer function in hidden layer and purelin function in output layer. Different number of nodes selected (from 1 to 20) in this case the best performance shows at 15 nodes which were obtained after 3000 (epochs) with MSE (1.8E-2) .The proposed CP neural network model can be represented schematically in Fig. (6) and Fig (7) shows cathodic protection system identification by neural network where the actual experimental output(blue)and the ANN output (red) after the learning process and it is clear that the two are almost identical which indicates that a good learning process was

achieved. Figure (8) shows the performance of the ANN and Fig.(9) shows the correlation coefficient of the network

### 3. Testing

An important aspect of developing neural networks is the determining how well the network performs once training is completed[18]. If the network has been trained sufficiently, the network output will differ only slightly from the actual output data. The network was tested to check if the performance denoted by (MSE) for training sets might diverge. In order to confirm these results, the actual values are compared to those predicted by the neural network for the generalizing patterns. Figures (10-13) show the outputs of the neural network for generalizing set plotted versus the targets where they are almost identical for the proposed ANN model.



1.Glass bath	5.Reference Electrode+ Luggin Capillary	9.Resistance Box
2.Solution Point	6.Power Supply	10.Drain
3.Cathode Point	7.Multi Rang Ammeter	11.Test
4.Anode	8.Multi Range Voltmeter	12.Stands

**Fig.( 1) Block Diagram of the installed ICCP Rig.**

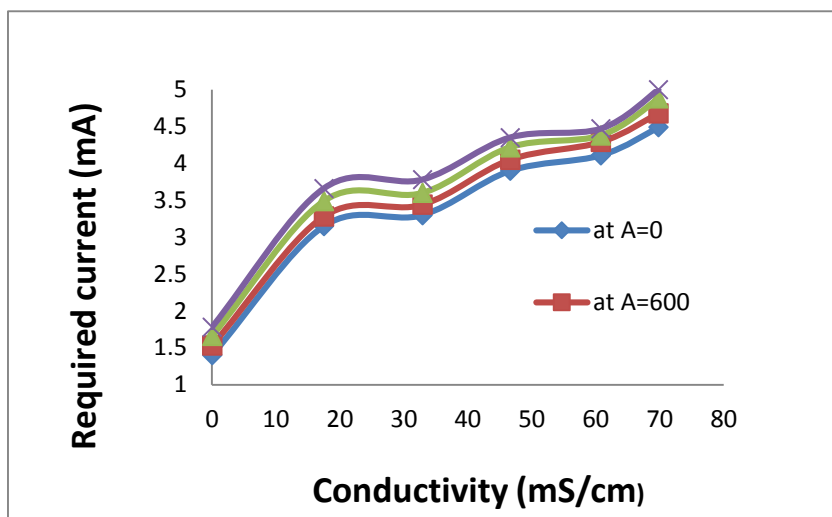


Fig. (2) CP current vs conductivity at 20 °C

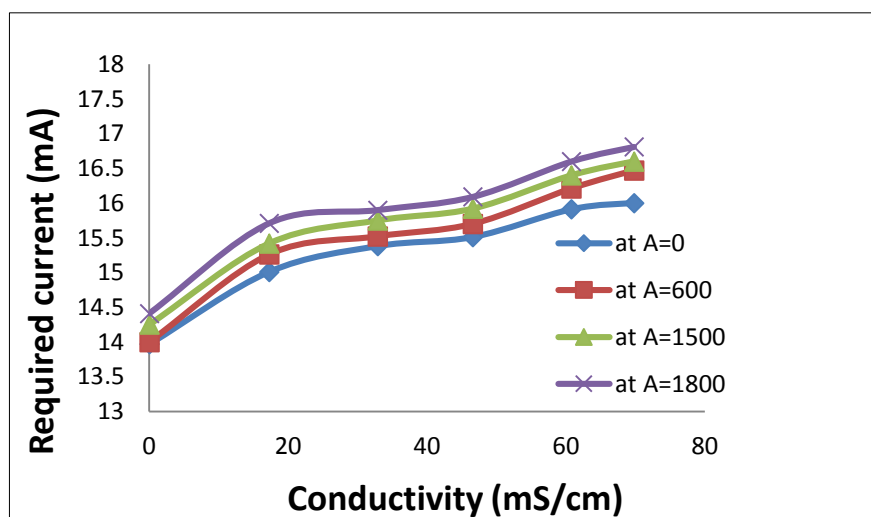


Fig. (3) CP current vs conductivity at 45 °C

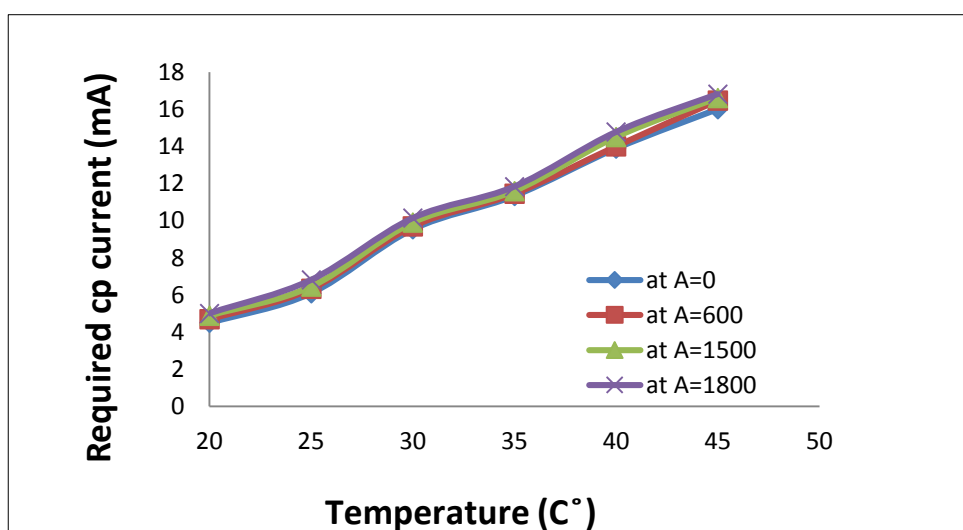


Fig.(4)CP current vs temperature at 0.025 (mS/cm) conductivity

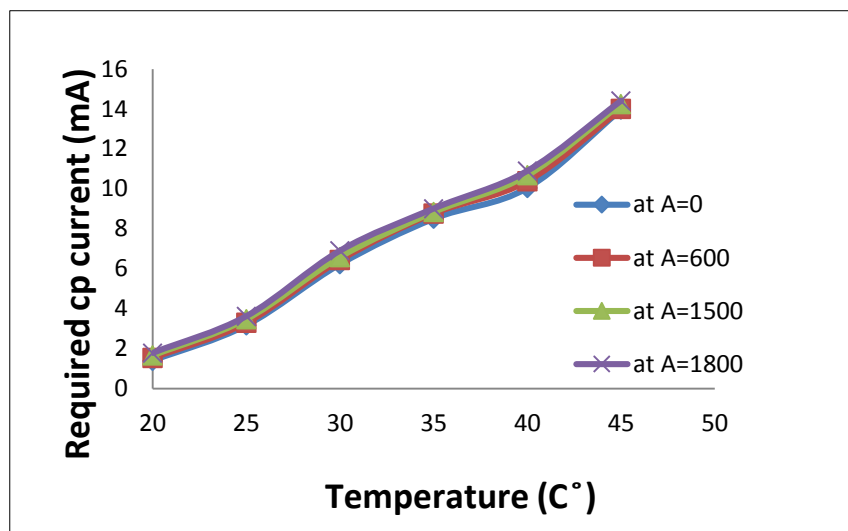


Fig.(5) CP current vs temperature at 69.8 (mS/cm) conductivity

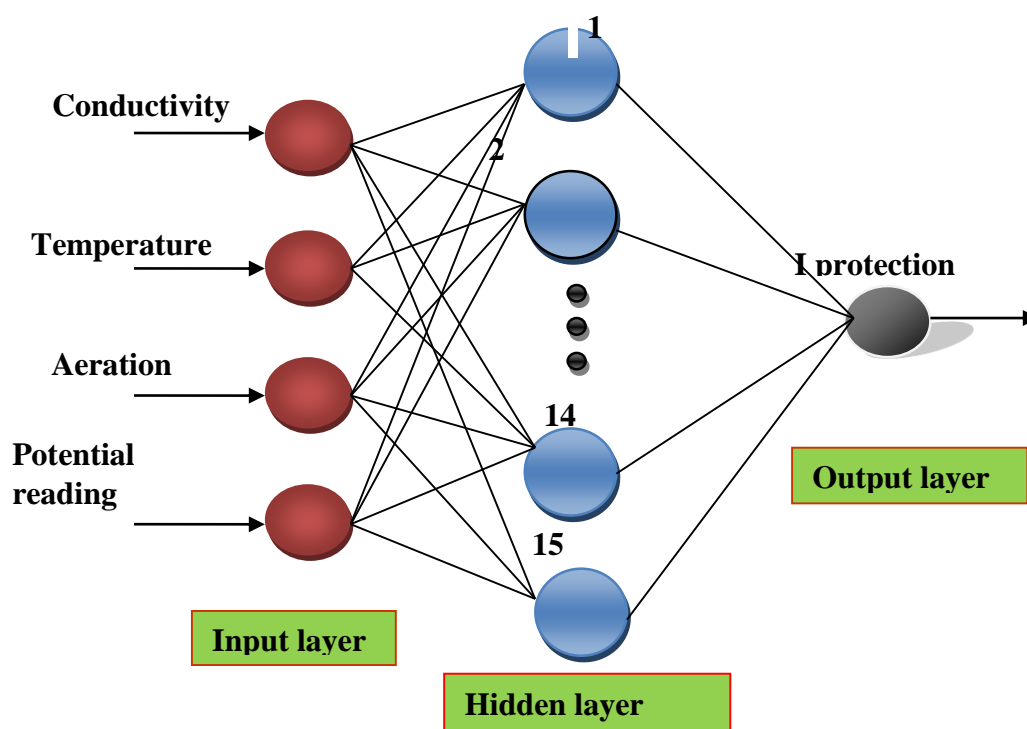
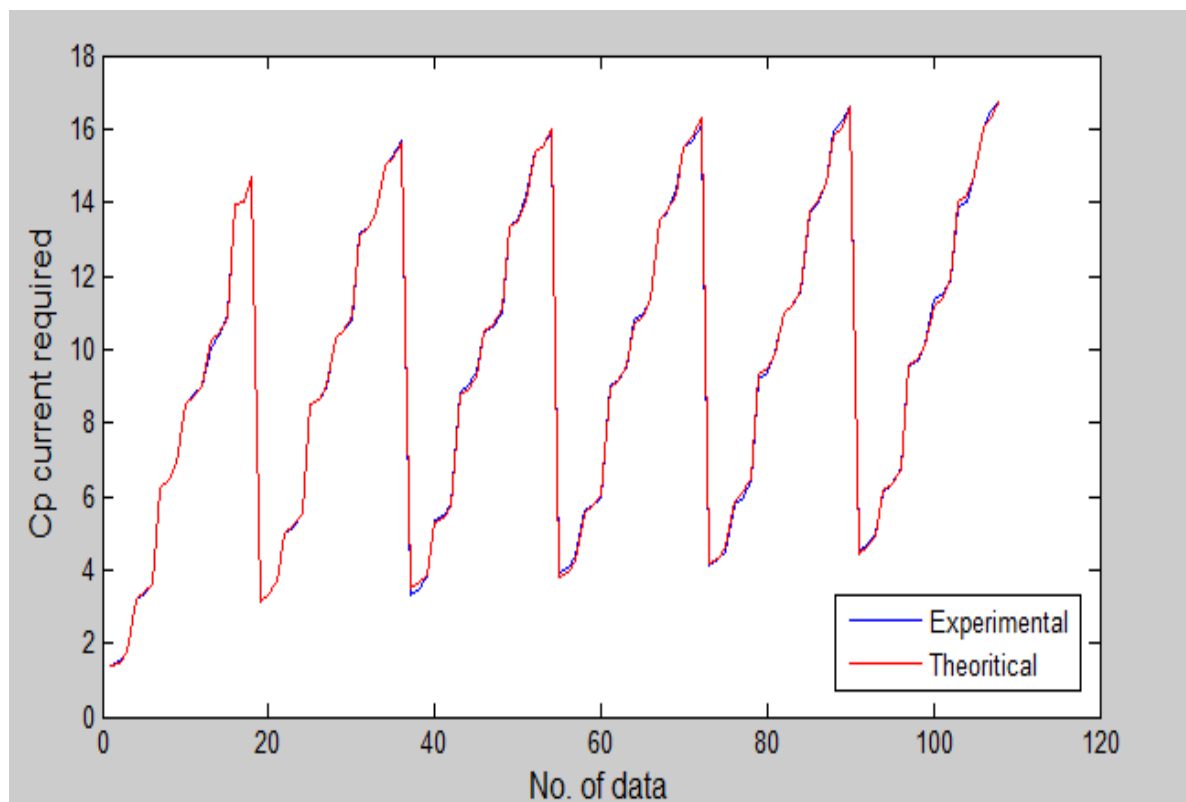
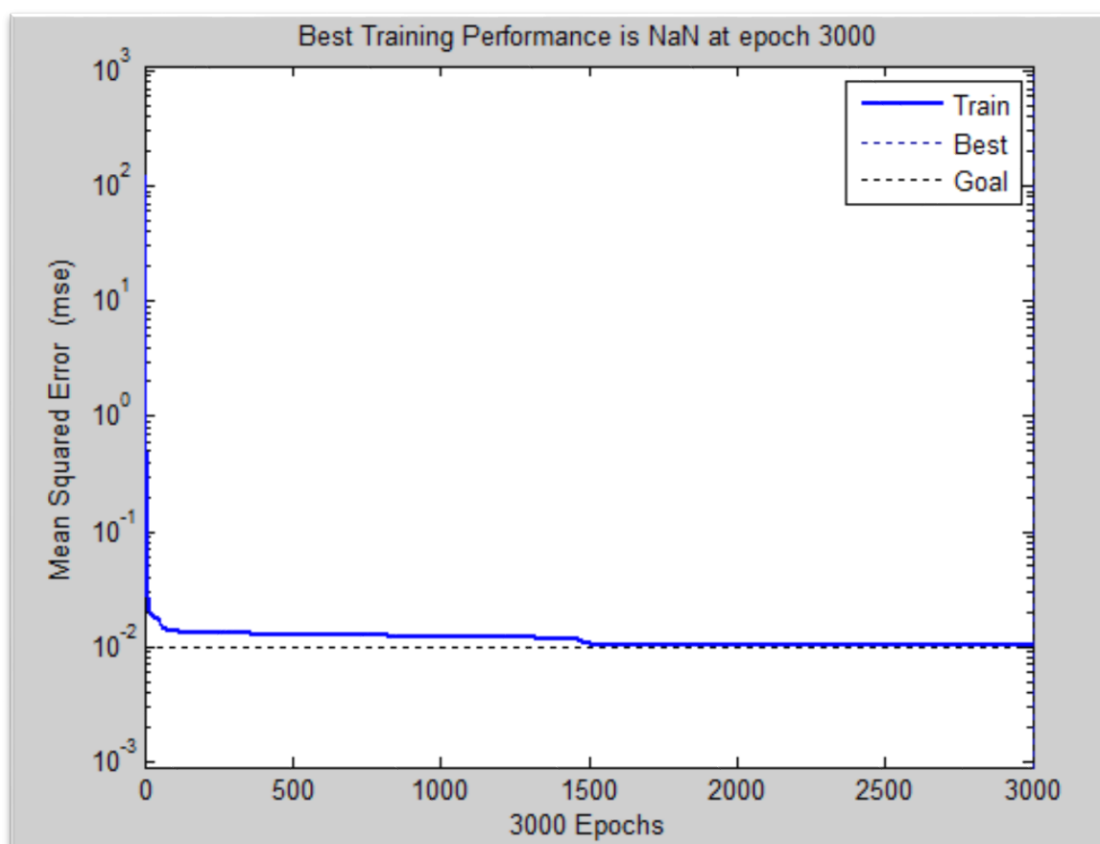


Fig.(6) Configuration of the proposed artificial neural network for CP System.



*Fig. (7) Identification of ICCP System*



*Fig.(8) Performance of the proposed artificial neural network*

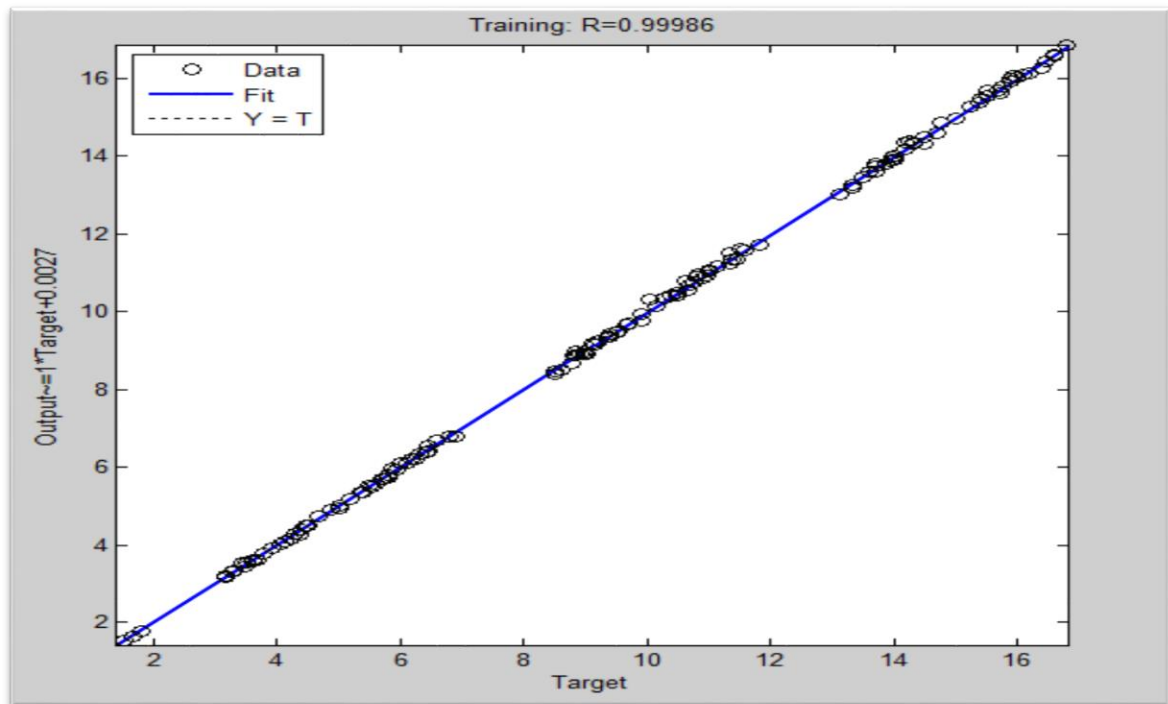


*Fig.(9) Correlation coefficient of the proposed artificial neural network*

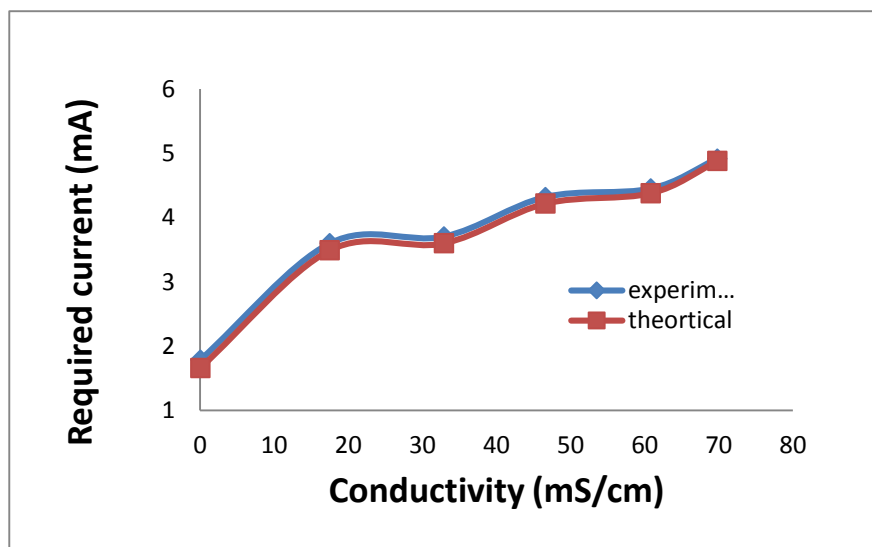


*Fig.(10) CP current vs conductivity at 20 °C for testing data*

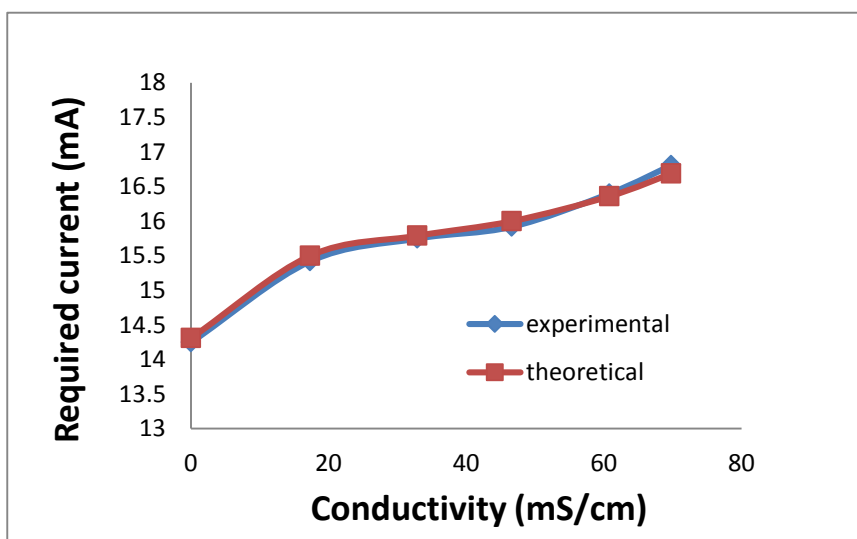


*Fig.(11) CP current vs conductivity at 45 °C for testing data*

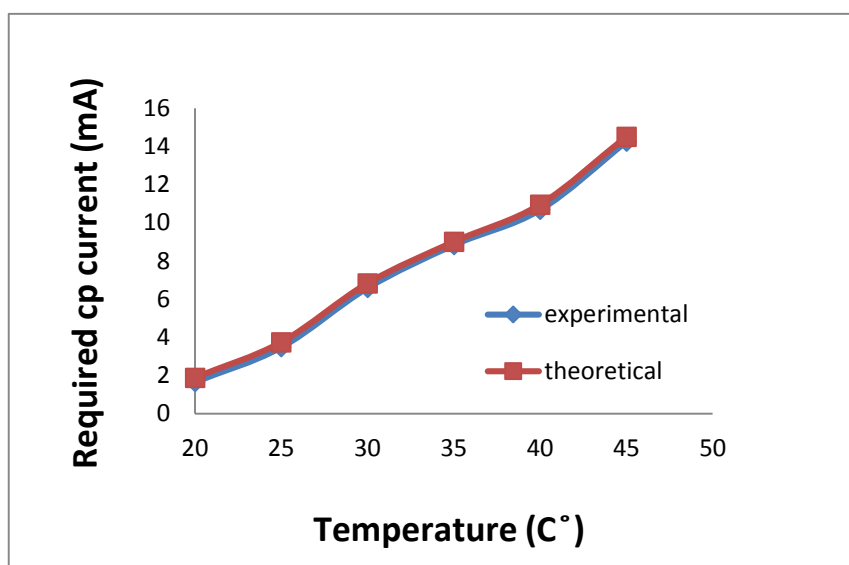


*Fig.(12) CP current vs temperature at 0.025(mS/cm) conductivity for testing data*

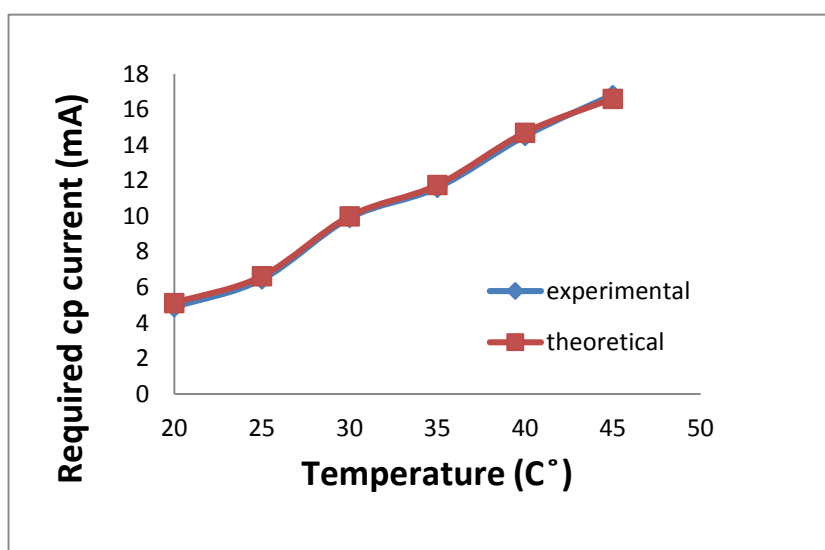


*Fig.(13) CP current vs temperature at 69.8(mS/cm) conductivity for testing data*

**CONCLUSION**

1. As the conductivity of the solution increased by increasing NaCl content, the current values required for protection increased.
2. As the solution temperature increased the protective current increased sharply.
3. Aeration factor increase the protective current slightly comparing with the effect of the other investigated Parameters, when the solution becomes saturated by oxygen, it reaches a steady state condition and the current did not changed.
4. The sequence effects of the studied parameters on the cathodic protection current can be arranged in the following order:

Temperature > concentration > aeration factor

5. An artificial neural network has proven to be efficient in identification of the impressed current cathodic protection system,
6. The neural network gives accurate results and is more flexible in terms that it can adapt itself with the change of the environment variable.

**REFERENCES**

- [1] Navfac mo-307; by Hamm. E. R., "Corrosion Control", Naval Facilities Engineering Command, Virginia, SN 0525-LP-542-3100, September, 1992.
- [2] Donald M. Waters, P.E., " Demy Stifying Cathodic Protection" , Steel Plate Fabricators Association, 2005. .
- [3] Samuel A. Bradford , Ph.D., p.Eng., "Corrosion Control" , ISBN 1-894038-58-4 , 2001.
- [4] Achebe C.H., Member, IAENG, U.C. Nneke, and O.E. Anisiji , " Analysis of Oil Pipeline Failures in the Oil and Gas Industries in the Niger Delta Area of Nigeria", ISBN 978-988-19251-9-0, 2012.
- [5] Vishal V. Ghai , " Knowledge Based Approach Using Neural Networks For Predicting Corrosion Rate", Master Thesis , Collage of Engineering and Technology of Ohio University, 2006.
- [6] Arthur K. Dunlop , James E. Donham, "ASM Handbook; Corrosion: of Petroleum Production Operation & Corrosion of Pipelines" , Volume 13, AS International, ISBN 0-87170-007-7, 1992.
- [7] Hongchen. F.: NACE CP Instructor, "Corrosion Control of Underground Pipelines", CorrStop, December, 2003.
- [8] Bayliss D. A. and D. H. Deacon, "Steelwork Corrosion Control", ISBN 0-203-30114-5, 2002. .
- [9] API Recommended Practice 1632, "Cathodic Protection of Underground Petroleum Storage Tanks and Piping Systems " , American Petroleum Institute , third edition, MAY, 1996.



- [10] Peabody A.W., "Peabody`s Control of Pipeline Corrosion", second edition, NACE International, ISBN 1-57590-092-0, 2001.
- [11] Mansi. R., " Cathodic protection of impressed current method for carbon steel in 3.5% NaCl solution", MSc. thesis, University of Technology, Chemical Engineering, 2007.
- [12] Abdulqader. A., "Studying Parameters of Cathodic Protection by Artificial Neural Network", MSc. thesis, University of Basrah, Mechanical Engineering, 2009.
- [13] Saleh. Sh.," Study The Effect of Some Variables on Cathodic Protection Current Density ", MSc. thesis, University of Technology, Chemical Engineering, Baghdad, June, 2005.
- [14] Jurgen Van Gorp, "Nonlinear Identification with Neural Network and Fuzzy Logic", Vrije University Brussel, April 2005.
- [15] Sath Yam Bonala , "Network Based System Identification with Application to Heating ,Ventilating and Air Conditioning(HVAC)System", MSc. Thesis ,M ay 2009
- [16] Laftah, R.M., "Buckling Behaviour of Stiffened Plate Panels Using Artificial Neural Networks", Ph.D Thesis, College of Engineering, University of Basrah, 2007.
- [17] Mohammad, H. M., "Prediction of Pitting Corrosion Fatigue Life for Carbon Steel Using Artificial Neural Networks", Ph.D. Thesis, Mechanical Engineering, Engineering College, Basrah University, 2010.
- [18] Howard Demuth, Mark Beale, " Neural Network Toolbox For Use with MATLAB", User`s Guide ,Version 4,2002.

## Study The Effect Of Water – Gas Shift Equilibrium on Adiabatic Flame Temperature for Alkanes Family Fuels at rich conditions

Tahseen Ali Gabbar  
Basrah Technical College, Iraq

### Abstract

The effect of water – gas shift equilibrium on adiabatic flame temperature for Alkanes family fuels was studied. The calculations of adiabatic flame temperatures were carried out by developing a program by using visual basic 6 language, based on a general algorithm meant to compute the equilibrium composition of products for any fuel–oxidizer gaseous mixture. The algorithm is based on the thermodynamic principles. Ten compounds were considered as products: the fuel ( $C_nH_{2n+2}$ ),  $CO_2$ ,  $CO$ ,  $H_2O$ ,  $N_2$ ,  $O_2$ ,  $CH_4$ ,  $C_2H_6$ ,  $C_3H_8$ ,  $C_4H_{10}$ ,  $H_2$ , their heat were capacities expressed as function of temperature with the form:  $C_p = a_0 + a_1T + a_2T^2 + a_3T^3$ . Two methods with and without water – gas shift equilibrium were used to analysis the products gases. The results showed, adiabatic flame temperature calculated with water – gas shift equilibrium greater than that calculated without water – gas shift equilibrium.

Keywords: Water – Gas shift Equilibrium, Adiabatic flame temperature, Flame & Combustion

### Introduction

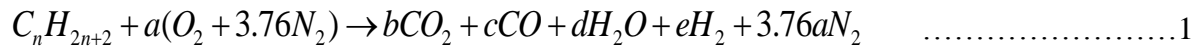
One of the most important features of a combustion process is the highest temperature of the combustion products that can be achieved. The temperature of the products will be greatest when there are no heat losses to the surrounding environment and all of the energy released from combustion is used to heat the products. If all the heat evolved in the reaction is employed solely to raise the product temperature, this temperature is called the adiabatic flame temperature. Because of the importance of the temperature and gas composition in combustion considerations, it is appropriate to review those aspects of the field of chemical thermodynamics that deal with these subjects.

Bhoia and Channiwala [1] are studied theoretical and experimental axial flame temperature distribution of producer gas fired premixed burner. Their experimental results showed that the maximum axial flame temperature distribution was achieved at A/F (air to fuel) ratio of 1 and the adiabatic flame temperature of 1653°C was calculated theoretically at A/F ratio of 1. Nurun Nabi [2] was carried out a theoretical investigation of engine thermal efficiency, adiabatic flame temperature,  $NO_x$  emission and combustion-related parameters for different oxygenated fuels. His results explained that with the increase in oxygen content in the fuels adiabatic flame temperature decreases linearly. Khalil and et al [3] were studied theoretically the effect of pressure and inlet velocity on the adiabatic flame temperature of a methane-air flame, the study was performed using Fluent software. The pressure was varied between 2 and 10 atmosphere, while the inlet velocity varied between 5 and 10 m/s. They were found in general the adiabatic flame temperature increase with pressure. Zhou and Donald [4] were studied a new method for adiabatic flame temperature estimations of hydrocarbon fuels. The investigation was conducted over a wide range of operating conditions in terms of fuel composition, pressure and temperature of reactants, fuel–air equivalence ratio and fuel vapor fraction and several neural network models for predicting the flame temperature for different applicable fuel ranges were built and examined. The neural network prediction results were compared with the calculated by a thermodynamic and chemical equilibrium-based computer code NASA program CET89. It was shown that trained neural network models can provide the adiabatic flame temperature prediction with a good level of accuracy over a wide range of operating conditions. Torii and et al [5] were studied theoretically study adiabatic flame temperature and specific heat of combustion gases for both hydrocarbon-air and alcohol-air mixtures by means of a method of chemical equilibrium calculation. It was found that the detailed properties of combustion gas compositions, to a certain degree, can be predicted by the approximated equations, which, based on the results of the chemical equilibrium calculations, which were produced with the aid of the method of least squares. Conroy and et

al [6] were examined the effects of flame temperature and the effect of assuming Lewis Number (ratio of mass to heat transport to the surface), is one.

### Theory

The combustion of an arbitrary hydrocarbon fuel (Alkanes fuels which has the form  $C_nH_{n+2}$ ), for rich combustion, can be represented as [7]:



Since the coefficient ( $a$ ) represent the ratio of the number of moles of  $O_2$  in the reactants to the number of moles of fuel, then, the equivalence ratio can relate as:

$$\Phi = \frac{1.5n + 0.5}{a} \quad \dots\dots\dots 2$$

where  $n$ : number carbon atoms in fuel

The reaction in equation (1) which has four unknown variables ( $b$ ,  $c$ ,  $d$  and  $e$ ), but from the material balance three equations can be written (carbon, hydrogen and oxygen balance). Then, two methods will be used in this paper to solve equation (1).

### Method 1 (with water – gas shift equilibrium occurs)

The water gas shift equilibrium occurs as the reversible reaction below:



The water-gas shift equilibrium constant can be written as [7,8],

$$K_p = \frac{b.e}{c.d} \quad \dots\dots\dots 4$$

Solving the element balance in terms of the unknown coefficient  $b$  results,

$$c = n - b \quad \dots\dots\dots 5$$

$$d = 2a - b - n \quad \dots\dots\dots 6$$

$$e = -2a + b + 2n + 1 \quad \dots\dots\dots 7$$

Substituting equations (5,6 and 7) into equation (4) yields a quadratic equation in  $b$ , the solution of which is

$$b = \frac{2a(K_p - 1) + 2n + 1}{2(K_p - 1)} - \frac{1}{2(K_p - 1)} \left[ (2a(K_p - 1) + 2n + 1)^2 - 4K_p(K_p - 1)(2an - n^2) \right]^{1/2} \quad \dots\dots\dots 8$$

The water – gas shaft is a function of temperature, Bustamante and Enick [7,10] were set the water – gas constant as :

$$K_p = \exp\left(-4.33 + \frac{4577.8}{T}\right) \quad \dots\dots\dots 9$$

### Method2 (without water – gas shift equilibrium occurs)

If the water gas shift equilibrium not occurs, the hydrogen gas not created in products (i.e  $e=0$ ). That leaves three unknowns ( $b$ ,  $c$ , and  $d$ ). To solve these, three element balances were employed (C, H, and O) as:

$$d = n + 1 \quad \dots\dots\dots 10$$

$$b = \frac{2(1.5n + 0.5)}{\Phi} - (2n + 1) \quad \dots\dots\dots 11$$

$$c = n - b \quad \dots\dots\dots 12$$

### Adiabatic flame temperature

The adiabatic flame temperature can be determined by using the conservation of mass and conservation of energy principles. To illustrate the procedure, suppose that the combustion air and the combustion products for each form of ideal gas mixtures. Then, the energy rate balance on a per mole of fuel basis, is [7]:

$$\sum_P n_i h_i = \sum_R n_i h_i \quad \dots\dots\dots 13$$

where  $i$  denotes the incoming species.

The enthalpy to be formed from two parts : sensible and chemical parte as:

$$h_i = \int_{T_o}^T C_{p_i} dT + \Delta h_{f,i}^o \quad \dots\dots\dots 14$$

Substituting equation (14) in to equation (13) yield,

$$\sum_P \left( \int_{T_o}^T C_{p_i} dT + \Delta h_{f,i}^o \right) = \sum_R \left( \int_{T_o}^T C_{p_i} dT + \Delta h_{f,i}^o \right) \quad \dots\dots\dots 15$$

Rewrite equation (15), then

$$\sum_P \left( \int_{T_o}^T C_{p_i} dT \right) = \sum_R \left( \int_{T_o}^T C_{p_i} dT \right) + \left( \sum_R \Delta h_{f,i}^o - \sum_P \Delta h_{f,i}^o \right) \quad \dots\dots\dots 16$$

The second term in the right hand of equation (16) represents heat of combustion and written as

$$Q = \left( \sum_R \Delta h_{f,i}^o - \sum_P \Delta h_{f,i}^o \right) \quad \dots\dots\dots 17$$

Integrating the right hand of equation (16) from original temperature to initial temperature ( $T_i$ ) ( $T_o=298K$ ), Therefore the first term in right hand of equation (16) will be zero and the left hand integrated from original temperature to adiabatic flam temperature ( $T_a$ ), then

$$\sum_P \left( \int_{T_o}^{T_a} C_{p_i} dT \right) = Q \quad \dots\dots\dots 18$$

The specific heat ( $C_p$ ) can be calculation from the equation:

$$C_{p_i}(T) = a_o + a_1 T + a_2 T^2 + a_3 T^3 \quad \dots\dots\dots 19$$

Where  $a_o$ ,  $a_1$ ,  $a_2$  and  $a_3$  are the specific heat coefficients, it values shown in appendix A

Substituting equation (19) in equation (18) and integrated, then

$$\sum_P \left( a_o T_a + \frac{a_1 T_a^2}{2} + \frac{a_2 T_a^3}{3} + \frac{a_3 T_a^4}{4} \right) = \left\{ \begin{array}{l} Q + \sum_P \left( a_o T_o + \frac{a_1 T_o^2}{2} + \frac{a_2 T_o^3}{3} + \frac{a_3 T_o^4}{4} \right) \end{array} \right\} \quad \dots\dots\dots 20$$

This equation solved by Newton-Raphson Method.

## Results

In combustion problems the adiabatic flame temperature depend on the heat of combustion. Also, both the heat of combustion and adiabatic flame temperature depends on the analysis of products gases. Therefore the analysis of products gases will be discussed first.

Figures (1 to 4) show the products analysis for methane, ethane, propane and butane fuel with change of equivalence ratio. The mole fraction of carbon monoxide and carbon dioxide were the same behavior for both methods, where mole fraction of carbon dioxide decreasing with increasing equivalence ratio as shown in figure (1) due to decreasing the number moles of air when the equivalence ratio increasing. This can be shown by equation (2), where reversible relationship between equivalence ratio and number moles of air (coefficient  $a$ ). Also, in figure (1), can be noted, by usng method2, the mole fraction of ( $CO_2$ ), (coefficient  $b$  was given by equation 11), will be equal zero if the equivalence ratio takes the following values: for

methane, ethane, propane and butane as  $\frac{4}{3}$ ,  $\frac{7}{5}$ ,  $\frac{10}{7}$  and  $\frac{13}{9}$  respectively, this is a limitation of method2.

The mole fraction of CO, in both methods, increased with the equivalence ratio increased as shown in figure (2), due to decreasing the number moles of oxidizer as above.

In figure (3) it can be shown that the mole fraction of water vapor by method1 decreasing with increasing equivalence ratio due to created hydrogen gas in products as a result of water gas shift equilibrium occurs, while using method2 it increased with increasing equivalence ratio due to decreasing total number moles of mixture for the products as a results of equivalence ratio increasing. In figure (4) the mole fraction of  $H_2$  was increased with the equivalence ratio increasing because of the mole fraction of CO will increase too, as shown in figure (2). The reaction specified in equation (3) will be move to use the right hand to increase the moles of  $CO_2$  and  $H_2$ .

Figure (5) shows the mole fraction of nitrogen decreasing with equivalence ratio increasing due to increasing moles of air according to equation2. Also, in this figure it can be noted that the higher nitrogen mole fraction is for butane compared with propane, ethane and methane respectively because of number moles of air for butane is greater than for propane, ethane and methane respectively when equivalence ratio remain constant.

Figure (6) shows the heat of combustion varies with equivalence ratio. From this figure it can be noted that the heat combustion for butane is the greater than propane, ethane and methane because of the heat formation of butane is greater than heat formation for other fuels. Also, this figure shows with increasing equivalence ratio the heat of combustion decreasing. This phenomena can be explained as:

In figure (7) increasing mole fraction of  $CO_2$  the heat of combustion will increase due to increasing enthalpy of products which is given by equation (17), but mole fraction of  $CO_2$  decreasing with increasing equivalence ratio as shown in figures (1), since heat of combustion decreased with equivalence ratio increasing. In figure (8) heat of combustion decreased when increasing mole fraction of CO, but mole fraction of CO increased when equivalence ratio increased as shown in figures (2). Therefore heat of combustion will be decreased when equivalence ratio increasing. Figure (9) shows the heat of combustion increasing when the mole fraction of water vapor increased for method2, but mole fraction of  $H_2O$  was decreased if equivalence ratio was increased as shown in figure(3), therefore heat of combustion decreasing. For method1 the same behave can be shown for water vapor with heat of combustion, where from figure(3) by method2 noted the water vapor at first slowly increasing then decreasing after the value of equivalence ratio reached greater than 1.15 for all fuels, since the behave of heat of combustion become as shown in this figure (9) for method2. Figure (10) show the heat of combustion decreased if the mole fraction of hydrogen was increasing for method1 only. But mole fraction of hydrogen was increased when the equivalence ratio increased as shown in figures (1 to 4). All results explained in figures (6, 7, 8 and 9) show that the heat of combustion will be decreased if the equivalence ratio increasing.

Figure (11) explained the relationship between adiabatic flame temperature with equivalence ratio. In this figure can be noted when increasing equivalence ratio the adiabatic flame temperature will be decreased due to decreasing heat of combustion. In this figure, the results show the adiabatic flame temperature for Propane and Butane are closed equally along the suing equivalence ratio although heat of combustion for Butane greater than Propane. This phenomena can be explanation due to increasing mole fraction of Nitrogen in products as a results of increasing the number of Carbone atom in form of fuel as shown in figure5, when equivalence ratio is constant. In adiabatic combustion, as in this research, the heat of combustion will be caused increasing of products temperature only. Mass of Nitrogen in products will be heated from initial temperature to products temperature, sine much of heat of combustion losses to heated Nitrogen. Therefor adiabatic flame temperature reduces if mass of Nitrogen increased. But Nitrogen mole fraction for Butane greater than for Propane (as in

figure 5), therefor, adiabatic flame temperature for Butane reduced and closed equally adiabatic flame temperature for Propane although heat of combustion for Butane greater than heat of combustion for Propane. This phenomena can be shown if drawing the relationship between adiabatic flame temperature ( $T_a$ ) and heat of combustion ( $Q$ ) after dividing each of them by number moles of Nitrogen in products. This is will be shown in figure (16). Where in figure (16) the bigger of this relationship was for Methane, Ethane, Propane and Butane due to increasing mole fraction of Nitrogen respectively.

Figures (12 and 14) shows the adiabatic flame temperature increasing when the mole fraction of  $\text{CO}_2$  and  $\text{H}_2\text{O}$  increasing too, but all results in figures (1 and 3) shows decreasing mole fractions of  $\text{CO}_2$  and  $\text{H}_2\text{O}$  if the equivalence ratio increasing therefore adiabatic flame temperature will be decreasing. In other hand, results in figures ( 13 and 15) show with increasing mole fraction of  $\text{CO}$  and  $\text{H}_2$ , the adiabatic flame temperature decreasing. The mole fraction of  $\text{CO}$  and  $\text{H}_2$  were increasing when equivalence ratio increasing too, therefore the adiabatic flame temperature will be decreasing.

In figure (17) can be noted, the adiabatic flame temperature calculated, for all fuels, by method1 was greater than that calculated by method2 due to reducing, by method1, mole fraction of  $\text{CO}$  in products as a results of water gas shift equilibrium occurs as shown in figure 2.

### Conclusions

The present theoretical investigation shows the significant effect the water – gas shift equilibrium on adiabatic flame temperature. From the obtained results and discussion the following conclusions can be drawn:-

1. The water – gas shift equilibrium increased adiabatic flame temperature.
2. There are solving limitations without water – gas shift equilibrium represent by cutting analysis if the equivalence ratio riches the values  $\frac{4}{3}$ ,  $\frac{7}{5}$ ,  $\frac{10}{7}$  and  $\frac{13}{9}$  for Methane, Ethane, Propane and Butane fuel respectively.

### References

- [1] **P.R. Bhoia and S.A. Channiwala** " Emission characteristics and axial flame temperature distribution of producer gas fired premixed burner" biomass and bioenergy 33, 469–477 (2009).
- [2] **Md. Nurun Nabi** " Theoretical investigation of engine thermal efficiency, adiabatic flame temperature,  $\text{NO}_x$  emission and combustion-related parameters for different oxygenated fuels" Applied Thermal Engineering 30 (2010) 839–844.
- [3] **Rana Haj Khalil, Ahmad Sakhrieh, Mohammad Hamdan, and Jamil Asfar** " Effect of Pressure and Inlet Velocity on the Adiabatic Flame Temperature of a Methane-Air Flame" Jordan Journal of Mechanical and Industrial Engineering, Volume 4, Number 1, Jan. 2010, ISSN 1995-6665, Pages 21 - 28.
- [4] **Minyong Zhou and J.E. Donald Gauthier** "A new method for adiabatic flame temperature estimations of hydrocarbon fuels" Fuel 78 (1999) 471–478.
- [5] **Shuichi Torii, Toshiaki Yano, and Yukio Tunoda** "Adiabatic Flame Temperature and Specific Heat of Combustion Gases" TORII, Shuichi; YANO, Toshiaki; TSUNODA, Y, Citation 34: 1-15, Issue Date 1992-09
- [6] **Paul J. Conroy, Paul Weinacht, and Michael J. Nusca** " Parametric Erosion Investigation (Propellant Adiabatic Flame Temperature)" Army Research Laboratory Aberdeen Proving Ground, MD 21005-5066



- [7] **S. R. Turns** "An introduction to combustion concepts and applications" second edition, McGraw-Hill Higher Education
- [8] **I. A. Yetter** "Combustion" 4<sup>th</sup> edition(2008).
- [9] **F. A. Williams** "Combustion Theory" second edition. Princeton University (1985).
- [10] **C.K. Law, A. Makino and T.F. Lu** "On the off-stoichiometric peaking of adiabatic flame temperature" Combustion and Flame Vol.145 ,p.p 808–819(2006),

### NOMENCLATURE

Symbol	Definition	SI Units
<b>English Symbols</b>		
$a$	Number moles of air	Mole
$b$	Number moles of CO <sub>2</sub>	Mole
$c$	Number moles of CO	Mole
$d$	Number moles of H <sub>2</sub>	Mole
$c_p$	Specific heat	KJ/mol. K
$d$	Number moles of H <sub>2</sub> O	Mole
$h_i$	Total enthalpy of species i	KJ/mol. K
$K_p$	Water – gas shift equilibrium constant	-
$n$	Number of carbon atoms in fuel form	-
$n_i$	Number moles of species i	mole
$Q$	Heat of combustion	KJ/mole of fuel
$T$	Temperature	K
$T_a$	Adiabatic flame temperature	K
$T_i$	Initial temperature	K
$T_o$	Original Temperature	K
$\Delta h_i$	Heat formations of species i	KJ/mol.
<b>Greek Symbols</b>		
$\Phi$	Equivalence ratio	-
<b>Subscript</b>		
$i$	Species $i$	
$a$	Adiabatic condition	

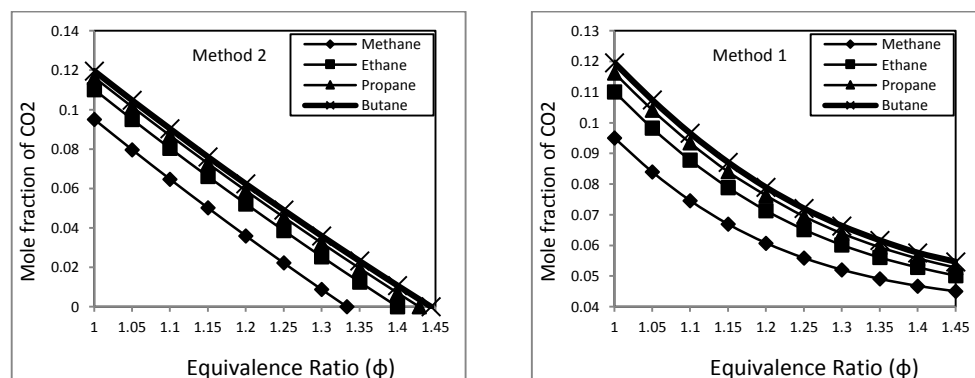


Figure (1) change mole fraction of CO<sub>2</sub> with equivalence ratio

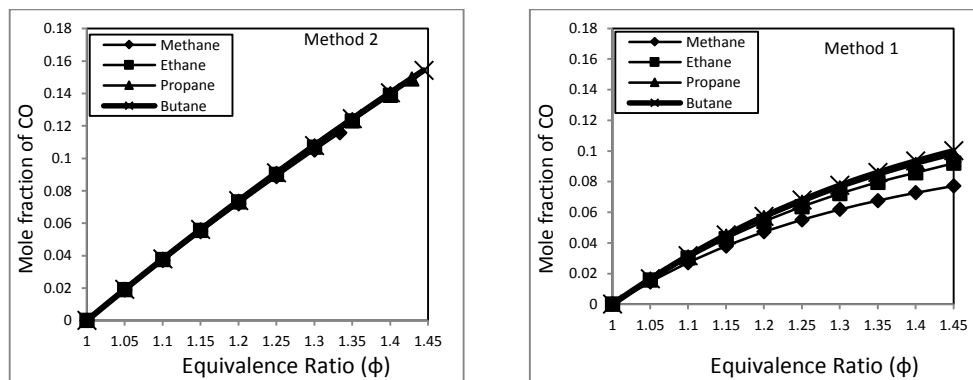
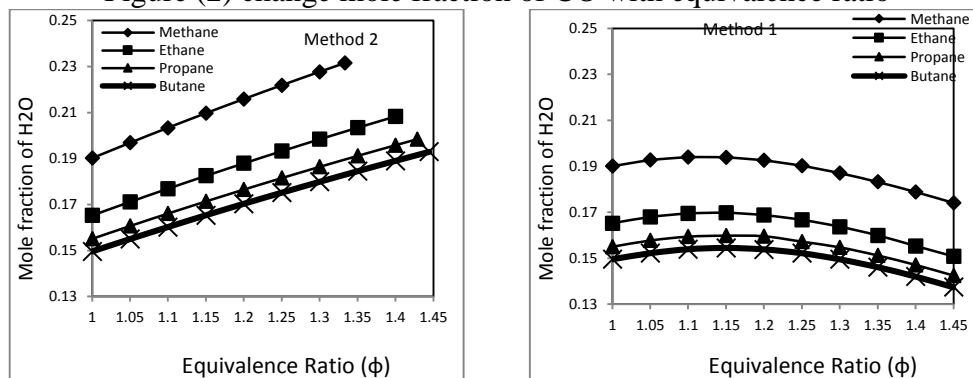
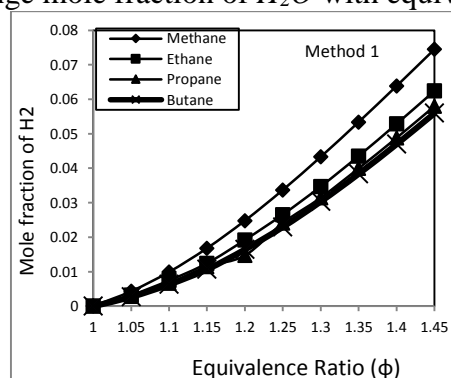
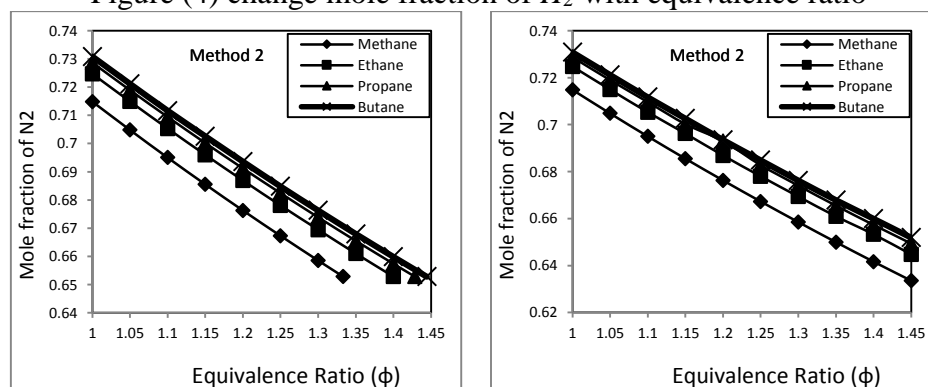


Figure (2) change mole fraction of CO with equivalence ratio


 Figure (3) change mole fraction of  $H_2O$  with equivalence ratio

 Figure (4) change mole fraction of  $H_2$  with equivalence ratio

 Figure (5) change mole fraction of  $N_2$  with equivalence ratio



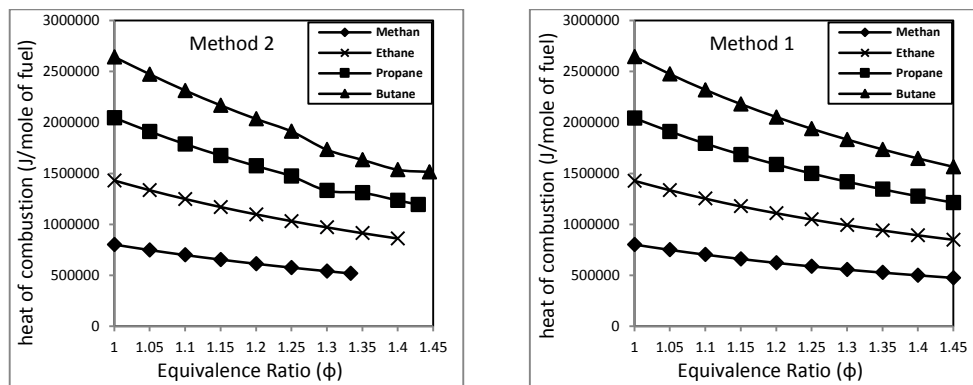
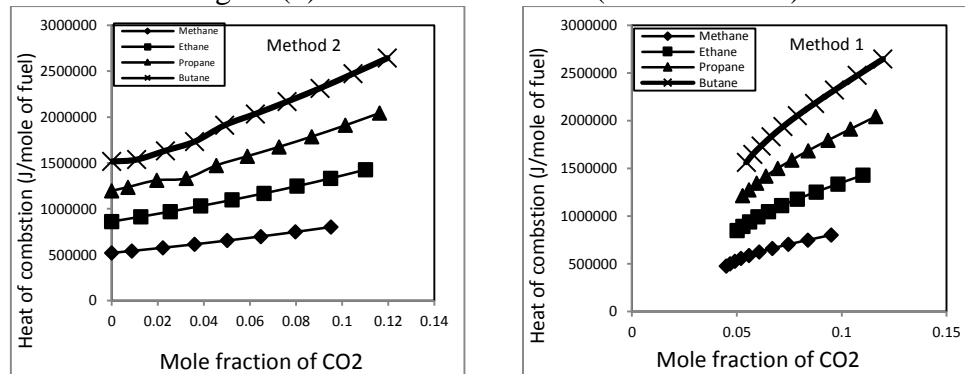
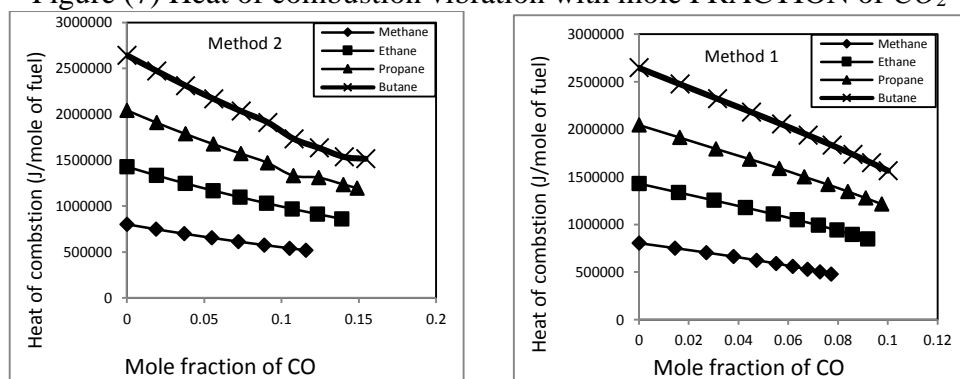
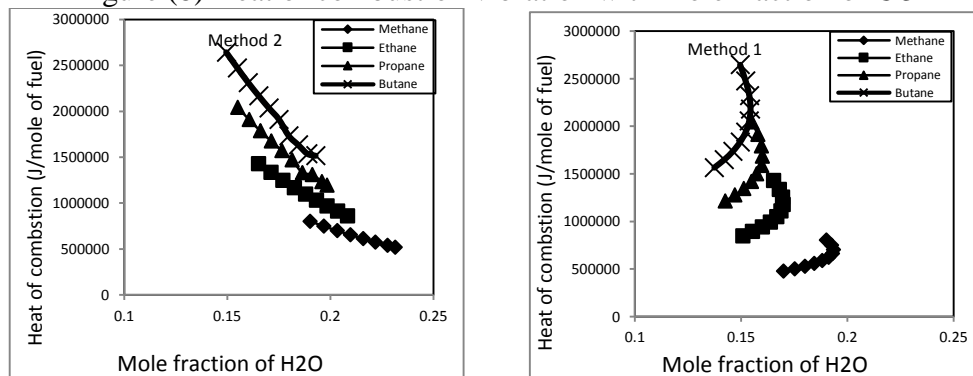


Figure (6) Heat of combustion (J/mole of fuel)

Figure (7) Heat of combustion vibration with mole FRACTION of  $\text{CO}_2$ Figure (8) Heat of combustion vibration with mole fraction of  $\text{CO}$ Figure (9) Heat of combustion variation with mole fraction of  $\text{H}_2\text{O}$

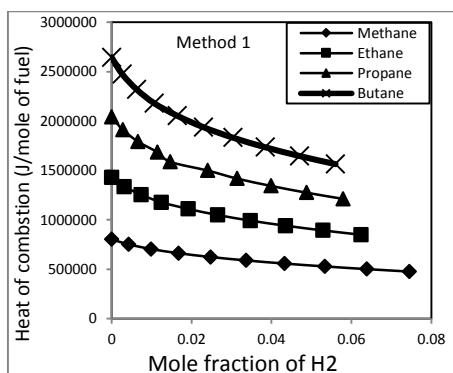
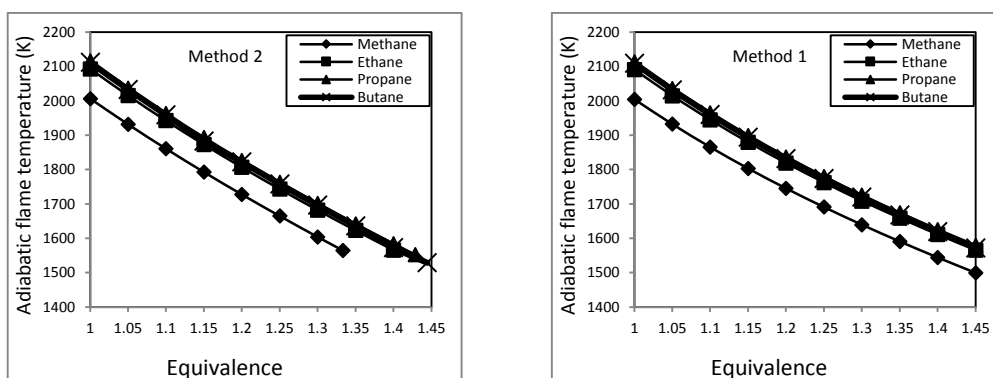

 Figure (10) Heat of combustion vibration with mole fraction of  $H_2$ 


Figure (11) Adiabatic flame temperature (K)

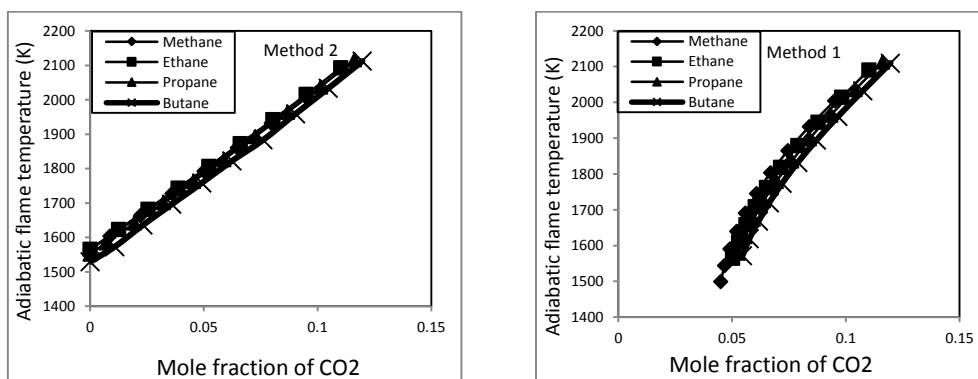


Figure (12) Adiabatic flame temperature (K)

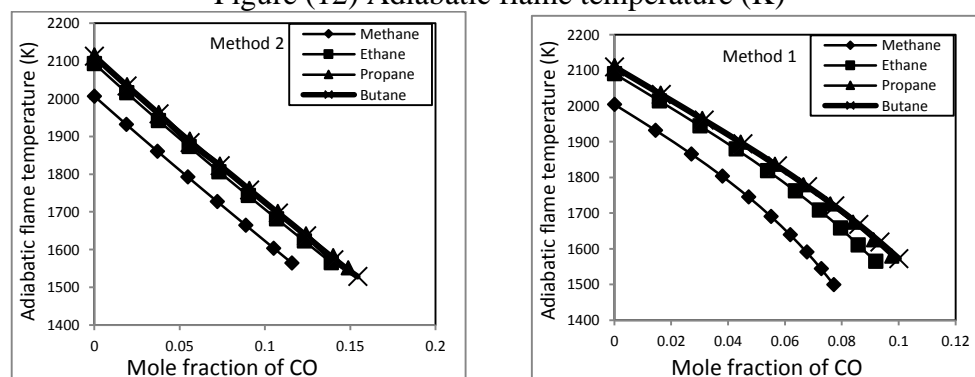


Figure (13) Adiabatic flame temperature (K)

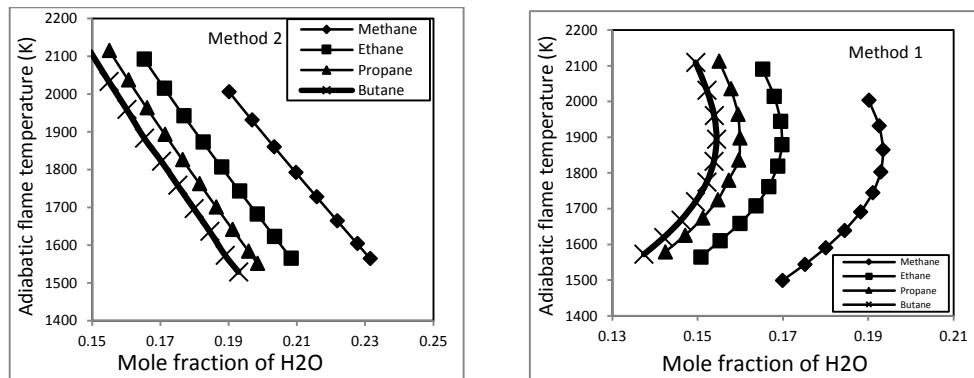


Figure (14) Adiabatic flame temperature (K)

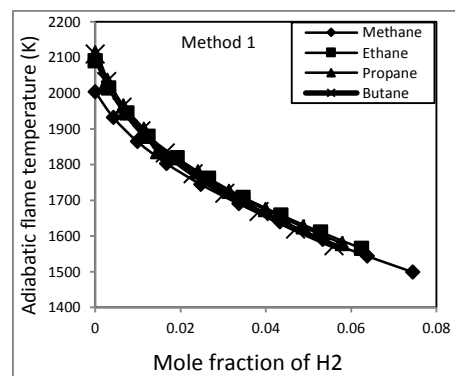


Figure (15) Adiabatic flame temperature (K)

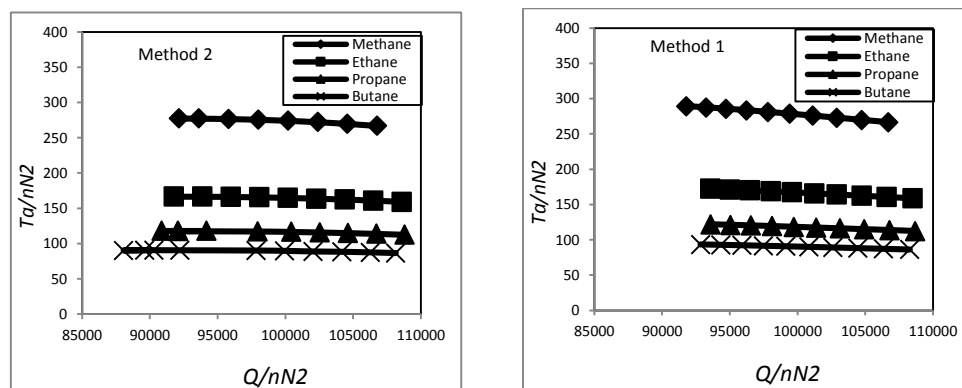
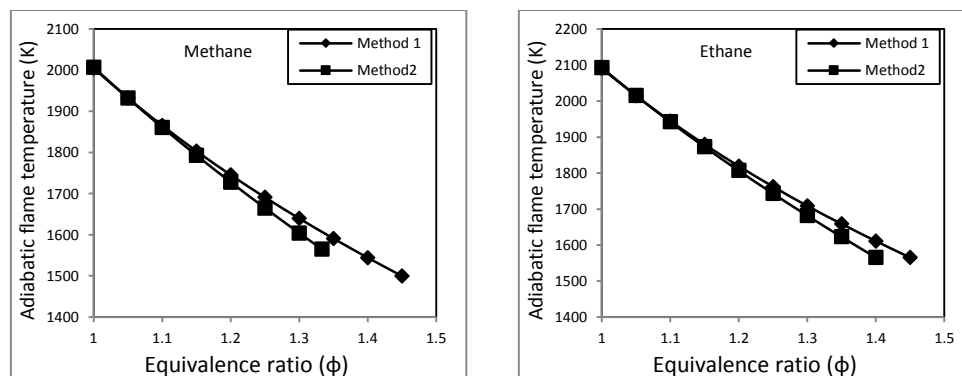


Figure (16)



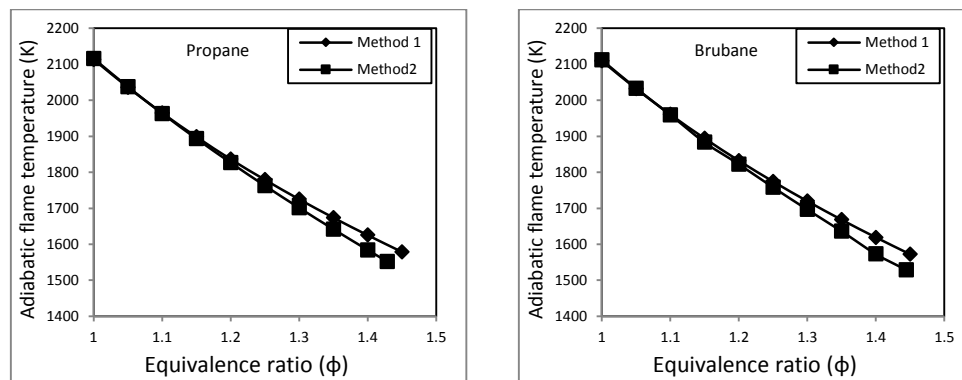


Figure (17) Various of Adiabatic flame temperature with equivalence ratio for all fuels  
**Appendix A** : the specific heat coefficient and heat formations for species

Formula	Name	$a_0$ J/mol K	$a_1$ J/mol K <sup>2</sup>	$a_2$ J/mol K <sup>3</sup>	$a_3$ J/mol K <sup>4</sup>
$N_2$	Nitrogen	3.115E+01	-1.357E-02	2.608E-05	-1.168E-08
$O_2$	Oxygen	2.811E+01	-3.680E-06	1.746E-05	-1.065E-08
$H_2$	Hydrogen	2.714E+01	9.274E-03	-1.381E-05	7.645E-09
CO	Carbon monoxide	3.087E+01	-1.283E-02	2.789E-05	-1.272E-08
$CO_2$	Carbon dioxide	1.980E+01	7.344E-02	-5.602E-05	1.715E-08
$CH_4$	Methane	1.925E+01	5.213E-02	1.197E-05	-1.132E-08
$C_2H_6$	Ethane	5.409E+00	1.781E-01	-6.938E-05	8.713E-09
$C_3H_8$	Propane	-4.224E+00	3.063E-01	-1.586E-04	3.215E-08
$C_4H_{10}$	Isobutane	-1.390E+00	3.847E-01	-1.846E-04	2.895E-08

# Evaluation of Off-Grid PV-Battery Inverter System for Supporting Energy Sector in Iraq

Alaa Liaq Hashem

PhD, Department of Mechanical Engineering, College of Engineering, University of Al-Qadisyah,  
Al Diwaniyah, Iraq.  
Email address: alaaliag@yahoo.com

## Abstract

Electrical energy is one of the most important forms of energy that directly affects all parts of modern life. The global demand for electrical energy significantly connected with population growth. In Iraq, the power plants involved in the production of electric energy operates mainly on fossil fuels, the decreases in their efficiency resulted in a significant decreases in the amount of energy supplied in all the cities of Iraq. Currently, the production amount available from all operated stations (thermal, gas, hydro or diesel units) to the national grid reach 7.153 GW in 2013, while the total electrical power needs is estimated more than 13 GW with a shortage energy reach up to 50%. The renewable energy share only 8% from the total production and comes from the hydro power plants. The renewable energy sources generate electricity with inconsiderable contribution of carbon dioxide (CO<sub>2</sub>) or other greenhouse gases (GHG) to the environment. This paper investigates the impact of a system consisting of a photovoltaic (PV) modules, batteries and inverter on off grid energy production. The system was analysed using PVsyst software. Global meteorological database software called Meteonorm7 has been used to generate a climate file for Baghdad city (33.3°N and 44.4°E) as input data into PVsyst. The suggested hybrid system in the present investigation consists of a combination of PV panels supplemented with battery set and inverter. The simulation explores a mix of climate conditions and the system components characteristics such as modules power output (kWp) and batteries charging/discharging storage behaviour to match the user need. With monthly electrical energy demand of 17127 kWh/month, the investigation indicates that Baghdad's location characterized with considerable monthly average daily beam normal solar radiation intensity (4.23 kWh/m<sup>2</sup>), is a prospective candidate for deployment of PV power components. The study results show that for a microgeneration system composed of 1.8-kWp PV system together with three batteries storage with overall energy storage 3.6 kWh and an inverter system. The solar penetration cover 21% from the total proposed demand.

**Keywords:** PV, Battery, Solar energy, Microgeneration, Green building, Photovoltaic systems, PVsyst. Off-grid PV system.

## الخلاصة

الطاقة الكهربائية هي واحدة من أهم أشكال الطاقة التي تؤثر بشكل مباشر على جميع مناحي الحياة الحديثة. الطلب العالمي على الطاقة الكهربائية مرتبط بشكل كبير مع النمو السكاني. في العراق، محطات الطاقة العاملة في مجال إنتاج الطاقة الكهربائية تعمل بشكل أساسي على الوقود الأحفوري، أدت الانخفاضات في كفاءتها في انخفاض كبير في كمية الطاقة المتوفرة في كل مدن العراق. حالياً، فإن كمية الإنتاج المتاحة من تشغيل كل المحطات (الحرارية، الغازية، الطاقة المائية ووحدات الديزل) إلى الشبكة الوطنية تصل إلى ٧,١٥٣ GW في عام 2013، في حين يقدر إجمالي احتياجات الطاقة الكهربائية أكثر من ١٣ GW مع عجز في الطاقة يصل إلى ٥٠٪. حصة الطاقة المتجددة ٨٪ فقط من إجمالي الإنتاج، ويأتي من محطات الطاقة الكهرومائية. مصادر الطاقة المتجددة تولد الكهرباء مع مساهمة لا تذكر من ثاني أكسيد الكربون (CO<sub>2</sub>) أو غيره من الغازات الدفيئة (GHG) للبيئة. هذه الورقة تحقق في تأثير استخدام منظومة مؤلفة من وحدات الخلايا الضوئية (PV)، بطاريات وعاكس على إنتاج الطاقة خارج الشبكة. تم تحليل النظام باستخدام برنامج PVsyst. استخدم برنامج قواعد البيانات العالمية للأرصاد الجوية يدعى Meteonorm7 لإنشاء ملف المناخ لمدينة بغداد (٣٣,٣° N على ٤٤,٤° E) وإدخال البيانات إلى برنامج PVsyst. في النظام الهجين المقترحة في التحقيق الحالي، التحليل يستكشف تأثير مزيج من الظروف المناخية وخصائص مكونات النظام مثل إنتاج وحدات الطاقة (kWp) وسلوك تخزين وتفريغ البطاريات لتتناسب مع حاجة المستخدم. مع الطلب الشهري على الطاقة الكهربائية مقداره ١٧١٢٧ كيلو واط / شهر، يشير التحقيق إلى أن موقع بغداد يتمتع بكميات اشعاع متميزة للمتوسط الشهري للإشعاع اليومي العمودي بكثافة (٤,٢٣ كيلو واط ساعة / م<sup>2</sup>)، وهو مرشح محتمل لنشر مكونات الخلايا الضوئية PV. أظهرت نتائج الدراسة أن نظام (microgeneration) تتألف من 1.8-kWp PV جنباً إلى جنب مع ثلاث بطاريات لتخزين الطاقة مقداره ٣,٦ كيلو واط وعاكس، تكون الطاقة الشمسية ٢١٪ من إجمالي الطلب المقترح.

## 1. Introduction

Electrical energy is one of the most important forms of energy that directly affect all parts of modern life. The global demand for electrical energy significantly connected with population growth. The electrical energy consumed worldwide rated up to 18.1% in 2012 from the fuel shares of the total energy final consumption, while fuel consumption used in electricity production reached to 22.3% of total fuel consumption, [1]. In Iraq, the power plants involved in the production of electric energy operates mainly on fossil fuels, the decreases in their efficiency resulted in a significant decreases in the amount of energy supplied in all the cities of Iraq. Currently, the production amount available from all operated stations (thermal, gas, hydro or diesel units) to the national grid reach 7.153 GW in 2013, while the total electrical power needs is estimated more than 13 GW with a shortage energy reach up to 50%, [2]. The renewable energy share only 8% from the total production from the hydro power plants. The rapid population growth make the buildings sector the largest consumer of electric power produced. The reduction in the consumption within the buildings sector through the integration of renewable energy systems that adopted in many countries of the world to provide a portion of the electrical energy of the building. Currently, countries such as USA,

UK and Germany installing renewable systems within buildings and modify their buildings code regulations (e.g. feed in tariff) to manage and encourage the deployment of renewable energy systems, [3]. In terms of its environmental benefits, power generation from renewable energy components become a very important. The renewable energy sources generate electricity with insignificant contribution of carbon dioxide (CO<sub>2</sub>) or other greenhouse gases (GHG) to the environment, they produce no pollutant discharge, [4]. Weather conditions govern the availability of solar energy at a given location. Baghdad city is the capital of the Iraq Republic. Iraq receives more than 3000 hours of solar radiance per year in Baghdad alone, [5]. This investigation for demonstrate the impact of install microgeneration system from photovoltaic (PV)-Battery and inverter components within domestic buildings in Baghdad city with off-grid scenario on the energy consumption from the grid and the solar energy fraction.

## 1.2 Background information

A wide set of tools exists for the test and design of both on-grid and off-grid connected photovoltaic systems, [6]. PV systems designers and users searching for accurate tool for characterizing, sizing, optimization and simulation the PV system. The PVsyst is a personal computer software package for the study, research, sizing and data analysis of complete PV systems. It deals with grid-connected, stand-alone, pumping and DC-grid (public transport) PV systems, and includes extensive meteo and PV systems components databases, as well as general solar energy tools, [7]. This paper investigate the impact of PV penetration and battery storage on off grid energy production. The proposed system using PVsyst software for energy and data analysis. A global meteorological database software called Meteonorm 7 used to generate a climate file for Baghdad city (33.3°N and 44.4°E) as input data into PVsyst software, [8].



## 2. Solar Radiation Data and Hybrid System

Using Meteonorm 7 climate data to generate a climate database for long period 1991-2010. The climate data sets interpolated from the satellite data for nearest climate stations from Baghdad city location. The Fig (1), Fig (2), Fig (3) and Fig (4) shows the dry air temperature in degree-centigrade (higher and lower limits), the global and diffuse radiation in kWh/m<sup>2</sup>, sunshine duration in hour, and wind velocity in m/s respectively. PV modules with the specific characteristics shown in Table (1), each panel provide 20 volts and 90 Wp.



Fig (1): Daily maximum and minimum

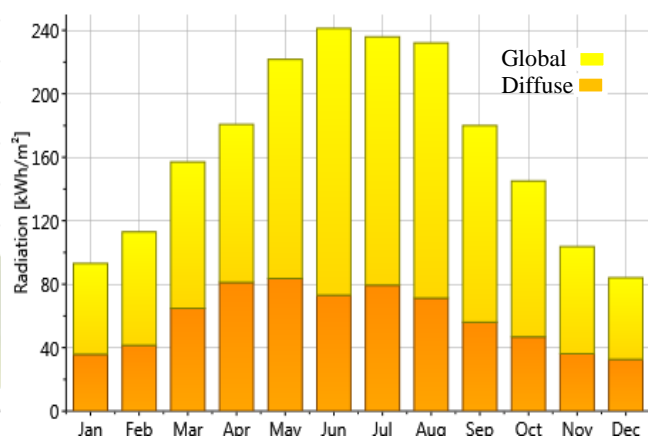


Fig (2): Diffuse and global solar

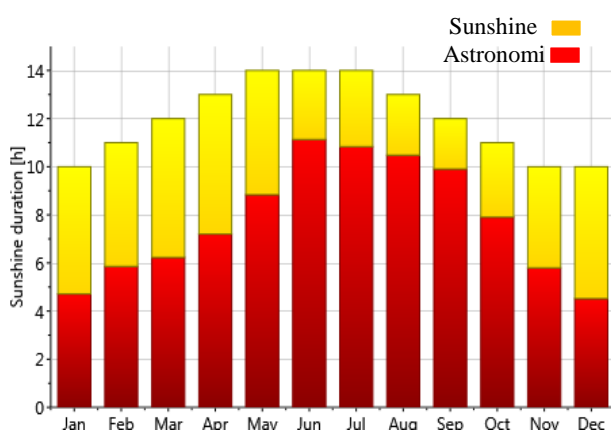


Fig (3): Sunshine and astronomical sunshine

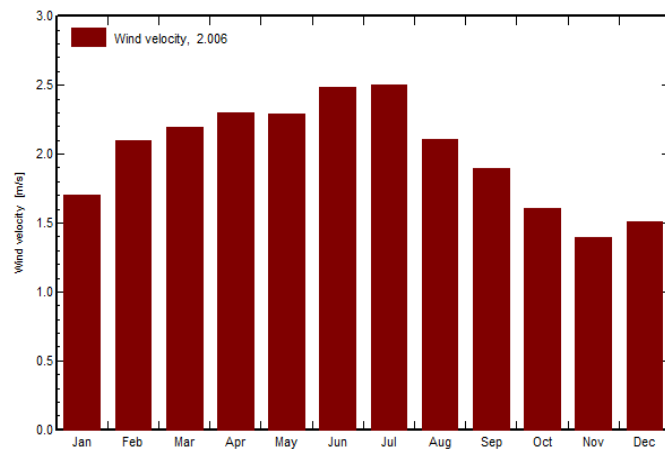


Fig (4): Wind

The total number of PV modules equal to 20, arranged as shown in Fig (5). The modules operate with a total voltage equal to 42 volt and 55 Ampere at standard operation conditions with a maximum operation temperature equal to 50 °C. The modules covers 20 m<sup>2</sup> from the building roof area. The PV module connected to an inverter, which it connected to a battery

set. The inverter and batteries characteristics are shown in Table (2). This system is connected to AC power lines (i.e., with inverter) as shown in Fig (6). The user consumes the converted power in amount depend on the load profile as shown in Table (3). The extra power used to charging the battery during the day, and buys power from the grid during the night, low battery energy or high demand times.

Table (1): Summary for the PV, collector, module and PV array loss

<b>Collector Plane Orientation</b>		Tilt	30°	Azimuth	0°
<b>PV Array Characteristics</b>					
<b>PV module</b>	Si-poly	Model	<b>GES-6P90</b>		
		Manufacturer	Sainty Solar		
Number of PV modules		In series	2 modules	In parallel	10 strings
Total number of PV modules		Nb. modules	20	Unit Nom. Power	90 Wp
Array global power		Nominal (STC)	<b>1800 Wp</b>	At operating cond.	2319 Wp (50°C)
Array operating characteristics (50°C)		U mpp	42 V	I mpp	55 A
Total area		Module area	<b>13.7 m<sup>2</sup></b>	Cell area	11.7 m <sup>2</sup>
<b>PV Array loss factors</b>					
Thermal Loss factor		Uc (const)	20.0 W/m <sup>2</sup> K	Uv (wind)	0.0 W/m <sup>2</sup> K / m/s
=> Nominal Oper. Coll. Temp. (G=800 W/m <sup>2</sup> , Tamb=20°C, Wind=1 m/s.)				NOCT	56 °C
Wiring Ohmic Loss		Global array res.	13 mOhm	Loss Fraction	1.5 % at STC
Module Quality Loss				Loss Fraction	0.1 %
Module Mismatch Losses				Loss Fraction	4.0 % (fixed voltage)
Incidence effect, ASHRAE parametrization		IAM = 1 - bo (1/cos i - 1)	bo Parameter	0.05	

Table (2): Battery and inverter systems parameters. STC: standard test condition).

<b>System Parameter</b>	System type	<b>Stand Alone System</b>	
<b>Battery</b>	Model	<b>Volta 6SB100</b>	
	Manufacturer	VOLTA Bangladesh	
Battery Pack Characteristics	Voltage	36 V	Nominal Capacity 100 Ah
	Nb. of units	3 in series	
	Temperature	Fixed (25°C)	
<b>Regulator</b>	Model	General Purpose Default	
	Technology	Undefined	Temp coeff. -5.0 mV/°C/elem.
Battery Management Thresholds	Charging	40.5/39.2 V	Discharging 35.3/37.8 V
	Back-Up Genset Command	35.5/38.7 V	

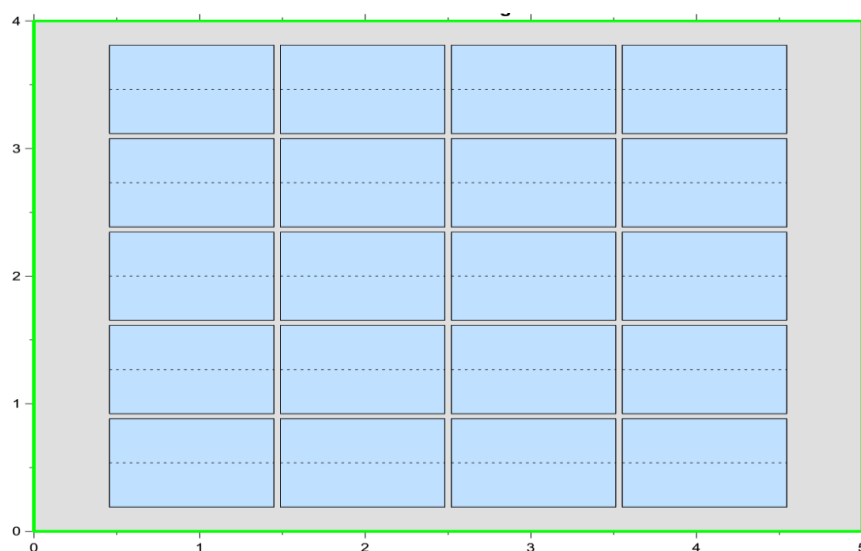


Fig (5): General modules layout with total area (total

### 3. PVSyst: Simulation Methodology

Fig (6) shows the proposed model of the off-grid connected PV-batteries and inverter system simulated within PVSyst.

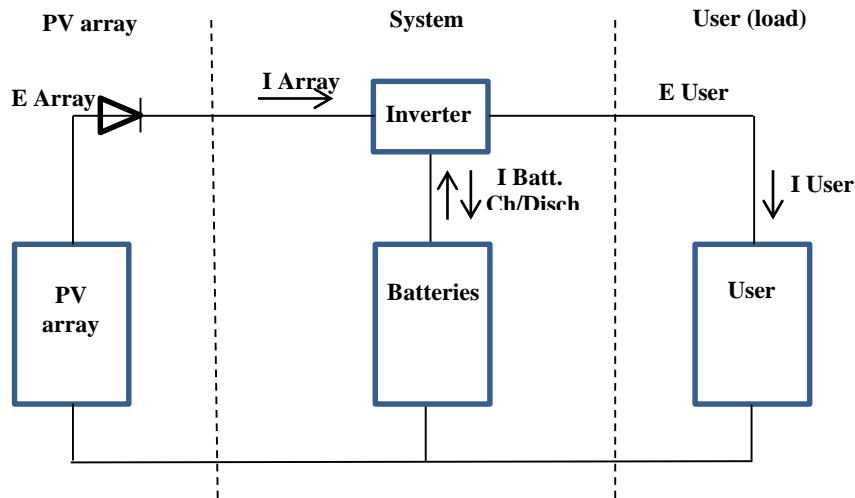


Fig (6): Off-Grid connected PV system.

To clarify the operating of a PV module, PVSyst use the one diode model, [9]. This model is based on the equivalent circuit for defining a single cell as shown in Fig (7). The model can be applied for the whole module because that all cells are considered as thoroughly similar.

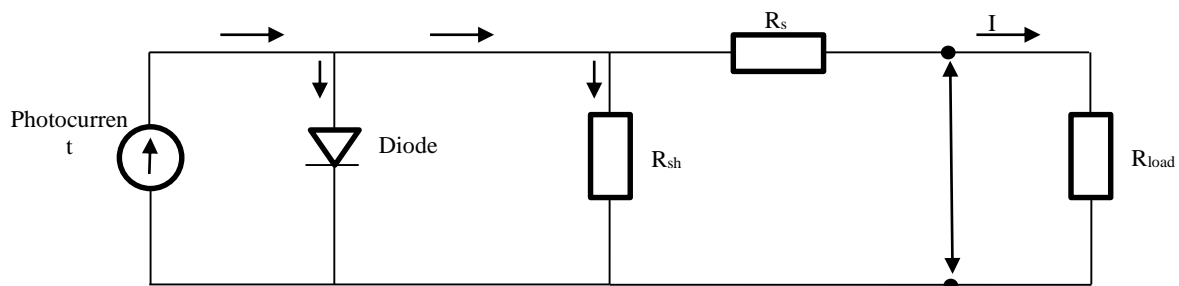


Fig (7): equivalent circuit for a single PV cell.

#### 3.1 PV model

The main mathematical relations which representing the general one-diode current model are, [9]:

$$I = I_{ph} - I_0 \left[ \exp\left(q \cdot \frac{V + I R_s}{N_{cs} \cdot \gamma \cdot k \cdot T_c}\right) - 1 \right] - (V + I R_s) / R_{sh} \quad (1)$$

The photocurrent  $I_{ph}$  depend on the incidence solar radiation and cell's temperature, it will be determined using the other parameters supplied under a standard test conditions STC:

$$I_{ph} = \left( \frac{G}{G_{ref}} \right) \cdot [I_{ph,ref} + m u_{ISC} (T_c - T_{c,ref})] \quad (2)$$

The diode's reverse saturation current  $I_o$  is assumed to change with the cell temperature according to the relation:

$$I_o = I_{o,ref}(T_c/T_{c,ref})^3 \cdot \exp[(q \cdot E_{Gap}/\gamma \cdot k) \cdot (1/T_{c,ref} - 1/T_c)] \quad (3)$$

Thus, for a given cell temperature and incident solar radiation, the model based on main five unknown parameters ( $R_s, R_{sh}, I_{ph}, I_{o,ref}$  and  $\gamma$ ) and with these conditions, it's difficult to solve equations 1 to 3 numerically without a suitable assumptions. Depending on the type a photovoltaic cell material, the values for the parameters under standard test conditions can be supplied from the manufacturer.

As it is not possible to deduce it from the manufacturer's datasheet, the value of the shunt resistance  $R_{sh}$  which representing the inverse of the slope of the  $I(V)$  curve for low  $V$ , will be independently treated (assumed a fixed in the equations), [7]. In order to determine the four remaining parameters, the four conditions below can be written for the specified standard test conditions  $G_{ref}$  and  $T_{c,ref}$ , which can be considered as equation 4:

- $I(V)$  at point  $V = 0$  (short circuit),
- $I(V)$  at point  $I = 0$  (open circuit),
- $I(V)$  at any other point, close to the maximum power point.,
- The derivative  $\mu V_{co} = dV_{co}/dT_c$ .

(4)

### 3.2 Battery model

In PVSyst, the basic linear battery's model, takes the form below, [10]:

$$U_{batt} = U_{oc,base} + \alpha \cdot SOC + \beta \cdot (T_{batt} - T_{ref}) + R_i \cdot I_{batt} \quad (5)$$

This model is then accomplished by a series of parameters, whose values are predefined in the PVSyst software (especially by the chosen battery technology type), or adjusted by the user itself if he has more specific data for his own battery.

## 4. Results and Discussions

The user demand represents the important factor in the design of the power production systems. In this study, the user demand shown in Table (3), which represents a real data taken from electrical bills for the researcher's house. With monthly electrical energy demand of

17127 kWh/month (minimum load = 695 kWh, maximum load= 2225 kWh) as shown in the Table (4), the load seems to be peak during June to July.

Table (3): The user monthly load with average monthly equal to 17127 kWh/mth.

Jan.	Feb.	Mar.	Apr.	May	June	July	Aug.	Sep.	Oct.	Nov.	Dec.	Year	
1095	695	695	1504	1504	2225	2225	1900	1900	1145	1145	1095	17127	kWh/mth

Table (4): The energy balanced and main results.

	GlobHor kWh/m <sup>2</sup>	GlobEff kWh/m <sup>2</sup>	E Avail kWh	EUnused kWh	E Miss kWh	E User kWh	E Load kWh	SolFrac
January	76.0	104.3	217.3	0.25	892	203.2	1095	0.186
February	95.0	119.6	266.4	34.34	493	202.2	695	0.291
March	144.0	161.7	357.3	43.94	443	251.8	695	0.362
April	174.0	173.9	356.4	12.91	1185	318.8	1504	0.212
May	221.0	198.6	402.7	6.14	1130	374.4	1504	0.249
June	231.0	197.3	395.6	4.39	1874	350.8	2225	0.158
July	236.0	206.3	411.4	1.49	1841	383.5	2225	0.172
August	217.0	208.3	413.0	2.29	1529	370.5	1900	0.195
September	173.0	189.3	381.1	0.96	1559	341.0	1900	0.180
October	136.0	170.8	361.3	15.29	815	329.9	1145	0.288
November	95.0	133.3	276.8	1.82	884	261.2	1145	0.228
December	74.0	108.5	225.5	1.04	884	210.8	1095	0.193
Year	1872.0	1971.8	4064.8	124.86	13529	3598.2	17127	0.210

Legends: GlobHor Horizontal global irradiation E Miss Missing energy  
 GlobEff Effective Global, corr. for IAM and shadings E User Energy supplied to the user  
 E Avail Available Solar Energy E Load Energy need of the user (Load)  
 EUnused Unused energy (full battery) loss SolFrac Solar fraction (EUsed / ELoad)

The suggested hybrid system in the present investigation consist of a combination of PV panels supplemented with battery set and inverter. The simulation explores a mix of climate conditions and the system components characteristics such as modules power output (kWp) and battery storage behaviour to match the user need. PVsyst allows an hourly time step simulation for analysis the system components as shown in Fig (8).

The yearly average solar radiation incident on the PV modules surfaces equal to 1872kWh/m<sup>2</sup>.

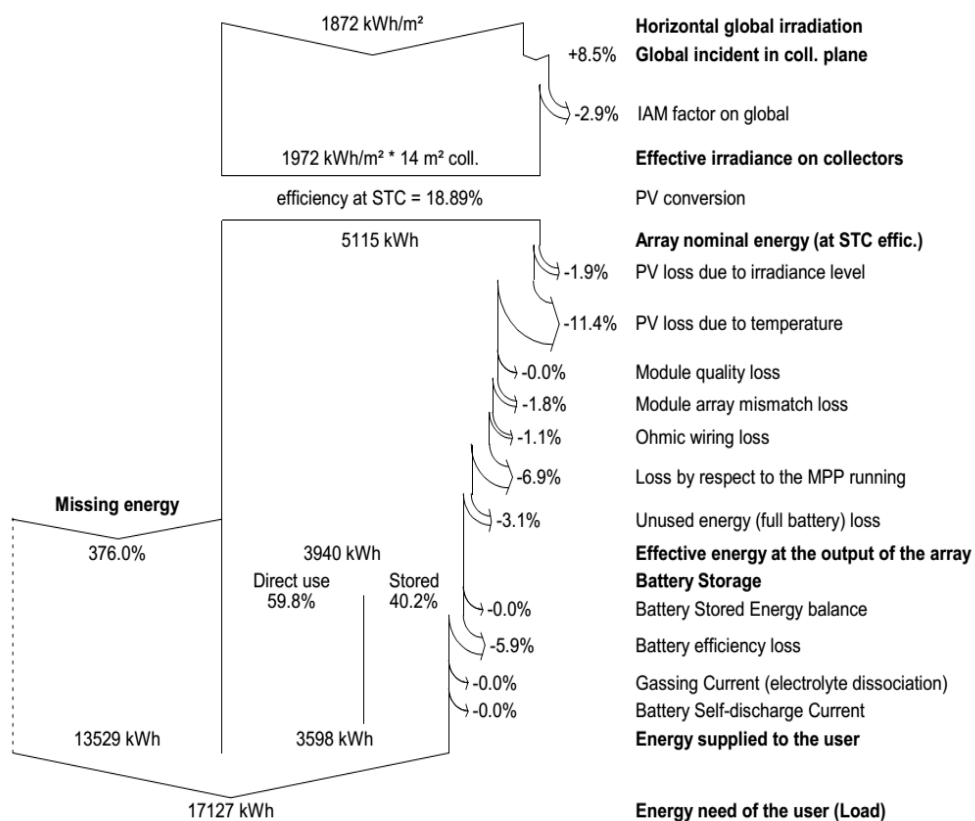


Fig (8): Power generation system energy and loss analysis

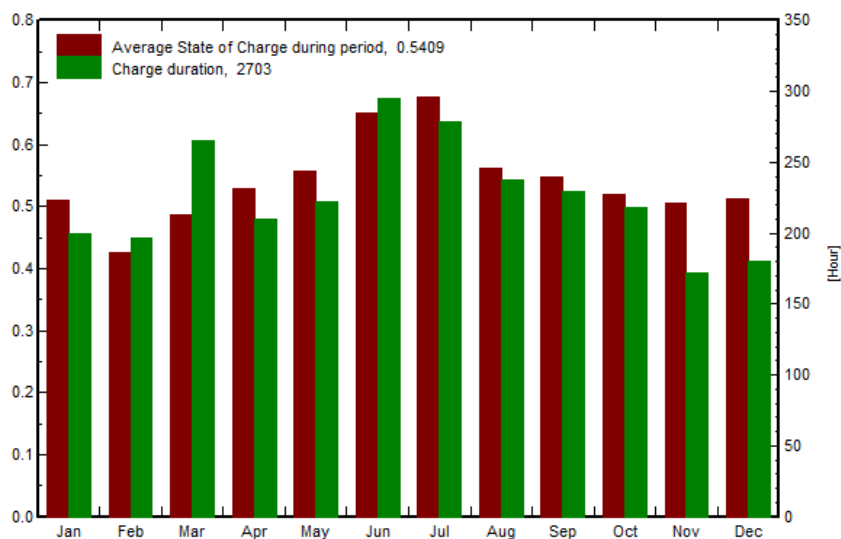


Fig (9): Batteries charging state and charge duration.

The collected solar radiation suffers from different types of losses, the array incidence loss, high temperature loss, reflective loss and electrical resistance losses and many others.

The net energy reached the batteries from the inverter equal to 3940 kWh. The net energy that reaches batteries from the inverter 3940 kWh.

The battery was in discharging state (i.e. energy supply) for 40.2%, while 59.8% the battery in charging state (i.e. off) from the simulation period. From the Fig (9), the charging duration equal to 2703 hour which representing 54% from the total hours.

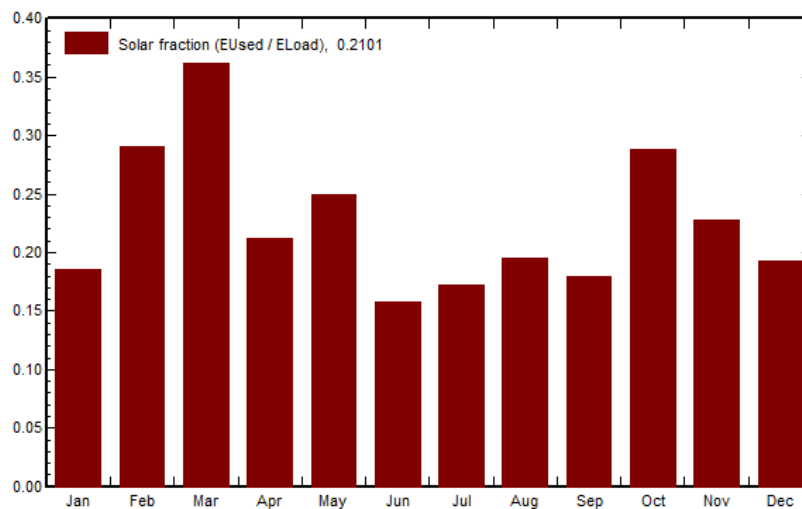


Fig (10): The solar energy fraction from the user

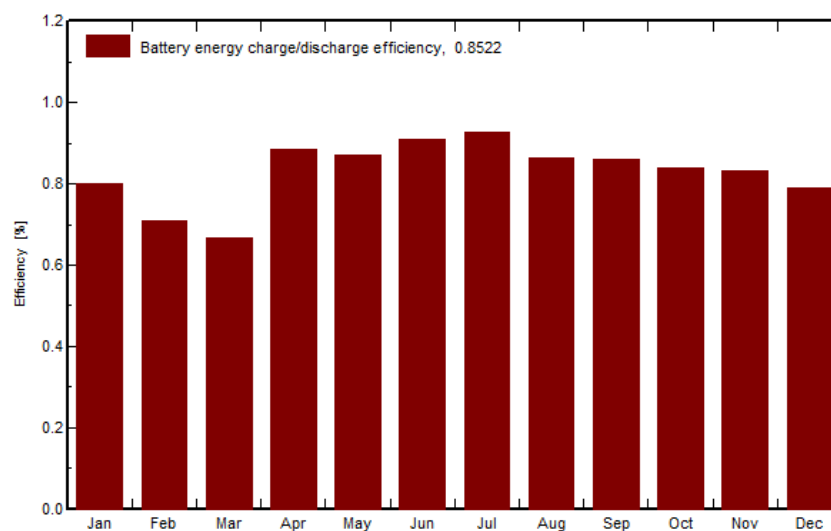


Fig (11): The batteries energy charging/discharging cycle efficiency.

The solar energy fraction from the total user need 3598 kWh and this represents 21% from the total demand; the user should buy 13529 kWh from the grid which representing 79% from the total demand as shown in Fig (10). The system operation keeps the batteries charging and discharging continuously. Fig (11) shows that the process efficiency reach more than 85%.



#### 4. Concluding Remarks

The investigation indicates that the Baghdad location received considerable amount from monthly average daily beam normal solar radiation ( $4.23 \text{ kWh/m}^2$ ), is a prospective candidate for deployment of PV power components. The study results show that for a micro generation system composed of 1.8-kWp PV system together with three batteries storage with overall energy storage 3.6 kWh and an inverter system. The solar penetration found to be 21% from the total demand. The solar penetration values can be maximised through the following:

- Increasing PV module capacity and or numbers: In general, the building's roof in Iraq a flat type, this allow to increase PV modules numbers.
- Reducing user load (demand side): the demand side has a direct effect on the ratio off solar contribution to load energy (from grid) ratio, the user should minimise the demand to achieve high solar penetration.
- High batteries efficiency: Using solar deep cycle batteries with 24 voltages and 200-Ampere current. This allow for decreasing batteries number and increasing the efficiency of charging/discharging and charging period.

#### 5. References

1. IEA, International Energy Agency, Key World Energy Statics, 2014.
2. Ministry of Electricity, <http://www.moelc.gov.iq>, Statistical data.
3. IEA, International Energy Agency, Feed-in tariff: A policy tool encouraging deployment of renewable electricity technologies, <http://www.eia.gov/todayinenergy>.
4. Majid J., Sheeraz K. and Mohammad R., 'Techno-Economic Feasibility Analysis of Solar Photovoltaic Power Generation: A Review', Smart Grid and Renewable Energy, 3(2012), pp: 266-274.
5. Kazem H. A. and Chaichan M. T., 'Status and future prospects of renewable energy in Iraq', Renewable and Sustainable Energy Reviews, 16 (2012), pp: 6007–6012.
6. Ramoliya V. J., 'Performance Evaluation of Grid-connected Solar Photovoltaic plant using PVSYST Software', Journal of Emerging Technologies and Innovative Research (JETIR), 2 (2015), pp: 372-378.
7. PVSyst: [www.pvsyst.com](http://www.pvsyst.com).
8. Meteonorm: [www.meteonorm.com](http://www.meteonorm.com).
9. pvmodule\_model.htm: [www.pvsyst.com](http://www.pvsyst.com).
10. batteries\_modeldescription.htm: [www.pvsyst.com](http://www.pvsyst.com).

**NOMENCLEATURE:**

$E_{\text{Gap}}$  = Gap's energy of the cell's material.

$G$  and  $G_{\text{ref}}$  = Effective and reference irradiance,  $\text{W/m}^2$ .

$I$  = Current supplied by the module, A.

$I_{\text{ph}}$  = Photocurrent, A.

$I_d$  = Diod current, A.

$I_o$  = Inverse saturation current, A.

$I_{\text{SC}}$  = Short circuit current, A.

$I_{\text{batt}}$  = Battery current (charge>0, discharge<0).

$k$  = Boltzmann's constant= $1.381.E-23$  J/K.

$\mu_{I_{\text{SC}}}$  = Temperature coefficient of the photocurrent (or short circuit current).

$N_{\text{cs}}$  = Number of cells in series.

$q$  = Charge of electron= $1.602.E-19$  Coulomb.

$R_s$  = Series resistance, ohm.

$R_{\text{sh}}$  = Shunt resistance, ohm.

$R_i$  = Internal resistance, assumed to be constant.

SOC = State of charge (varies from 0 to 1).

$T_c$  = Effective temperature of the cells, °K.

$T_{\text{c,ref}}$  = Reference cell's temperature, °K.

$T_{\text{batt}}$  = Temperature of the battery.

$T_{\text{ref}}$  = Reference temperature (usually 20 °C).

$U_{\text{batt}}$  = Voltage for a battery-element.

$U_{\text{oc,base}}$  = Intercept of the open circuit voltage linear part of SOC.

$V$  = Voltage at the terminal of the module, V.

$V_{\text{oc}}$  = Open circuit voltage, V.

**GREEK SYMBOLS:**

$\gamma$  = Diode quality factor, normally between 1 and 2.

$\alpha$  = Slope of the open circuit line (depend on the chemical couple of battery solution).

$\beta$  = Temperature coefficient (-5 to -6).